

Copyright
by
Matthew Louis Wisher
2014

The Dissertation Committee for Matthew Louis Wisher
certifies that this is the approved version of the following dissertation:

**Pulsed Magnetic Field Generation for Experiments in High
Energy Density Plasmas**

Committee:

Gary Hallock, Supervisor

Roger Bengtson, Co-supervisor

Michael Becker

Todd Ditmire

Mercer Driga

**Pulsed Magnetic Field Generation for Experiments in High
Energy Density Plasmas**

by

Matthew Louis Wisher, B.S., M.S.E.

DISSERTATION

Presented to the Faculty of the Graduate School of
The University of Texas at Austin
in Partial Fulfillment
of the Requirements
for the Degree of

DOCTOR OF PHILOSOPHY

THE UNIVERSITY OF TEXAS AT AUSTIN

August 2014

Get your bachelor's degree.

Get your master's.

Or get your Ph.D.

But most of all...

GET YOUR HORNS UP.

Acknowledgments

I would like to begin by thanking my parents, Danny and Charlene Wisher, for their unwavering encouragement and support through this long, long journey. I could double the size of this thesis by describing all they have given, sacrificed, and endured so I could get to this point. Of all these things, one stands out most: the morally wholesome, Christian household in which they raised me. This, I know, is the root of the work ethic that has kept me going, and the benefit of such an upbringing cannot be overstated. They have, and continue to, exemplify the essence of godly family. I hope that with this short paragraph, I can honor them in at least a small way, although I could never write enough for the reader to appreciate what outstanding people they are. I would also like to thank my siblings, Samuel, Ruth, and David, for their encouragement as well, and I am certain that they echo my appreciation of our parents.

To my colleagues in the Center for High Energy Density Science (CHEDS) at the University of Texas at Austin (UT-Austin), I say thank you for the stimulating conversations, and for your support, both technical and moral. Thanks to Professor Todd Ditmire for welcoming me into his group and enabling the fine pulsed laser facilities at our campus. Additionally, I must thank the excellent staff at the Texas Petawatt Laser (TPW) facility for their expertise during the experiment discussed in this work. Most notably, Dr. Hernan Quevedo (CHEDS), has worked closely with me

throughout my graduate student career, and I owe him many thanks for allowing me to pick his brain and steal his optics.

Several UT-Austin students have played a large role in my work: these are Sean Lewis, Nathan Riley, and John Currier. Sean has been a great lab-mate and comrade in this work, and continues to explore physics at Sandia National Laboratories (SNL) for his own Ph.D. work. Nathan's encyclopedic knowledge of his field is terrific; I find discussions with him to be rich in detail and highly enlightening. John, who recently received the bachelor's degree in physics from UT-Austin, volunteered to work with me in the laboratory, including during the TPW experiment; he has an outstanding work ethic, and I hope I work with many more like him in the coming years.

The staff of Sandia National Laboratories (the "Sandians") have meant a great deal to me in several ways during my time at UT-Austin. The project that I undertook for my Ph.D. work was initiated by Dr. Kenneth Struve, who has been in touch since the beginning, and has been a wonderful resource, teacher, and colleague during that time. Additionally, Brian Stoltzfus, another Sandian, has provided technical expertise in pulsed power science which is unmatched by others I have encountered. These two embody the excellence of our national laboratories, and it has been an honor working with them. I must also thank SNL for sponsoring me for the National Physical Sciences Consortium (NPSC) fellowship, and for the fascinating internship experience in the summer of 2011.

I extend my gratitude to the fine people of the UT-Austin Physics Machine Shop for their technical expertise and enjoyable conversations throughout the years. I would especially like to recognize Jack Clifford, who taught me everything I cared

to know about machine tools and techniques, and then some. I also thank Keith Carter, who knows more about how to get things done in a laboratory than pretty much anyone else I've met. Experimental work is made or broken on the technical competency of the experimenter, and Keith has saved me from foolish mistakes in the laboratory more than once.

Lastly, I would like to extend thanks to my two advisors: Prof. Gary Hallock (ECE) and Prof. Roger Bengtson (CNS). I must thank Prof. Hallock for keeping me “grounded” to my roots as an electrical engineer, and for helping me navigate the treacherous slopes of the Ph.D. program.

And I must thank Prof. Roger Bengtson for taking me on as his student to explore the wild world of pulsed power. Roger once said to me that his students are, in some sense, like his kids; I didn't quite understand what he meant until the very end of our journey together. There were many times I felt lost, and even more times that I was confused, but through this all, Roger made the struggles bearable, and turned confusion into fascination. Even now, I'm not sure how he did this, but I suppose that's the mark of a wise advisor. To think about all the years he has been doing physics, and to know that it is still “fun” to him, is inspiring beyond explanation. Roger has been generous in time and patience, and I am honored to say that he has been my advisor.

It has been a true privilege to be a graduate student at UT-Austin for these last six years. I'm glad to come to the end of this journey, but regardless of where the future takes me, Texas will always feel like home. . . my Texas.

-Hook 'em

Pulsed Magnetic Field Generation for Experiments in High Energy Density Plasmas

by

Matthew Louis Wisher, Ph.D.

The University of Texas at Austin, 2014

Supervisors: Gary Hallock
Roger Bengtson

Experiments in high energy density (HED) plasma physics have become more accessible with the increasing availability of high-intensity pulsed lasers. Extending the experiment parameters to include magnetized HED plasmas requires a field source that can generate fields of order 100 tesla. This dissertation discusses the design and implementation of a pulsed field driver with a designed maximum of 2.2 MA from a 160 kJ capacitor bank. Faraday rotation measurement of 63 T for a 1.0 MA discharge supported Biot-Savart estimates for a single-turn coil with a 1 cm bore. After modification, the field driver generated up to 15 T to magnetize supernova-like spherical blast waves driven by the Texas Petawatt Laser. The presence of the high field suppressed blast wave expansion, and had the additional effect of revealing a cylindrical plasma along the laser axis.

Table of Contents

Acknowledgments	v
Abstract	viii
List of Tables	xii
List of Figures	xiii
Chapter 1. Introduction	1
1.1 Motivation	1
1.2 High energy density (HED) magnetized plasmas	3
1.2.1 Laser irradiation	3
1.2.2 Electrical discharge	7
Chapter 2. Magnetized plasma experiments	10
2.1 Related work	10
2.2 Requirements	11
2.2.1 High field	11
2.2.2 Operation in vacuum	13
2.3 Pulsed field generation	14
2.3.1 Pulsed power	14
2.3.2 Pulsed power capabilities	16
2.3.3 Special considerations	19
Chapter 3. MegaGauss 2, a pulsed magnetic field driver	28
3.1 Origin	28
3.1.1 Initial design from Sandia Labs	28
3.1.2 Modification at UT-Austin	30
3.2 Design	32

3.2.1	Portability	32
3.2.2	Vacuum compatibility	33
3.2.3	Low inductance	35
3.2.4	Construction	37
3.2.5	Circuit analysis	50
3.3	Performance	62
3.4	Magnetic field measurement	70
3.4.1	Coil types	70
3.4.2	Field estimation with simplified model	72
3.4.3	Faraday rotation measurement	74
Chapter 4. Experiment design and execution		80
4.1	Initial experiments	80
4.1.1	Cluster plasma generation	80
4.1.2	Magnetized cluster fusion	83
4.2	Magnetized blast waves	85
4.2.1	Description of target	85
4.2.2	Gas fill testing with pulsed power	88
4.2.3	TPW description	89
4.2.4	Implementation of MG2 on TPW	96
4.2.5	Diagnostics	101
4.2.6	Expectations	104
Chapter 5. Experiment results from MBW-1		107
5.1	Pulsed power performance	107
5.2	Plasma channel	112
5.3	Interpretation of plasma channel	122
5.3.1	Plasma creation mechanism	123
5.3.2	Plasma filament in no-field shots	128
5.3.3	Plasma filament in high-field shots	131
5.3.4	Summary of plasma behavior	134

Chapter 6. Conclusion	136
6.1 Summary	136
6.2 Future work	138
List of Symbols	140
Bibliography	144
Vita	154

List of Tables

3.1	Effective inductances of MegaGauss 2 (MG2) components for different capacitor bank configurations. All values are in nH and are estimates using ideal conditions, except for capacitor inductance, which is specified by the manufacturer as an absolute maximum. These values correlate with Figure 3.16.	35
3.2	Estimated values for inductance of switch can enclosure components. All elements are approximations to a coaxial transmission line with dimensions from Figure 3.6.	36
3.3	Lumped circuit values for RLC model, derived from individual MG2 component values. Values are estimates.	54
4.1	Gas fill trial #1: Parker 099-0065-900 pulse valve (flow aperture inner diameter (ID) .76 mm).	90
4.2	Gas fill trial #2: Parker 009-0089-900 pulse valve (flow aperture ID 2.95 mm).	91
4.3	Gas fill trial #3: Same as trial #2, but a plastic fill tube length (4.4 cm) was added to electrically insulate the pulse valve from the MG2 chamber. *8-point average.	92
4.4	Gas fill trial #4: Same as trial #3, but pressures and fill times are 4-point averages. A turbopump reduced ambient pressure to <10 mTorr to remove potential influence on the gas fill time.	92
5.1	Keldysh parameter for the first five ionizations of xenon.	127

List of Figures

1.1	A capacitive storage pulsed power system slowly accumulates electric charge and rapidly releases it as a high-power pulse discharge [4]. . .	2
1.2	Clusters are created by releasing high-pressure (~ 1 MPa) gas through a supersonic nozzle. A high-intensity laser pulse ionizes the cluster plume 2 mm below the nozzle opening.	4
1.3	Several works have established the energy dependence of DD fusion; the figure above shows several of these, compiled by Erba [16]. Clusters can generate ions with energies of several keV, which can be sufficient to access the low end of the energy range shown.	5
1.4	Pressure in atmospheres behind a spherical blast wave as a function of radial distance (arbitrary units) from the blast wave center. Each pressure curve is labeled with its time from the start of the blast wave. Please refer to [7] for a discussion of the radial and time scaling in this figure (Figure 4 in [7]), which are dependent on initial conditions. . .	7
1.5	Photograph of a Z-pinch wire array for experiments on the Z Machine at Sandia National Laboratories. Photograph from http://www.sandia.gov/z-machine	8
1.6	Section view of the Z Machine at Sandia National Laboratories (SNL) [4].	8
2.1	Left to right, a high-field (~ 200 T) coil before and after a shot. Magnetic pressure within the copper loop explodes the coil. Images courtesy of C. Mielke, LANL [57].	13
2.2	Paschen breakdown voltages for parallel plate electrodes with various gases at 20° C [10, 35].	20
2.3	Magnetic pressure coming about from current flow along a parallel plate transmission line will push the plates apart. Damage can result if the design is not suited for this pressure.	26
3.1	Current from a capacitor bank flows through coaxial cables to a central chamber that accumulates current from all capacitors. Within this chamber, a vacuum-insulated conical transmission line directs the current to the load, which is situated on the top of the conical line. .	29

3.2	Left: The original design from Sandia National Laboratories (SNL) used a large vacuum chamber (~ 90 L volume), which included the triplate transmission line in the vacuum volume. Right: A smaller vacuum chamber (~ 3 L) fixed to the top of the transmission line reduced the vacuum volume, and avoided technical difficulties arising from operating the transmission line in vacuum. Highlighted portions of the schematics indicate vacuum volumes.	31
3.3	The entire MegaGauss 2 system at The University of Texas at Austin. All ten capacitors are connected to the central vacuum chamber. The control electronics rack and charge and trigger distribution tanks are visible in the background.	32
3.4	Detail view of original vacuum insulators as designed at Sandia National Laboratories. Space enclosed (right) by insulators is vacuum volume. Discharge cables connect to the atmosphere (left) side, as in Figure 3.8. Additional elements of triplate and chamber are suppressed to show features.	34
3.5	Detail view of vacuum insulator. Space above angled insulator is vacuum volume, which is enclosed by the small chamber atop the upper region of triplate transmission line. Also visible: 3/4 inch blast wave target, which is detailed in Section 4.2.1, and insulating disks between triplate layers.	34
3.6	Approximation of switch enclosure components to coaxial segments. Left: section view of an enclosure. Right: coaxial transmission line simplification. Segments A–B: capacitor terminal, C: spark gap switch (electrode diameter), D–E: salt water resistor, F: discharge cables. Values for each segment are listed in Table 3.2.	36
3.7	Capacitor and switch module, with cutaway of switch enclosure. Not shown: trigger resistor, shorting lever, and discharge cables.	38
3.8	Left: collet plates secure cables to triplate perimeter. Right: capacitor bank modules 6, 7, and 8. Background: charge dump tank with charge cables.	40
3.9	Section view of triplate transmission line. Dimensions provide values for inductance and impedance calculation. Bottom and top layers are the cathode, and the middle layer is the anode.	41
3.10	Angled vacuum insulators help avoid breakdown (flashover) across the anode-cathode gap. This influences the design of transmission line transition sections, e.g. between atmosphere and vacuum. Conical half angle (γ) is conventionally negative when the dielectric is wider on the anode side (the left image in the figure) [4].	43
3.11	A coil assembly fits inside a split clamp. Several screws that pass through the clamp halves tighten the clamp and secure the coil by engaging threads on the UCP.	44

3.12	Schematic of charge dump tank. A 120 VAC control signal energizes dump relay coil. A high-voltage DC source charges capacitors through 16.2 k Ω dump resistors. Disabling the 120 VAC signal closes the dump relay, forcing the capacitor bank to discharge through the dump resistor chain.	46
3.13	Schematic of master trigger tank. A high-voltage pulse triggers the master switch, which shorts to ground and sends a falling-edge pulse ($1/2 V_{\text{chg}} \rightarrow \text{GND}$) to capacitor bank switches. Arrival of this pulse triggers the capacitor bank.	48
3.14	Schematic diagram of sensing coils that monitor discharge current. . .	49
3.15	This series combination of a resistor, inductor, and capacitor (series RLC) is the simplest form of the circuit schematic for the MG2 system. Solving this circuit for $i(t)$ given the initial condition $v_c(t = 0) = V_{\text{chg}}$ will yield an ideal model of the system's behavior.	52
3.16	This schematic is an electrical representation of the most important circuit elements (resistors, inductors, and capacitors) in the MG2 system. The elements can be combined to produce the simple model in Figure 3.15.	55
3.17	Normalized plot of discharge current for the ten-capacitor system Equation (3.14). Maximum current of $0.81I_0$ occurs at 1.63 μs ; reverse current peaks at $-0.52I_0$	56
3.18	Comparison of discharge models using a single capacitor module. Green trace (not shown in inset): analytic RLC model prediction. Red trace (inset, smooth profile): numerical BERTHA simulation with a simple RLC arrangement as in Figure 3.19. Blue (inset, oscillating profile): numerical BERTHA simulation with component-specific simulation elements (Figure 3.20).	58
3.19	BERTHA schematic of a simple RLC model, using values from Table 3.3 for a single switch. Compare with Figure 3.15.	58
3.20	BERTHA schematic representing MG2 using one capacitor, with distinct circuit elements. Compare with Figure 3.16.	59
3.21	BERTHA schematic of entire ten-capacitor system. Top: capacitor bank; bottom: triplate transmission line and coil load. Schematic is split at node "A" to better fit the schematic into a single figure.	60
3.22	Illustration of the resulting total discharge current when four switches in the BERTHA schematic of Figure 3.21 are delayed by 1.5 μs . Total current has a dimple caused by the asynchronous switches peaking late. A proper discharge, and an ideal RLC model are shown for comparison; notice the high-frequency ringing in the BERTHA simulation plots.	61
3.23	In Shot 450, several switch/capacitor assemblies arced inside the switch enclosure. This bypassed the discharge cables and subsequent circuit elements, reduced the inductance of that sub-circuit, and resulted in a faster discharge.	64

3.24	Comparing the load B-dot signal with the sum of the capacitor currents can reveal if there was a fault in field production before the peak field occurred. A sudden deviation from expected behavior almost always indicates an arc (e.g. Shot #409).	65
3.25	Resonant frequency and time to peak for the MG2 system is dependent on the number of capacitors involved in the discharge. As the number of capacitors (N) decreases, the overall system inductance falls, making the discharge faster.	66
3.26	From left to right, coil failure modes range from dramatic expansion, necking to the point of coil separation, or complete fragmentation. These affects are driven by the magnetic pressure within the coil, although melting may play a role in generating the small pieces of debris as in the rightmost image.	69
3.27	Asynchronously discharging capacitors can result in a poor superposition of currents. This reduces the peak current, which here occurs much later than the ideal-case 1.63 μ s.	70
3.28	Photos of field coils and their computer-aided design (CAD) models with dimensions. Left: a high-field coil meant for maximum field generation for cluster fusion experiments. Right: a gas cell assembly for astrophysical blast wave experiments.	71
3.29	The magnetic field can be estimated by assuming the current is distributed along the coil length among several infinitesimally thin filaments lining the inner surface of the coil. Points are Faraday rotation measurements obtained from high-field coil shots (courtesy of S. Lewis).	73
3.30	A measurement of the changing intensity of the S and P polarized components of a probe beam undergoing Faraday rotation yields the high-frequency trace, which is deconvolved using Equation (3.17) to give a magnetic field measurement. Expected and measured discharge currents are plotted for comparison with the field measurement.	75
3.31	Faraday rotation measured values for magnetic field at several axial positions along the coil. Inset: terbium gallium garnet (TGG) crystal placement inside high-field coil representative of the positioning method during collection of the plotted data. Horizontal error bars reflect uncertainty in crystal position; vertical bars are measurement error. Data points courtesy of S. Lewis.	77
3.32	Using an axial distribution in combination with a radial falloff of current takes the estimate closer to the real measured field. Courtesy: S. Lewis.	78
3.33	A more advanced model of current distribution, such as this one, from [42], can better simulate the magnetic field. However, generating such a model is more complicated compared to the simpler static model as in Figure 3.29.	78

4.1	Clusters are created by releasing a burst of high-pressure (20 - 70 bar) gas through a supersonic nozzle. A high-intensity laser pulse ionizes the cluster plume 2 mm below the nozzle opening. High plasma temperature can yield nuclear fusion can occur if clusters contain deuterium. . . .	81
4.2	Exploded diagram of the gas cell assembly, with coil partially hidden to expose features on the polycarbonate body. The target pin is glued into a socket at the bottom of the body. Once the pin is secure, the body is inserted into the coil, and the remaining gas cell pieces are added. Inset: a completed assembly.	86
4.3	Target designed for Magnetized Blast Waves experiment #1 (MBW-1) experiments. Field coil wraps around polycarbonate gas cell. Texas Petawatt (TPW) beam enters and exits through pinholes along the long axis of the gas cell; diagnostic beam is perpendicular to the long axis and passes through anti-reflective (AR) windows on the gas cell.	87
4.4	Schematic diagram of the Texas Petawatt Laser [1].	94
4.5	Floor plan of the Texas Petawatt Laser [1]. The region labeled Target Area hosted the MBW-1 experiment.	96
4.6	Schematic layout of MG2 in the TPW target area for the blast waves experiment shows the placement of the capacitor bank and chamber in the TPW beam line.	98
4.7	Schematic arrangement showing relation of TPW beam, diagnostic path, and target.	98
4.8	Schlieren photography schematic. Unscattered light encounters a beam block at the focus of a collecting lens. Light scattered by density perturbations (e.g. a blast wave) has its trajectory modified, and is thereby diverted around the beam block to be captured by a camera.	102
4.9	Nomarski interferometry can use a single beam to produce an interferometric measurement by dividing a single probe beam into two oppositely polarized beams [27].	103
5.1	MG2 Shot 534 shows asynchronously discharging capacitors resulting in a poor superposition of currents. This reduces the peak current, which here occurs much later than the ideal 1.63 μ s. A laser sync pulse shows the laser's arrival on target with respect to the discharge timing. . . .	108
5.2	Peak current and field, and field upon laser incidence on target for each MBW-1 shot. Increase in consistency in second and third shot groups is due to reduction from five to two capacitor modules, which improved discharge synchronization. Zero values are due to failed measurement or discharge faults (e.g. breakdown).	109

5.3	A varying discharge produces a varying magnetic pressure, giving a time dependence on the maximum temperature (kT in nkT) for which $\beta = 1$. This temperature is plotted versus time for the 15 T mode in MBW-1. The temperature variation is least near the peak where $di(t)/dt \approx 0$. Density $n = 1.3 \times 10^{18} \text{ cm}^{-3}$	113
5.4	Comparison of the no-field and high-field case. The no-field case does not seem to affect the spherical blast wave's expansion, but the high-field ($> 10 \text{ T}$) case contracts the spherical blast wave and reveals a contracted laser filament. Dashed circle around the pin represents the field-of-view boundary. Note that these features are not always visible in experiment images; and are only meant to be interpretive aides. . .	115
5.5	All no-field Schlieren images from MBW-1. Delay between laser irradiation and probe beam varied between 50 and 350 ns. Dark lines indicating a sharp density gradient appear in most images. Laser enters from the left; for scale, crosshair circles are labeled with their diameters in millimeters.	117
5.6	All low-field Schlieren images from MBW-1. Dark lines indicate a sharp density gradient. In both shots, these lines appear thinner than those in the no-field case. For comparison, the most similar no-field shots are show below their respective low-field shots. Laser enters from the left; for scale, crosshair circles are labeled with their diameters in millimeters.	118
5.7	Selected high-field Schlieren images from MBW-1. Dark lines indicate a sharp density gradient. Filamentary structure is in stark contrast to quasi-spherical structure in no-field and low-field shots. Also note the bubble-like structure surrounding the pin. Laser enters from the left; for scale, crosshair circles are labeled with their diameters in millimeters.	120
5.8	Selected high-field Schlieren images from MBW-1 with unidentifiable or inexplicable features are shown for completeness. Laser enters from the left; for scale, crosshair circles are labeled with their diameters in millimeters.	121
5.9	Time evolution of the laser filament seen in high-field shots. Initial plasma should only be in the focal region, but can expand at later times. The first two figures do not have comparable experimental images. Images from Shots 7053, 7066, and 7021 in Figure 5.7 are respectively comparable to the cartoon images for $T_0 + 50 \text{ ns}$, 100 ns , and 250 ns .	122
5.10	High-field shots yield new structures around the target pin. Left: Shot 7014 provides comparison with the no-field case at the same probe beam delay. Center: original image for Shot 7021, filament and bubble structures are clearly visible. Right: a cartoon superimposed on Shot 7021's image highlights the two structures under discussion. Laser enters from the left; for scale, crosshair circles are labeled with their diameters in millimeters.	123

5.11	Ordinarily, an atom's potential well contains its electrons. In the presence of strong electric field, this potential well is distorted, which creates an opportunity for the electron to escape by tunneling, a quantum mechanical effect [12].	127
5.12	Ionization rates for xenon across one laser cycle using values from Figure 5.11 in Equation (5.4). Rates are normalized to 10^{16} s^{-1} , with their scale factors listed in the plot callouts.	129
5.13	An expansion of the plasma filament is visible as probe delay increases. From left to right, plasma filament radius is approximately 1 mm, 1.3 mm, and 1.5 mm. Due to the Schlieren imaging apparatus using a half-beam block and illuminating only the top surface of the filament, symmetry about the horizontal axis is assumed for measurement purposes. This symmetry-breaking effect is discussed in Section 4.2.5.	133

Chapter 1

Introduction

1.1 Motivation

Recent decades have seen advances in high intensity lasers that present new possibilities for accessing the high energy density (HED) plasma regime [21,22,43,44,63]. In particular, a high intensity laser pulse incident on solid density targets can ionize the target and generate hot electrons and ions. This HED regime provides a path to exciting experiments exploring stellar conditions, fusion reactions, and particle acceleration [9]. In addition, magnetization of the HED plasma regime extends the possibilities of these experiments, providing opportunities to study magnetohydrodynamic (MHD) plasmas, magnetized astrophysical conditions, confinement of hot plasmas, and magnetically-influenced instabilities.

Accessing this magnetized regime can be technically challenging due to the high field densities required to influence an HED plasma. With plasma pressures well into the gigapascal range, magnetized HED plasma experiments require at least multi-tesla magnetic fields to effect a meaningful change in the plasma behavior. While permanent magnets may access the range of a few tesla, a truly useful magnetic field source will reach tens to hundreds of tesla consistently. An apparatus that could generate such a field continuously would foreseeably require tremendously low-loss

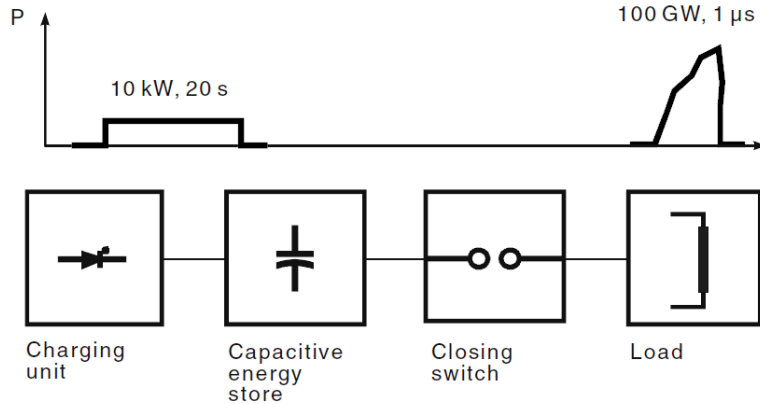


Figure 1.1: A capacitive storage pulsed power system slowly accumulates electric charge and rapidly releases it as a high-power pulse discharge [4].

conductors (i.e. superconductors), a vast electrical power source, and additional costly or impractical resources.

Generating a magnetic field of this strength encourages a pulsed approach, in which the magnetic field is sufficiently strong for a duration longer than that of the HED plasma’s lifetime; that is, the field outlasts the time scale of the relevant plasma events. A pulsed field source takes advantage of this duration constraint by concentrating its energy into a brief burst, relaxing complications such as conductor heating and high-power current sources.

A pulsed current driver generating a pulsed magnetic field can accumulate energy slowly ($\tau_{charge} \approx 1$ minute) using a low current source, and later release its energy quickly ($\tau_{pulse} \approx 0.1\text{--}1$ μs). This time compression of the accumulated energy results in an enormous peak power as depicted in Figure 1.1, which can be converted into a magnetic field that peaks sufficiently high to magnetize an HED plasma.

1.2 High energy density (HED) magnetized plasmas

1.2.1 Laser irradiation

A high-intensity pulsed laser can accelerate electrons out of a solid target, and the resulting space charge accelerates the leftover ions. This can accelerate the ions to several keV, and can form an HED plasma in the region close to the target where the number density remains sufficiently high. These solid targets vary in form and material, but deposition of energy into the electrons is the principal mechanism of plasma creation and will drive plasma generation in two particular cases of interest here: cluster fusion and astrophysically relevant blast waves.

Cluster fusion

Clusters are nano-scale solid targets that can generate multi-keV ions [6, 13, 39, 60], which, in the case of deuterated clusters, can exhibit DD nuclear fusion [14, 65]. Clusters are produced when a supersonic nozzle releases a high-pressure (2–7 MPa) gas into vacuum, creating an expanding adiabatic stream of gas. As the gas cools, the van der Waals' attractions between molecules draw them together into solid density clumps [25]. When irradiated by a high-intensity laser pulse, the clusters absorb nearly all ($\sim 90\%$) of the laser energy. The laser's electric field ionizes the atoms in the clusters and accelerates the freed electrons away. Without those electrons, the remaining cluster is positively charged, and the ions in the clusters experience a space charge that can drive the ions apart with multi-keV energy. Clusters containing deuterium can generate hot deuterium ions, and ions from neighboring clusters can undergo collisions that yield nuclear fusion.

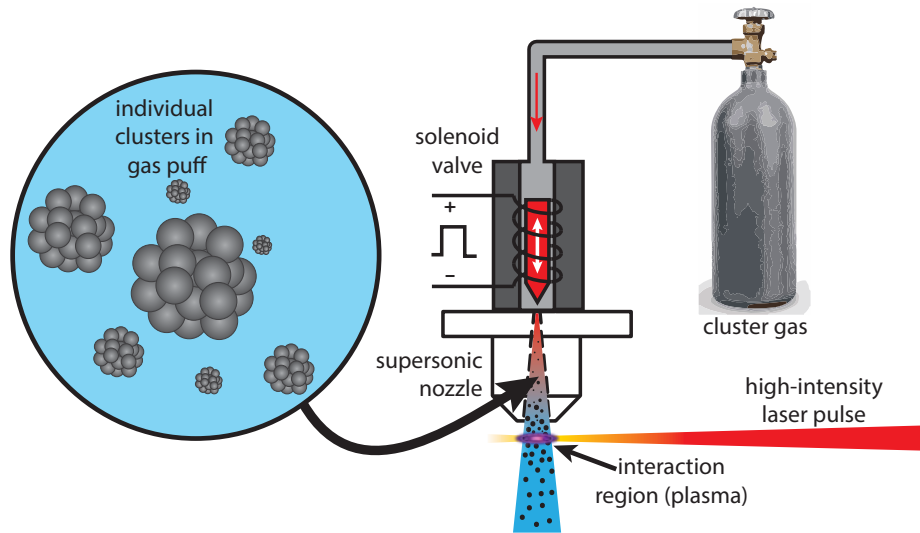


Figure 1.2: Clusters are created by releasing high-pressure (~ 1 MPa) gas through a supersonic nozzle. A high-intensity laser pulse ionizes the cluster plume 2 mm below the nozzle opening.

Not only are clusters excellent absorbers of laser energy, but they also are easy targets to replace. Each pulse of a solenoid valve releases high-pressure gas through the supersonic nozzle into vacuum (open time 0.8–1.0 ms), creating a fresh puff of clusters under the nozzle, as shown in Figure 1.2. This feature provides a significant advantage over solid targets, which, once irradiated, are damaged permanently and must be replaced. Replacement can involve articulation of the target to expose a fresh surface to the laser, or venting of the vacuum chamber to replace the entire target, increasing the experiment’s technical complexity and reducing its repetition rate.

Deuterated clusters have generated special interest due to their ability to exhibit DD fusion. The high intensity laser provides an electric field that extracts most of the electrons from the clusters, resulting in a strong positive charge which

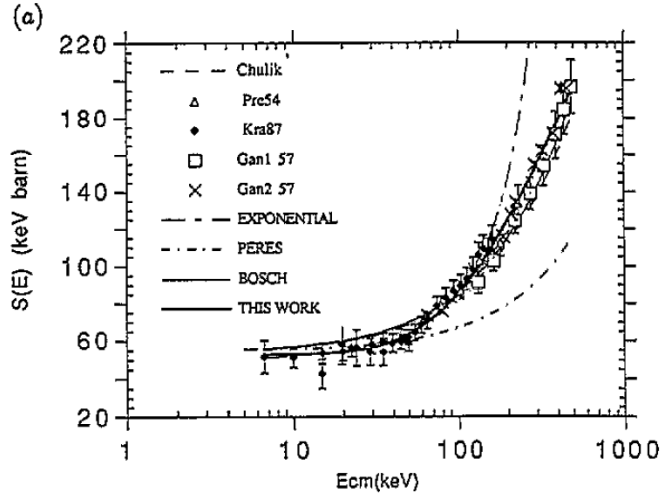


Figure 1.3: Several works have established the energy dependence of DD fusion; the figure above shows several of these, compiled by Erba [16]. Clusters can generate ions with energies of several keV, which can be sufficient to access the low end of the energy range shown.

accelerates the ions to multiple keV. Ideally, the laser pulse duration should be of the order of the ions' response time ($\tau_{pulse} \approx 1/\omega_{pi}$) [5]. If the laser pulse is much slower than this, the ions in the cluster may expand before the laser is gone, and the simplifying assumption of static ions no longer applies. In general, a greater space charge yields a greater ion energy, likely resulting in an increase in the DD fusion rate, as shown in Figure 1.3.

Astrophysics

Astrophysical phenomena and conditions may also present themselves in appropriately formed HED plasmas. Albeit short-lived, the hot, dense plasma formed during the irradiation of a solid target (e.g. a pin or a foil) can mimic conditions within stellar objects, including neutron stars and supernova remnants, as discussed in the literature

review section in [15]. Of particular interest here is the radiative blast wave formed by a supernova launching hot plasma into its surrounding medium. A supernova event initiates a blast wave, an expanding volume with a sharp mass density gradient at its boundary. Within the density gradient (i.e. the shock front), the density falls off smoothly as the radial distance from the blast wave center decreases. Reference [7], from which Figure 1.4 is excerpted, illustrates this radial falloff in numerical solutions for a spherical blast wave.

When blast waves expand into certain media, especially those of high atomic number, the shock will radiate energy, possibly forming a secondary shock, or modifying typical blast wave instabilities [64]. This scenario can be reproduced in the laboratory by irradiating a solid target immersed in a background gas. The laser's interaction with the solid target creates the initial blast wave, and the background gas functions as the surrounding medium. Imposing a strong magnetic field on this blast wave may drive additional effects, or suppress those which are already present [61].

This gas-immersed solid target design enables a study of stellar physics in the laboratory, and provides opportunity for the addition of manipulating effects such as instability seeding or magnetization effects. Such studies could provide insight into the death and birth of stellar bodies and the growth factors of instabilities seen in these situations, and can help refine plasma physics theory by revealing characteristics of instabilities that have yet to be examined experimentally.

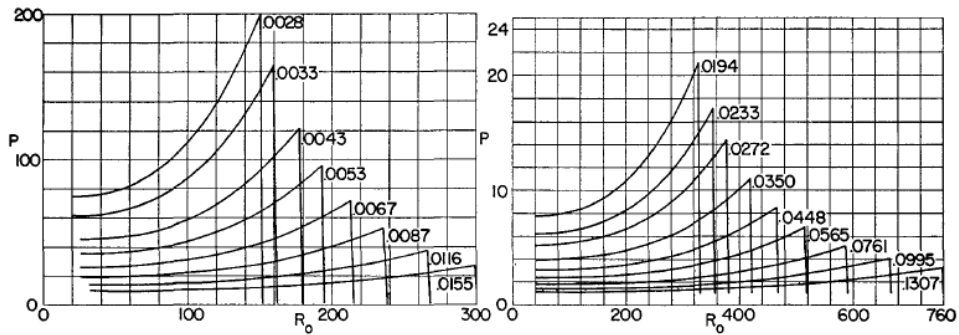


Figure 1.4: Pressure in atmospheres behind a spherical blast wave as a function of radial distance (arbitrary units) from the blast wave center. Each pressure curve is labeled with its time from the start of the blast wave. Please refer to [7] for a discussion of the radial and time scaling in this figure (Figure 4 in [7]), which are dependent on initial conditions.

1.2.2 Electrical discharge

Electrical pulsed power systems can also yield HED conditions by rapidly heating and compressing material to densities approaching that of solids. A well-known architecture is the Z-pinch plasma, which compresses a radially symmetric electrical load like the the wire array shown in Figure 1.5 by driving a current along its surface.

The resulting azimuthal magnetic field compresses the load by the $\vec{J} \times \vec{B}$ force acting on the current passing through the load. This drive current rapidly heats the load and converts it to plasma, and the magnetic field pinches this plasma into its central axis. As the imploding plasma reaches the center, it reaches an extreme of energy and density and stagnates as the internal pressure resists further implosion. For example, the Z Machine at SNL, pictured in Figure 1.6, generates a stagnating plasma which emits an enormous quantity of X-rays, which can drive radiation effects

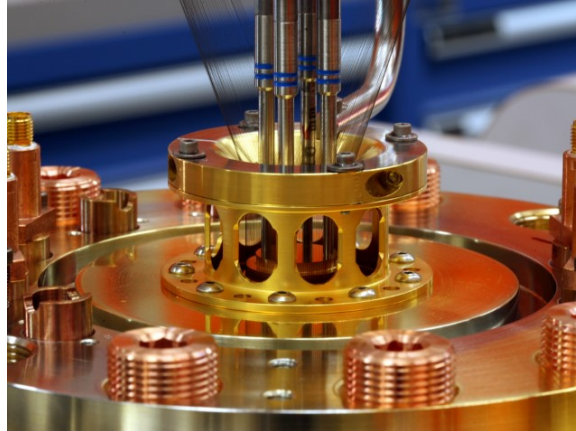


Figure 1.5: Photograph of a Z-pinch wire array for experiments on the Z Machine at Sandia National Laboratories. Photograph from <http://www.sandia.gov/z-machine>.

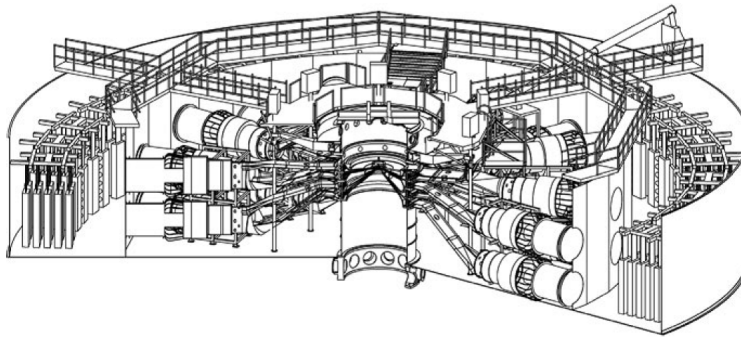


Figure 1.6: Section view of the Z Machine at SNL [4].

in nearby objects. An experimental astrophysics application uses the Z Machine's X-ray emission to drive plasma creation in a nearby gas cell, which simulates white dwarf star photospheres [17, 18].

Another HED physics application is magnetized liner inertial fusion (MagLIF), a developing method of exploring the feasibility of nuclear fusion in an electrically-driven HED plasma [11, 52, 53]. A cylindrical metal liner filled with laser-preheated fuel

(deuterium gas) conducts an axial current on its surface, and compresses under the Z-pinch effect. The collapsing liner also compresses a preexisting magnetic field, and this flux compression magnetizes the plasma within the liner. Concurrent mechanical compression by the imploding liner raises the density of the plasma to a level that is suitable for inertial confinement fusion. Pressures within these targets will reach well beyond the HED threshold of 100 GPa, easily placing MagLIF within the HED plasma regime.

The complete set of HED effects and conditions accessible with laser and electrically driven systems is too vast for the present discussion, but the interested reader will find Reference [9], *Frontiers in High Energy Density Science*, a conveniently sized brief on the blooming research opportunities in this field. Future discussion here will focus on generation of a magnetized HED (or near-HED) plasma with an intense pulsed laser.

Chapter 2

Magnetized plasma experiments

2.1 Related work

MIFEDS

Several facilities have pursued the magnetized plasma regime, both in university and research facilities. The Magneto-Inertial Fusion Electrical Discharge System (MIFEDS) at The University of Rochester's Laboratory for Laser Energetics (LLE) is an augmentation that adds magnetic field capability for fusion experiments on LLE's OMEGA laser [24]. Reference [30] discusses a recent experiment that applied a seed field of 8 T to an inertial confinement fusion (ICF) target filled with deuterium gas. The OMEGA laser irradiated the target pellet, and this produced an imploding plasma shell that compressed the magnetic field within the pellet volume. This flux compression resulted in a magnetized (~ 26 MG) hot spot at the target center, effecting a 30% increase in DD fusion neutron yield.

Z Machine

Z-pinch experiments at the Z Machine at SNL are presently examining the potential for magnetized nuclear fusion with their MagLIF experiments [11, 52, 53]. A high-intensity pulsed laser will irradiate pre-magnetized deuterium gas inside a metal

liner, generating a plasma with an initial magnetic field. As this plasma is formed, the Z Machine’s drive current flows through the liner, compressing it; this also compresses the initial field (magnetic flux compression) and the deuterium fuel. If the magnetic pressure can counter the plasma pressure and confine the fusion plasma, this could prove to be a scientific breakeven fusion source, where scientific breakeven is defined as the condition where the energy used in heating the fuel matches the resulting fusion energy ($E_{fuel} = E_{fusion}$).

Additional facilities

A host of other pulsed power devices, in both academic and professional laboratory facilities, are available. COBRA at Cornell University [23], the gas-puff Z-pinch at the Weizmann Institute [20], MAGPIE in the United Kingdom [41], and the Humboldt High Magnetic Field Centre [48] are some examples. Several universities collaborate with facilities in the operation of pulsed power machines, or develop their own. Some of note are The University of Missouri, The University of New Mexico, and Texas Tech University. Their respective pulsed power capabilities enable these facilities to explore the magnetized plasma regime, although their present research may not be exclusively directed to that end.

2.2 Requirements

2.2.1 High field

A strong magnetic field is the key ingredient to accessing the regime of magnetized HED plasmas—that is, a field whose magnetic energy density is comparable to

the energy density of the plasma: $B_0^2/2\mu_0 \sim nkT$. Given the energy density threshold of ≥ 100 GPa for an HED plasma, the field must meet the requirement that $B_0 \geq 500$ T. This presents a significant technical challenge: permanent magnets of this strength are not available, and the electric current that would generate such a field with a direct current (DC) electromagnet would be impractical using present technology.

Field lifetime > plasma lifetime

Pulsed generation can provide sufficiently strong fields, but the field must be essentially uniform during the plasma's lifetime. This places a lower bound on the duration of the field. A laser-produced cluster plasma, for example, is at HED conditions for a few nanoseconds, requiring the magnetic field to hold a constant value for several nanoseconds to magnetize the plasma. This duration constraint is not necessarily a problem; pulsed power systems usually have pulse lengths of the order of 100 ns or more. For example, the Z Machine's high-current pulse is about 100 ns long.

Mechanical forces

Mechanical stressing of high field (≥ 10 T) components can result in damage or destruction of the field-generating element. The 300 T pulsed field driver in the National High Magnetic Field Laboratory (NHMFL) at Los Alamos National Laboratory (LANL) [51] demonstrates this with remarkable clarity in Figure 2.1. The degree of damage depends on the coil's structure, material, and peak field, but this is a pervasive concern when designing strong magnets. This is primarily caused by the magnetic pressure experienced by conductors bordering a strong magnetic field. The pressure from such a field is given by $p_{mag} = B^2/2\mu_0$, and is relevant in transmission



Figure 2.1: Left to right, a high-field (~ 200 T) coil before and after a shot. Magnetic pressure within the copper loop explodes the coil. Images courtesy of C. Mielke, LANL [57].

lines that carry high current, and in the field-generating element itself. The field driver must have countermeasures to avoid damage to sensitive components from this pressure, or must be designed to withstand it. Usually, these high-field coils are designed to be replaced easily, since in most cases the coil will be rendered unusable after one shot.¹

2.2.2 Operation in vacuum

For the field generating system to be useful in laser plasma experiments, the magnetized volume must be in high vacuum ($\leq 10^{-4}$ Torr). This is a necessity when using high-intensity laser pulses, which will self-focus and filament in poor vacuum, robbing the target of a significant portion of the pulse energy. In practice, this requirement usually means the field-generating element must be in vacuum as well. As the field source becomes more complex, this constraint becomes increasingly difficult

¹The National High Magnetic Field Laboratory (NHMFL) at LANL has magnets that can repeatedly withstand fields of 40–70 T, and are presently developing a 100 T design.

to meet. This vacuum operation requirement is challenging; with the coil inside the vacuum chamber, the sizable drive current (usually at least 1 MA) must be fed through the vacuum chamber wall.

2.3 Pulsed field generation

2.3.1 Pulsed power

Generating a short-duration, strong magnetic field encourages use of the pulsed magnetic field approach. A device capable of generating a sufficiently strong magnetic field that lasts at least the plasma lifetime should be possible with a pulsed, high current driver.

Definition

Pulsed power is a broad term that applies to systems that store electrical energy slowly (~ 10 s) and release it within an interval of several nanoseconds to microseconds. In addition, the peak output power is in the gigawatt range, with a pulse energy of at least a kilojoule [4]. Despite the high power output, pulsed power devices can fit within a modest laboratory space by utilizing this concept of pulse compression. Pulsed power devices that are built on this concept can store energy in a slowly-charged capacitor bank and rapidly release it into a load, as in Figure 1.1. Specialized circuits designed for rapid discharge of large amounts of energy can reach high currents without bulky, high-power current sources. For example, suppose a capacitive storage bank in a pulsed power system is charged for one minute. If this bank releases its stored energy within one microsecond, it will output 6×10^7 times

more power than the power that charged the bank, neglecting losses. Such a device may only occupy the floor space of a modest apartment, depending on the size of the capacitor bank.

This pulse compression is made possible with a circuit that has very low system inductance (L), which is a defining characteristic of a capacitive-storage pulsed power device. As the inductance diminishes, the time to reach peak current also diminishes since it approximately scales with $L^{-1/2}$.

With fast pulses, all elements of the circuit must be considered as transmission lines, each with a length and characteristic impedance. Due to the high currents generated by pulsed power systems, purely resistive elements are minimized to avoid wasting power in resistive heating, although a small resistance can be beneficial by limiting the voltage reversal, which is damaging to capacitors. Parasitic capacitances account for a small fraction of the system capacitance; the capacitance of the charging bank far exceeds these incidental capacitances. However, even a change of a few nanohenries in system inductance will make a notable difference in performance, since well-designed pulsed power devices tend to have very low inductances, making those small changes significant. Specialized low-inductance capacitors, transmission lines, and switches are necessary parts of a high-performance, capacitor-driven pulsed power system.

Applications

Pulsed power has wide applications in HED physics, and its specialization is greatly determined by the load attached to the system. For example, high magnetic field

experiments may use single-turn coils, while Z-pinch experiments may use cylindrical wire arrays. Still others use a cylindrical gas-puff Z-pinch, or a thin metal liner. Regardless of the load configuration, high magnetic fields play a crucial role in driving the physics of the experiment.

2.3.2 Pulsed power capabilities

High field generation

Pulsed power current drivers can routinely generate peak discharges of one to tens of megaamperes, and can drive high field experiments given the appropriate load. In the case of Z-pinches, the azimuthal field through the conductive target quickly pinches the target toward its axis of symmetry. This effect is useful in schemes which utilize flux compression, such as the MIFEDS and MagLIF experiments. In other cases, the current flows through a coil, usually single-turn, to generate a strong field within the coil volume, such as in [40, 48].

In the case of a cylindrically symmetric field source (e.g. a single-turn coil), treating the coil as a collection of many current filaments through the conductor's cross-section can model the changing current distribution and resulting forces [42, 45–47]. Such a model can also closely predict discharge behavior as the coil changes its inductance during the discharge due to its expansion. Field calculations for these models are based on the Biot-Savart law, which describes the magnetic field \mathbf{B} as a function of position vector \mathbf{r} from an infinitesimal current element to the point of interest:

$$\mathbf{B} = \frac{\mu_0}{4\pi} \int_C \frac{I d\mathbf{l} \times \mathbf{r}}{|\mathbf{r}|^3}, \quad (2.1)$$

where I is the current through the infinitesimal line element $d\mathbf{l}$. Numerical modeling of current distribution gives a better sense of field evolution, but is more complex.

Although it sacrifices accuracy, simplifying the field source by treating it as a pair of infinitesimal current loops will facilitate an intuitive understanding of field scaling with coil dimensions and current. The on-axis field from a single infinitesimal current loop is given by applying Equation (2.1) to the single-loop case:

$$B_z(z) = \frac{\mu_0 I R^2}{2(z^2 + R^2)^{3/2}}, \quad (2.2)$$

where I is the total current through the loop, and R is the radius of the loop. Taking two such loops separated by a distance of $2z_0$, each carrying half the total current, the on-axis field is given by

$$B_z(z) = \frac{\mu_0 I R^2}{2} \left(\frac{1/2}{((z - z_0)^2 + R^2)^{3/2}} + \frac{1/2}{((z + z_0)^2 + R^2)^{3/2}} \right). \quad (2.3)$$

At the coil center ($z = 0$), this simplifies to

$$B_z(0) = \frac{\mu_0 I R^2}{2(z_0^2 + R^2)^{3/2}}. \quad (2.4)$$

Two conclusions are immediately clear: coil geometry has a major effect on field strength, and field varies linearly with current. In an example two-loop coil with an ID of 1 cm and end-to-end length $2z_0 = 1$ cm, a current of $I = 1$ MA will yield

an on-center field strength of 44 T. This is a considerable percentage of the HED threshold of 500 T, and can be sufficient to influence a near-HED plasma. An array of current filaments distributed throughout the coil's cross-section will better predict field strength, at the cost of increased complexity. Although it is not a complete picture of the coil's field profile, Equation (2.4) can give order-of-magnitude estimates, which is helpful for initial coil design.

Vacuum operation

Operation in vacuum is a technical challenge, since it is not practical to enclose the entire pulsed power system in vacuum. A pulsed power system design that will drive a load in vacuum must include a scheme for feeding the high current into vacuum. Specially designed feedthroughs are necessary for pulsed power applications, since common vacuum feedthroughs are not designed to meet the constraints of low inductance and high current. Fortunately, the power transmission line itself can function as a feedthrough, with sealing insulators as vacuum barriers. These insulators are shaped to discourage dielectric tracking, a damaging phenomenon that short-circuits the transmission line by establishing an arc across the surface of an insulator. Machinable plastics are ideal for these insulators, since they will form a portion of the vacuum vessel. An excellent choice is Rexolite[®] 1422², a cross-linked polystyrene with the additional benefit of excellent vacuum performance, which reduces the contribution to the poor vacuum quality that usually accompanies plastic components. Acetal resin is a cheap alternative, but its dielectric and vacuum properties are inferior to

²C-Lec Plastics, Philadelphia, PA 19135

Rexolite's. Ceramics are also good insulators, and some are vacuum compatible, but their fragility and poor machinability limit their usefulness in this application.

2.3.3 Special considerations

A pulsed magnetic field driver is susceptible to effects that can inhibit optimum performance, and these effects impose special constraints on the driver's design. The effects discussed here fall under three general categories: electrical breakdown (arcs), magnetic pressure, and field coil destruction.

Electrical breakdown

High voltage breakdown of the medium between high voltage elements is a major consideration in pulsed power design. All else being constant, reducing the separation between transmission line elements will reduce inductance, but will increase the electric field strength across the gap and consequently will increase the chance of breakdown.

1) **Paschen breakdown** Of principle concern is the Paschen breakdown, a spontaneous electric breakdown of a gas within the gap between two electrodes. The gap width (d), which is filled with a gas at some pressure (p), has a maximum voltage associated with the product of those two variables,

$$V_B = \frac{Bpd}{\ln [A pd / \ln (1 + 1/\gamma)]}, \quad (2.5)$$

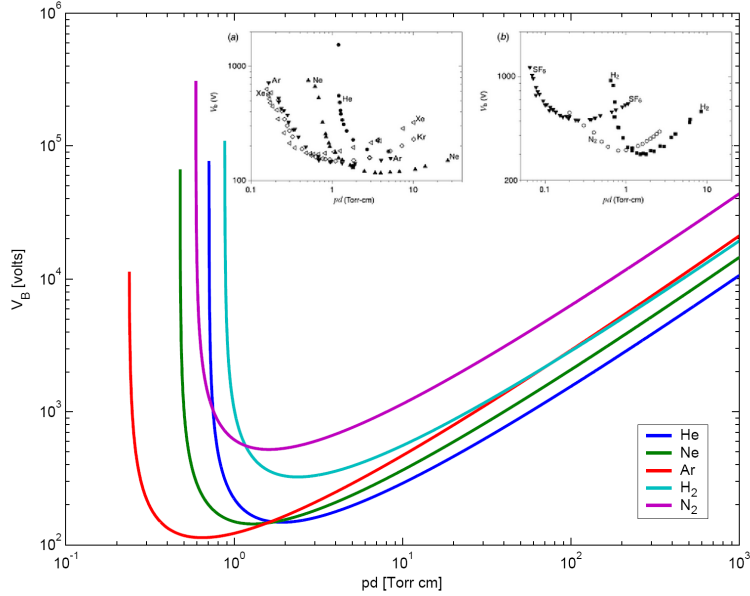


Figure 2.2: Paschen breakdown voltages for parallel plate electrodes with various gases at 20° C [10, 35].

where A and B are constants particular to the gas being used. The γ factor is the secondary electron emission coefficient; an avalanching (Townsend) breakdown will occur for $\gamma \geq 1$ [4].

Above V_B , spontaneous electric breakdown will occur in the gas. An example Paschen breakdown curve in Figure 2.2 maps the maximum hold-off voltage for a given pd product, under ideal conditions. This is useful in determining the hold-off voltage in the transmission line, which will have some voltage across its gap due to the inductive voltage given by

$$v(t) = L \frac{di(t)}{dt}. \quad (2.6)$$

The transmission line should be designed such that the gap distance is able to hold

off the inductive voltage at the operating pressure of the gas filling the transmission line. However, Equation (2.6) does not capture the whole picture. Phenomena such as reflections at transmission line transitions may cause voltage spikes that add to the predicted voltage. A detailed transmission line calculation can reveal these voltages. In practice, surface conditions and material composition of the electrodes may reduce the hold-off voltage, and practical pulsed power engineering demands consideration of such features that can lower the hold-off voltage.

As an example, with air at 1 atm ($p = 760$ torr) and a gap voltage of $V_B = 10$ kV, the gap d should be at least 2 mm under ideal conditions. If $d = 1$ cm, it follows from a similar analysis that if $0.6 \leq p \leq 160$ torr, the air gap will break down. This low pressure range occurs during evacuation; if the system is to be operated in vacuum, this pressure range must be avoided. Such pressures are not considered high-quality vacuum, and are not likely to exist in an experiment unless there is a leak in the vacuum system preventing sufficient evacuation, or a localized region of higher pressure (e.g. outgassing or virtual leaks).

It is important to consider that an experiment involving gas can cause a Paschen breakdown if the gas is allowed to enter a high voltage region. Even if the overall pressure of the experiment does not suggest Paschen breakdown, a localized region with higher pressure can pose a threat to the experiment's success. During a pulsed discharge, the current will tend to follow the least inductive path, which arcs can provide. The arc will redirect the current, effectively shorting the desired path, wasting the discharge, and usually damaging the conductor surfaces at the arc site. For experiments involving gas targets, the gas flow must be contained, or directed

away from the high voltage conductors during the discharge.

2) Field emission Very strong electric fields at a metal surface can cause electron emission in vacuum, without the need for a triggering event to initiate the emission. This phenomenon can be troublesome for high-voltage transmission lines, especially where the anode-cathode (A-K) gap narrows, which increases the electric field. Strong electric fields can distort the potential barrier that binds the electrons to the metal, allowing the electrons to escape freely into the vacuum by tunneling, a quantum mechanical effect. This is described by the Fowler-Nordheim equation

$$j = \frac{1.54 \times 10^{-6} \beta^2 E^2}{\phi} \exp \left(-\frac{6.83 \times 10^7 \phi^{3/2} \theta(y)}{\beta E} \right), \quad (2.7)$$

$$\theta(y) \approx 0.956 - 1.06y^2,$$

$$y = 3.8 \times 10^{-4} \frac{\sqrt{E}}{\phi},$$

which gives the tunneling current j as a function of the metal work function ϕ , surface enhancement factor β , and electric field E [4]. In recent literature, an electric field strength of 200 kV/cm is the typical threshold for electron emission from commonly used transmission line materials like aluminum and stainless steel.

The electric field in the A-K gap can accelerate this tunneling current, leading to vacuum breakdown (flashover). Design review of the vacuum section of the transmission line in the Z-Machine at SNL discusses this possibility in [54]. Empirical data from [37] formed the background for the design principle that field emission can usually be avoided by keeping $E \lesssim 100$ kV/cm. Furthermore, the Z-Machine's vacuum insulator causes a field enhancement at the triple point junction of the insulator,

cathode, and vacuum regions; at this position, the design principle is even tighter with $E \lesssim 30$ kV/cm [56]. Recent literature continues this discussion of the flashover behavior at the vacuum insulator interfaces, particularly in Reference [59].

A field of 100 kV/cm is extremely strong, but may be possible in some cases, and sometimes unexpectedly due to voltage ringing. This can be caused by a resonance in the circuit, or by a circuit that suffers from poor impedance matching. This voltage ringing appears as a high-frequency oscillation superimposed on a slowly-varying primary voltage pulse. This ringing, although short-lived, can produce transient voltage pulses that raise the total voltage several times higher than the voltage predicted by Equation (2.6). If this voltage exists in vacuum across a sufficiently narrow A-K gap, the electric field in the gap can exceed the tunneling threshold, causing field emission which may then drive vacuum flashover.

3) Ultraviolet (UV) illumination Emission of UV light from contact surfaces can be responsible for liberating photoelectrons from the cathode, and in a sufficiently strong field, these electrons may be accelerated to energies high enough to initiate an arc. A poor joint between conductors can cause contact arcing, which can be a source of UV light. Metal compression gaskets can address this by providing a conductive seal between conductors; another suitable solution may be obstructing lines of sight between the UV source and the cathode surfaces.

4) E_θ induced electric field An axially-directed magnetic field, as is generated by a solenoid, induces an electric field encircling the field lines. From the integral form of

Faraday's law,

$$\oint_{\partial S} \mathbf{E} \cdot d\mathbf{l} = - \iint_{\mathbf{S}} \frac{\partial \mathbf{B}}{\partial t} \cdot d\mathbf{S}, \quad (2.8)$$

it is apparent that the more cross-sectional area the magnetic field penetrates, and the more rapidly the magnetic field changes, the greater the electric field at that area's boundary. We identify this electric field as the E_θ field, since the field is directed along the angular basis vector in cylindrical geometry. If driven to sufficient magnitude, the E_θ field may initiate an arc around the field lines. In the example of a solenoid with an ID of 1 cm, generating an axial field such that $\partial B_z / \partial t = 100$ tesla/ μ s, E_θ along the inner boundary of the coil surface is 2.5 kV/cm. The coil's loop voltage, neglecting the "legs" of the coil, is $2\pi R E_\theta \approx 8$ kV. This voltage may serve as an accelerating field for electrons released by UV illumination, or may initiate Paschen breakdown. The presence of a gas in the magnetized region will likely amplify the possibility of Paschen breakdown, if the loop voltage exceeds the breakdown voltage V_B .

Magnetic pressure

Strong magnetic fields produced by high currents imposes a pressure ($p_{mag} = B_0^2 / 2\mu_0$) on the conductors bounding the field. With pulsed power, the magnetic field diffusion time can exceed the pulse duration, therefore at first, the internal field is much greater than the external field. The time for the magnetic field to penetrate a conductor can be approximated with

$$\tau_m = \mu_0 L^2 / \rho \quad (2.9)$$

where L is the length scale of magnetic field variation, and ρ is the resistivity of the conductor [8]; for copper, $\rho = 1.725 \times 10^{-8} \Omega \cdot \text{m}$ [28]. For a pulsed power system, the

magnetic field's length scale L should be the skin depth δ , shown in Equation (2.10). Supposing a skin depth of $176\ \mu\text{m}$ for a drive current frequency of $140\ \text{kHz}$, we find $\tau_m = 2.27\ \mu\text{s}$. This is a relatively long time in terms of many pulsed power systems, including the one discussed in this work.

Before diffusing through the conductor, the magnetic field can exert tremendous pressure on the transmission line, and can damage or destroy structurally vulnerable components. This magnetic pressure is the manifestation of the magnetic field acting on the charge carriers in the surrounding conductor. By analogy, the conductors attempt to expand to reduce the magnetic energy density ($p_{mag} = B^2/2\mu_0$) in the same way that a balloon expands in response to increasing gas pressure ($p = nkT$).

This expansion force will appear in the transmission line segments leading to the coil, and the transmission line must be designed to withstand this force. In an example of a $1\ \text{MA}$ discharge into a narrow ($w = 10\ \text{cm}$, $h = 2\ \text{mm}$) final segment of a two-plate parallel transmission line pictured in Figure 2.3, the magnetic flux density within the line is $12.6\ \text{T}$. This gives a pressure of $62.8\ \text{MPa}$ between the plates, or a force of $62.8\ \text{kN}$ between a $10\ \text{cm} \times 1\ \text{cm}$ strip. If the design allows, such parallel plate lines should be avoided since they require clamping to prevent bulging during a discharge; coaxial or conical transmission lines can better withstand these expansion forces. Multi-plate transmission lines are even more preferable since they divide the current among several conductors, reducing the magnetic pressure between them. Furthermore, this multi-plate design can balance the magnetic pressure forces on inner conductors, such as the center conductor of a triplate line.

The magnetic pressure within the field coil can cause expansion, necking,

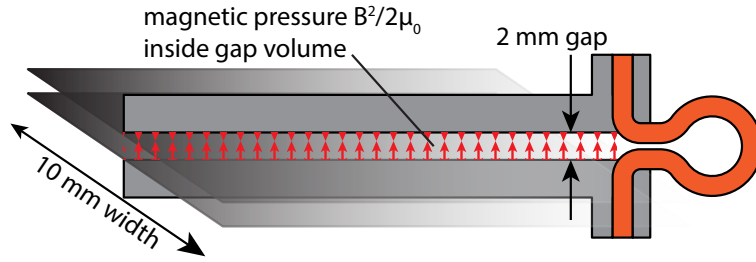


Figure 2.3: Magnetic pressure coming about from current flow along a parallel plate transmission line will push the plates apart. Damage can result if the design is not suited for this pressure.

fragmentation, or tearing. Which failure modes dominate depends greatly on the field strength and the coil design. Massive, heavily reinforced coils such as those found at the National High Magnetic Field Laboratory (NHMFL) at LANL can withstand the pressures that accompany their high fields (40–70 T). Other systems such as the ones described in [48] and [40] use expendable coils which are replaced every shot. Pressures of at least 1 GPa are common in high field experiments; a 2 cm ID Helmholtz coil driven by a 1 MA pulse will experience 800 kPa (510 kN) on its inner surface.

Destruction of field coil

With the likely destruction of the field coil above 40–50 T, expendable coils are the obvious choice, with emphasis on minimizing fabrication expense. Copper is relatively malleable, and is inexpensive compared to the advanced materials used in multi-shot high field coils. The 2 cm ID Helmholtz coil discussed in the last section, if made from 3 mm-thick copper bar, would certainly not withstand the internal 510 kN force.

Coil melting also contributes to coil destruction. Even copper’s excellent

conductive properties allow some resistance, which is heightened by the effective reduction of conductor cross-section due to the skin effect. This effect is a result of the pulsed nature of the discharge, which has a characteristic frequency related to the circuit parameters. A pulsed power system is by nature an RLC circuit, with a resonant frequency generally in the radio frequency (RF) range. In a highly conductive material, the current will tend to flow mostly on the surface layer of the conductor; this effect is heightened as frequency increases. The current's distribution into the conductor's depth is expressed by

$$I(x) = I_S e^{-d/\delta}, \quad \delta = \sqrt{\frac{2\rho}{\mu\omega}}, \quad (2.10)$$

where I_S is the current at the surface, d is the depth below the conductor's surface, ω is the angular frequency of the oscillating current and ρ and μ are the material's resistivity and magnetic permeability, respectively. Given a frequency of 140 kHz, the skin depth (δ) in copper is 174 μm . For the 2 cm ID Helmholtz example, a uniform current distribution along the coil's length (1 cm) will give a current density of $5.7 \times 10^{11} \text{ A/m}^2$. This current through the length of the coil loop will dissipate 149 J in the 607 $\mu\Omega$ resistance of the skin layer during the first 3.6 μs half-cycle of the discharge. Considering the volume of the skin layer, and copper's material properties, this can raise the temperature of the skin layer by 441 Kelvin. Copper's melting point is 1356 K, suggesting melting will not occur unless the current becomes concentrated in a smaller cross-section of the coil. A numerically calculated, time-resolved simulation of current distribution predicts this concentrating effect will become more pronounced as the discharge proceeds.

Chapter 3

MegaGauss 2, a pulsed magnetic field driver

3.1 Origin

To extend the cluster fusion and astrophysical blast waves experiments discussed in Section 1.2.1 into the magnetized regime, Sandia National Laboratories (SNL) and The University of Texas at Austin (UT-Austin) developed a portable pulsed power system designed to deliver up to 2.2 MA into a single-turn coil inside a vacuum chamber. This system was initially named MegaGauss (MG1), and later renamed to MG2 after upgrading the initial 31 kJ capacitor bank to a 160 kJ bank. The principle of minimizing total circuit inductance guided the design process, from component selection to power transmission geometry.

3.1.1 Initial design from Sandia Labs

The SNL/UT-Austin collaboration began with a prototype pulsed power driver, designated MG1, which was designed to reach 500 kA with a two-capacitor 31 kJ bank. Magnetized cluster fusion was the primary objective of this system, and MG1 was the first step in the development of the field driver for that experiment. The

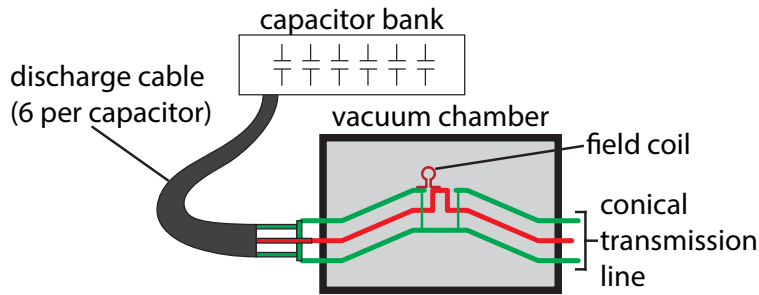


Figure 3.1: Current from a capacitor bank flows through coaxial cables to a central chamber that accumulates current from all capacitors. Within this chamber, a vacuum-insulated conical transmission line directs the current to the load, which is situated on the top of the conical line.

capacitor bank fed into a three-level conical transmission line through a parallel array of 12 discharge cables (6 per capacitor), which directed the discharge current into a single-turn coil at the transmission line center. A vacuum vessel enclosing the bulk of the transmission line enabled vacuum operation. Figure 3.1 shows a simple schematic of these elements.

In Summer 2011, a larger, 160 kJ, ten-capacitor bank replaced the original MG1 capacitor bank. New triplate transmission line components accepted up to 60 discharge cables, and a master trigger distribution circuit replaced the MG1 direct triggering scheme. While the larger capacitor bank required upgrades of peripheral components like the charge dump circuit and control electronics, the overall design remained unchanged.

Operation of the cluster fusion gas jet presented the technical difficulty of a gas in the transmission line. The original design called for vertical injection of the cluster jet, but this consistently produced arcing in the anode-cathode (A-K) gap

near the target. Diversion of the cluster gas away from the A-K gap successfully countered this problem, but appeared to disrupt the cluster formation process. Initial MG1 cluster jet trials and subsequent confirmation with MG2 indicated the design needed modification to accommodate the clusters. Vacuum operation also presented a problem at high voltage: high current shots (~ 1 MA) often arced during vacuum operation, although the background pressure was in the 10^{-4} or 10^{-5} range, the limit of our vacuum capability.

3.1.2 Modification at UT-Austin

Cluster fusion accomodation

In response to the cluster injection and vacuum arcing challenges, we further modified the MG2 design. Moving the cluster jet to a horizontal orientation avoided injecting the cluster jet into the triplate line's A-K gap. This allowed the cluster jet to enter one side of the single-turn coil and exit the opposite side, making the gas flow parallel to the A-K gap. This modification redirected the gas, but brought the metal parts of the gas jet apparatus closer to the high-voltage transmission line.

Breakdown avoidance in vacuum

Chamber operation at atmospheric pressure during early MG2 trials was consistently successful, but operating at vacuum presented a major challenge since the chamber arced under many conditions. A major redesign of the target chamber, shown in Figure 3.2, took advantage of this atmospheric insulation by reducing the vacuum volume to a small region around the single-turn coil. This kept all the elements of

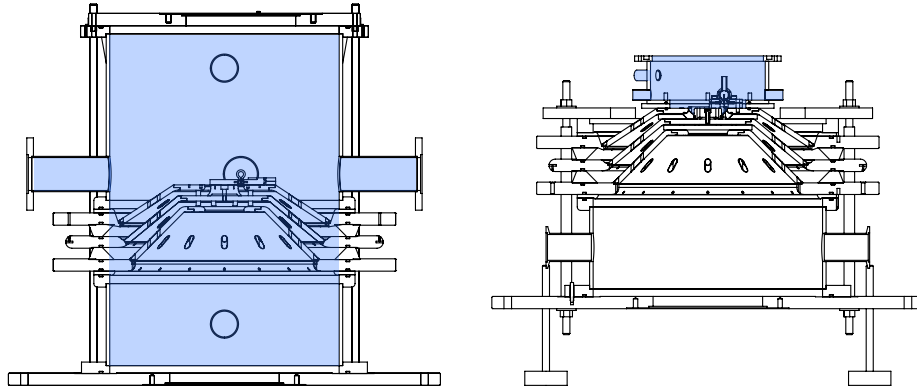


Figure 3.2: Left: The original design from Sandia National Laboratories (SNL) used a large vacuum chamber (~ 90 L volume), which included the triplate transmission line in the vacuum volume. Right: A smaller vacuum chamber (~ 3 L) fixed to the top of the transmission line reduced the vacuum volume, and avoided technical difficulties arising from operating the transmission line in vacuum. Highlighted portions of the schematics indicate vacuum volumes.

the triplate line at atmospheric pressure, except for the top face of the cathode and a small portion of the anode, as shown in Figure 3.5. The coil is in the reduced vacuum volume, and connects to the top face of the triplate line as originally designed. This adjustment eased troubleshooting by reducing the breakdown-susceptible surface to a smaller, more accessible region. Along with strategically placed Mylar[®] film insulation, this upgrade succeeded in reducing premature arcing during vacuum shots.

These design changes apply to the following discussion of the MG2 system, which will discuss each component of the system in detail. After the design discussion, a simplified circuit schematic of the MG2 system will provide a predictive model for discharge behavior. Current and field measurements support the model predictions.



Figure 3.3: The entire MegaGauss 2 system at The University of Texas at Austin. All ten capacitors are connected to the central vacuum chamber. The control electronics rack and charge and trigger distribution tanks are visible in the background.

3.2 Design

3.2.1 Portability

Pictured in Figure 3.3, MG2 is designed to be portable enough to enable use at multiple facilities, primarily UT-Austin and SNL. Its modularity highlights this design feature in that the MG2 charge bank is composed of up to 10 current source modules in parallel. This allows flexibility in the capacitor bank size, providing portability and scalability.

The target chamber includes a three-layer (tripla)te), radial/conical transmission line that directs the individual discharges from the current modules to the load. The discharge cables from each module couple into the flattened perimeter of the

transmission line (outer diameter (OD) 60 cm). Casters on the aluminum base under the transmission line allow easy transport; the chamber is also lightweight enough (~ 90 kg) to be lifted with a common laboratory hoist. The charge dump circuit, master trigger circuit, and electronics control enclosure are on rolling platforms and can be moved independently of the other MG2 components. A control computer, and the digitizing oscilloscopes that record the discharge behavior are necessary, but are not unique to the MG2 system, and any arrangement that meets the basic computing and data acquisition requirements will suffice.

3.2.2 Vacuum compatibility

Generation of the high magnetic field must occur in vacuum to support MG2's designed purpose of providing a magnetic field for laser plasma experiments. The anode and the top surface of the cathode serve as the bottom of the vacuum chamber. The chamber's wall is cylindrical, with an O-ring at its top which seals against a lid, and several flanged vacuum ports provide access into the chamber volume for evacuation, laser propagation, gas feed lines, and electrical interconnects. The vessel is made of stainless steel and is strong enough to function as a debris shield, which is crucial for high-field, destructive shots. Figure 3.5 shows an angled dielectric insulator at the chamber's bottom that both provides an atmosphere-vacuum barrier, and insulates the transmission line components. The angling of the insulator prevents charge buildup along the insulator surface, which can result in arcing across the insulator (dielectric tracking) [4]. This is similar to the angled insulators on the original vacuum chamber, detailed in Figure 3.4.

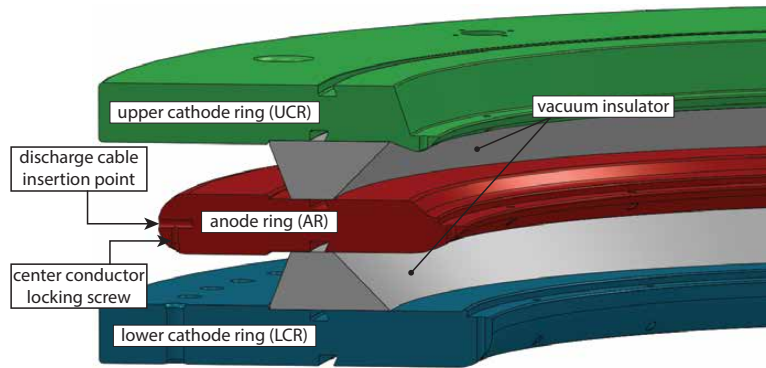


Figure 3.4: Detail view of original vacuum insulators as designed at Sandia National Laboratories. Space enclosed (right) by insulators is vacuum volume. Discharge cables connect to the atmosphere (left) side, as in Figure 3.8. Additional elements of triplate and chamber are suppressed to show features.

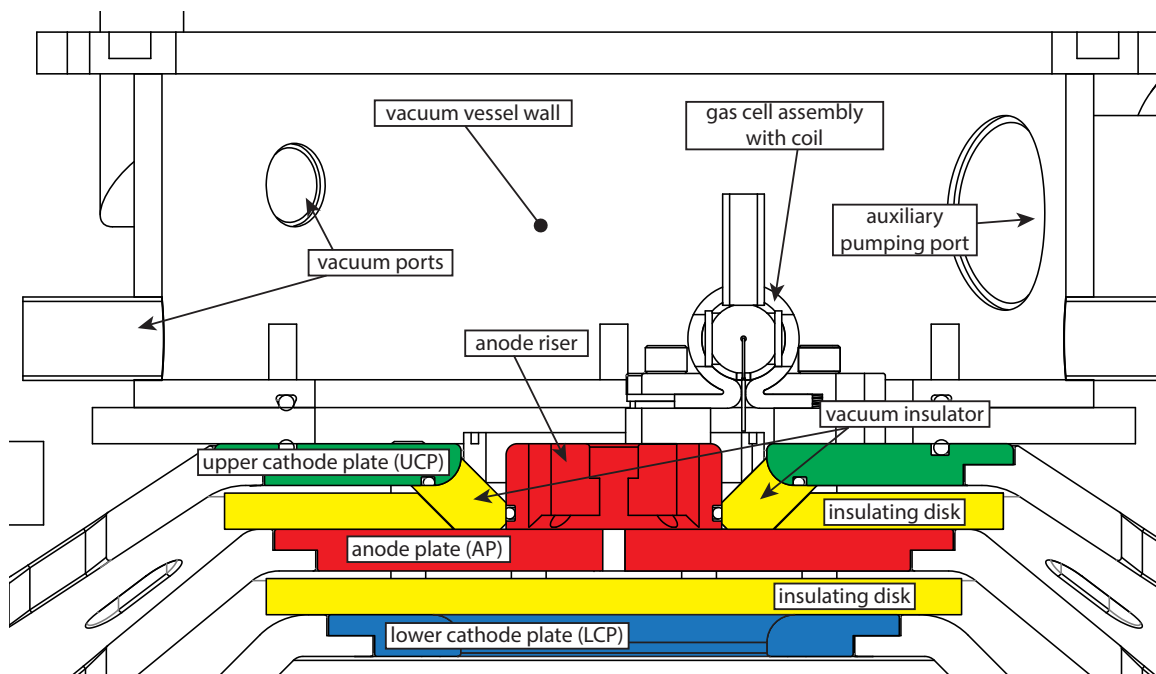


Figure 3.5: Detail view of vacuum insulator. Space above angled insulator is vacuum volume, which is enclosed by the small chamber atop the upper region of triplate transmission line. Also visible: 3/4 inch blast wave target, which is detailed in Section 4.2.1, and insulating disks between triplate layers.

Capacitors used in bank	Capacitor inductance	Switch enclosure	Discharge cables	Triplate line	Coil	Total
1	40	71	139	5	10	265
2	20	35.5	69.5	5	10	140
10	4	7.1	13.9	5	10	40

Table 3.1: Effective inductances of MG2 components for different capacitor bank configurations. All values are in nH and are estimates using ideal conditions, except for capacitor inductance, which is specified by the manufacturer as an absolute maximum. These values correlate with Figure 3.16.

3.2.3 Low inductance

Minimizing inductance will increase peak current and reduce the rise time, defined here as the time from discharge onset to peak current (0% to 100%). The MG2 design uses components selected and designed to minimize inductance, and their inductance values are listed in Table 3.1. The capacitors and spark gap switches are commercially manufactured, and their inductances are not adjustable. All other components of the discharge circuit are adjustable in geometry, design, or both, allowing manipulation of the total inductance.

A series of coaxial lines yields an estimate of the inductance of the switch enclosure assembly, as pictured in Figure 3.6, and these coaxial elements can be customized to minimize inductance. Bundling six discharge cables reduces the inductance incurred by power transmission from the current module to the triplate line. This inductance could be reduced further with more cables, but the perimeter of the triplate line would be unable to accommodate more cables without a major alteration. Total inductance

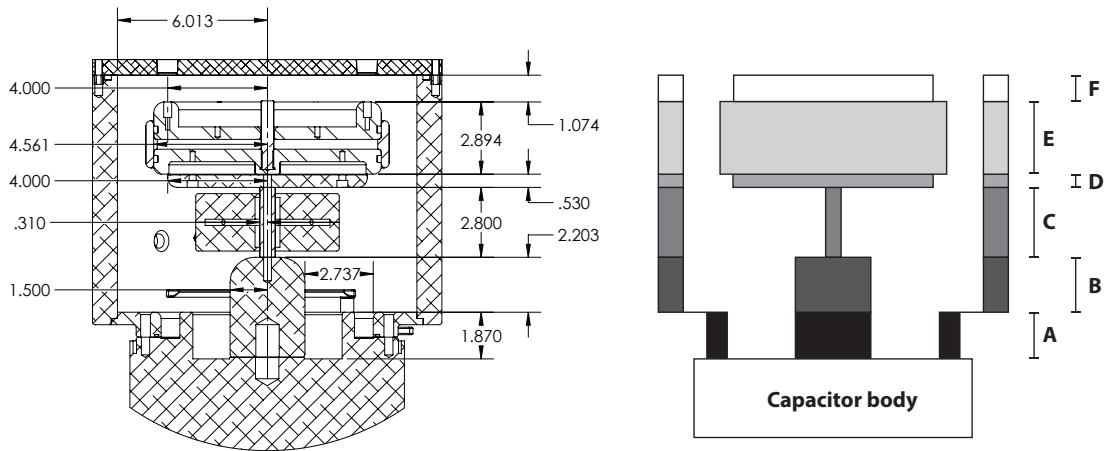


Figure 3.6: Approximation of switch enclosure components to coaxial segments. Left: section view of an enclosure. Right: coaxial transmission line simplification. Segments A–B: capacitor terminal, C: spark gap switch (electrode diameter), D–E: salt water resistor, F: discharge cables. Values for each segment are listed in Table 3.2.

Segment	Inner radius (in)	Outer radius (in)	Length (cm)	Inductance (nH)
A	1.50	2.74	4.75	5.7
B	2.74	6.01	5.60	15.5
C	0.31	6.01	7.11	42.2
D	4.00	6.01	1.35	1.1
E	4.56	6.01	7.35	4.1
F	4.00	6.01	2.73	2.2

Total inductance: 70.8

Table 3.2: Estimated values for inductance of switch can enclosure components. All elements are approximations to a coaxial transmission line with dimensions from Figure 3.6.

of the central transmission line is estimated at 5.7 nH [58]; the remaining circuit inductance is that of the load, which varies. For a single-turn coil with a 1 cm ID, the load inductance is approximately 10 nH under the simplifying assumption of a long, single-turn ($N = 1$) solenoid: $L = \mu_0 N \pi R^2 / \ell$, where R is the solenoid radius, N is the number of turns, and ℓ is the solenoid length. This represents 25% of the estimated system inductance when the system is configured to use the full 10-capacitor bank.

3.2.4 Construction

Current source modules

A parallel array of up to 10 current source modules, one of which is shown in Figure 3.7, compose the charge bank. Each module consists of six key elements: 1) a 3.2 μF oil-filled, low-inductance capacitor³, 2) a threaded transition stub screwed onto the central (positive) terminal of the capacitor, 3) a spark gap switch⁴ that gates the capacitor discharge, 4) a small salt water trigger resistor ($\sim 1 \text{ k}\Omega$) into the switch's trigger terminal, 5) a large, axial salt water resistor ($\sim 100 \text{ m}\Omega$), and 6) a cylindrical enclosure that contains elements 2 through 6.

The open bottom of the switch enclosure bolts to the outer (negative) terminal of the capacitor, and functions as the current's return path into the capacitor. The top plug of the water resistor has six receptacles for the discharge cables, and the cables pass through O-ring feedthroughs in the enclosure's lid. Additional feedthroughs

³General Atomics Energy Products, Series PDS/PDSS high voltage fast pulse capacitors, San Diego, CA

⁴Titan 40364 spark gap switch, L-3, Pulse Sciences Division, 2700 Merced Street, San Leandro, CA, 94577

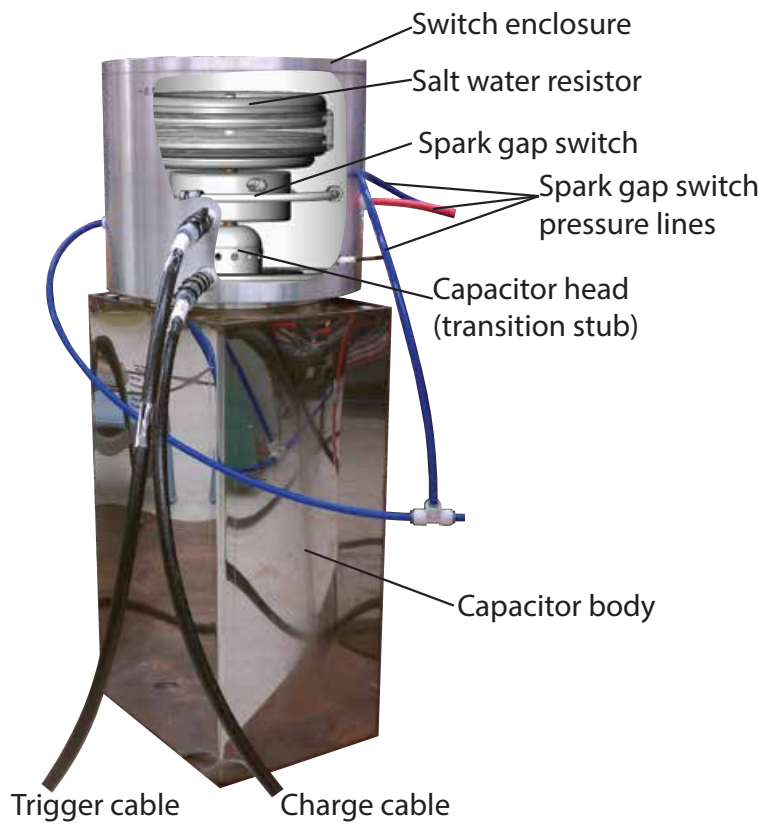


Figure 3.7: Capacitor and switch module, with cutaway of switch enclosure. Not shown: trigger resistor, shorting lever, and discharge cables.

provide access for switch fill and enclosure fill gases, and for charge and trigger cables. A pressure gauge monitors the interior pressure of the enclosure, and an inductive pickup probe (B-dot) attached to the side of the enclosure monitors the discharge's induced field. A spring-loading shorting bar bridges the capacitor terminals, and a manually inserted locking pin holds the bar in the retracted position when the capacitor is to be charged. Filling the enclosure with a mixture of sulfur hexafluoride and dry nitrogen insulates the components from arcing during charging.

Discharge cables

Each capacitor module connects to the rest of the system through a parallel bundle of six 3.0 m, high-power coaxial cables.⁵ Using six cables reduces overall cable inductance, and divides the high-current discharge among several conductors. The dielectric and inner conductor of the cables pass through modified Swagelok[®] Ultra-Torr fittings attached to the lid of the switch enclosure. The O-ring inside the fitting seals against the dielectric's surface, making the enclosure an airtight vessel. Inside the enclosure, each cable inserts into a receptacle bored into the top of the axial water resistor. The cable's outer conductor clamps to the metal body of an Ultra-Torr fitting, providing electrical contact for the return current.

Friction clamps bolted to the triplate transmission line, shown in Figure 3.8, secure the other ends of the cables to the transmission line perimeter. Each cable's inner conductor plugs directly into perimeter of the middle plate (anode) of the transmission line, where it is secured by a set screw. The friction clamp is an aluminum strip that

⁵Pulse cable #2121, Dielectric Sciences, Inc., Chelmsford, MA 01824-3526



Figure 3.8: Left: collet plates secure cables to triplate perimeter. Right: capacitor bank modules 6, 7, and 8. Background: charge dump tank with charge cables.

bridges the upper and lower plates (cathode) of the triplate line, and has a collet at its center to grip a metal sleeve attached to the cable's outer conductor. This friction clamp electrically links the outer conductor to both cathode plates and holds the cable from backing out of the anode plate. The anode plate's perimeter is inset 2.2 cm from the cathode plates, and does not contact the friction clamp. The next section will discuss the triplate line geometry in more detail.

Target chamber

The target chamber comprises three portions: a hollow, cylindrical frame, a conical triplate transmission line that directs the discharge current into the central load, and a cylindrical vessel to accommodate experiments carried out in vacuum. The frame's main functions are holding the triplate line together against the magnetic pressure experienced during shots and keeping the triplate aligned. Insulating rings between the frame and the triplate isolate the high-voltage triplate from the frame.

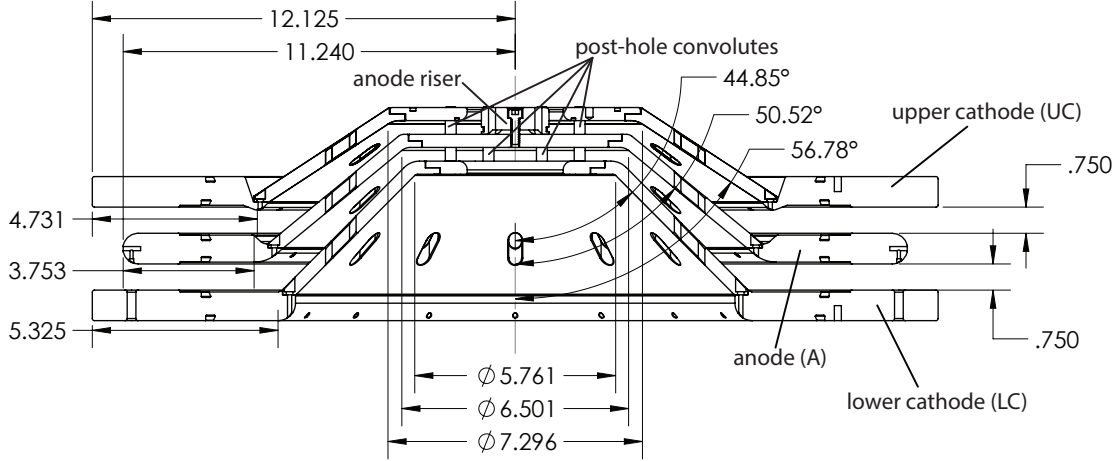


Figure 3.9: Section view of triplate transmission line. Dimensions provide values for inductance and impedance calculation. Bottom and top layers are the cathode, and the middle layer is the anode.

Each plate of the triplate line, with its dimensions pictured in Figure 3.9, is composed of three stainless steel parts: a flat annulus where the discharge cables connect, a conical transition segment, and a flat center section where the target is attached; these sections are abbreviated xR , xC , and xP , respectively, where x is UC (upper cathode), A (anode), or LC (lower cathode).

A conical line is desirable due to the structure's inherent mechanical strength and relatively low inductance, given by the expression

$$L = \frac{\mu_0}{2\pi \sin \theta} \int_{s_1}^{s_2} \ln \left(\frac{1 + d(s) \tan \theta / 2s}{1 - d(s) \tan \theta / 2s} \right) ds, \quad \theta < \pi/2, s_1 > 0. \quad (3.1)$$

where s is the radial coordinate in cylindrical geometry, $d(s)$ is the separation between conductors as a function of radial position, and θ is the angle of the conical line, oriented such that $\theta = 0$ is a flat radial line. A first-order Taylor approximation to

this solution yields the analytical expression

$$L = \frac{\mu_0}{2\pi \cos \theta} \frac{d\Delta s}{s}, \quad (3.2)$$

which reveals $L \propto 1/\cos \theta$; linear scaling with the length and separation ($L \propto d/s$) mimics that of a parallel plate transmission line [55].

This conical transmission line structure is common to several high-current pulsed power devices, including the Z Machine and Saturn, both at SNL, or COBRA at Cornell University. In the case of MG2, the UCP and LCP are the cathode, and are connected via post hole convolutes passing through the AP in the center section. The UCP has a ID 7.0 cm bore to accommodate a OD 4.9 cm solid cylinder rising from the flat AP below which raises the anode surface to the level of the UCP, as shown in Figure 3.5. The load bridges the A-K gap between these two surfaces, completing the circuit at the triplate’s apex. The conical segments of the triplate have radial slits every 45° which enable evacuation of the triplate gap in the original design discussed in Section 3.1.1.

Two dielectric rings, angled to discourage dielectric tracking according to the principle illustrated in Figure 3.10, separate the UCR and AR, and the LCR and AR; additionally, they provide structure to the chamber frame by forming part of the wall, as seen in Figure 3.4. These rings seal against the triplate with O-rings, which are left over from the original SNL design. Such rings, often referred to as vacuum insulators in the literature, are typical in conical transmission lines, and are sometimes stacked to improve high-voltage performance [54]. A similar, smaller ring separates the UCP and AP, and also functions as an air-vacuum interface. The larger rings on the triplate

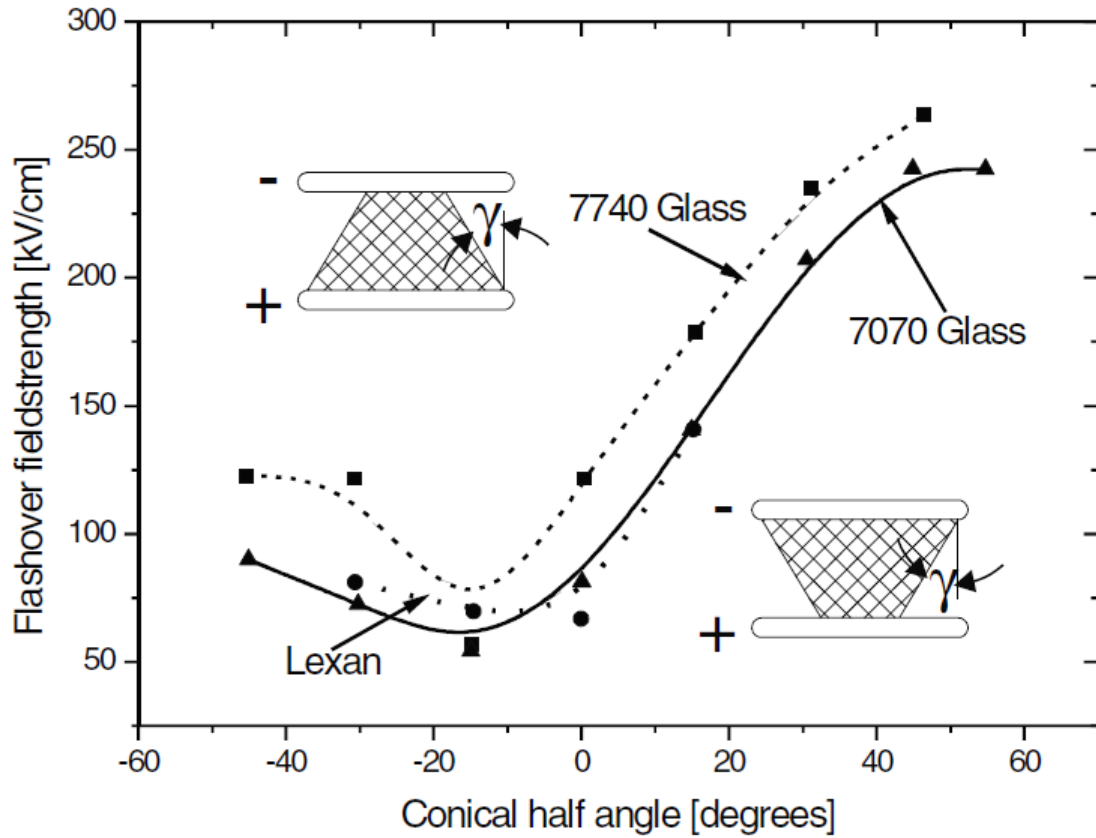


Figure 3.10: Angled vacuum insulators help avoid breakdown (flashover) across the anode-cathode gap. This influences the design of transmission line transition sections, e.g. between atmosphere and vacuum. Conical half angle (γ) is conventionally negative when the dielectric is wider on the anode side (the left image in the figure) [4].

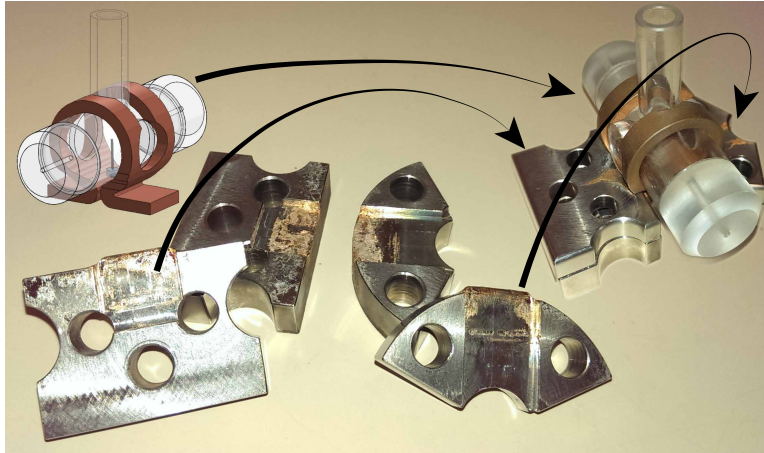


Figure 3.11: A coil assembly fits inside a split clamp. Several screws that pass through the clamp halves tighten the clamp and secure the coil by engaging threads on the UCP.

perimeter inspired the design of this smaller central ring, although the O-ring seals were adjusted to mate with the UCP and AP.

The top of the triplate is adaptable to a variety of loads, but the single-turn coil is MG2's most common load. To adapt this load to the transmission line, and to simplify coil replacement, a shaped clamp like the one shown in Figure 3.11 bolts into the anode and cathode surfaces. This coil clamp is composed of two pairs of stainless steel blocks, each with a slot that matches the coil base. One pair of blocks bolts into the anode, and the other into the cathode, and these secure the coil base as the bolts are tightened. Coil replacement involves removing the bolts, extracting the used coil, positioning a new coil in the clamp, and re-tightening the bolts. The coil clamp parts eventually degrade from contact arcing, but the simple geometry of the clamps makes replacement economical.

A small cylindrical (ID 22 cm \times 9.2 cm) vacuum vessel, also pictured in Figure 3.5, bolts to the flat top of the triplate line, and a claw clamp fixture seals the flanged bottom of the vessel's wall against an O-ring on the UCP. The UCP, AP, and the small dielectric ring between them function as the base of the vacuum vessel. The wall of the vessel is stainless steel, with two ports along the coil/laser axis 3.0 cm off the centerline, two ports along the coil's perpendicular, and several auxiliary ports for gas or electrical feedthroughs. A stainless steel lid bolts to the top of the vessel and seals against an O-ring at the flanged top of the vessel wall, sealing the chamber.

Charge & trigger distribution

A high-voltage DC source⁶ provides the charge current to the capacitor bank, and the capacitors are connected to the current source through a dump resistor chain. In the event that the capacitors must discharge without sending their energy into the load, the capacitors can dissipate their energy into the high-power 16.2 k Ω ceramic resistors in the resistor chain. Charge is dumped by closing a Ross relay⁷ that shorts the capacitors to ground, and the high value of the dump resistors makes the capacitors discharge slowly and safely in ~ 100 ms. During charging, the dump relay (normally-closed) is held open by a 120 VAC current to the relay's coil; this current is switched by the MG2 control system. This entire circuit, except for the bank capacitors, is suspended in a metal tank filled with transformer oil. The circuit schematic for the charge dump tank is shown in Figure 3.12.

⁶Glassman PK125, Glassman High Voltage, Inc., 124 West Main Street, High Bridge, NJ 08829-0317.

⁷Ross Engineering Corporation, 540 Westchester Drive Campbell, CA 95008

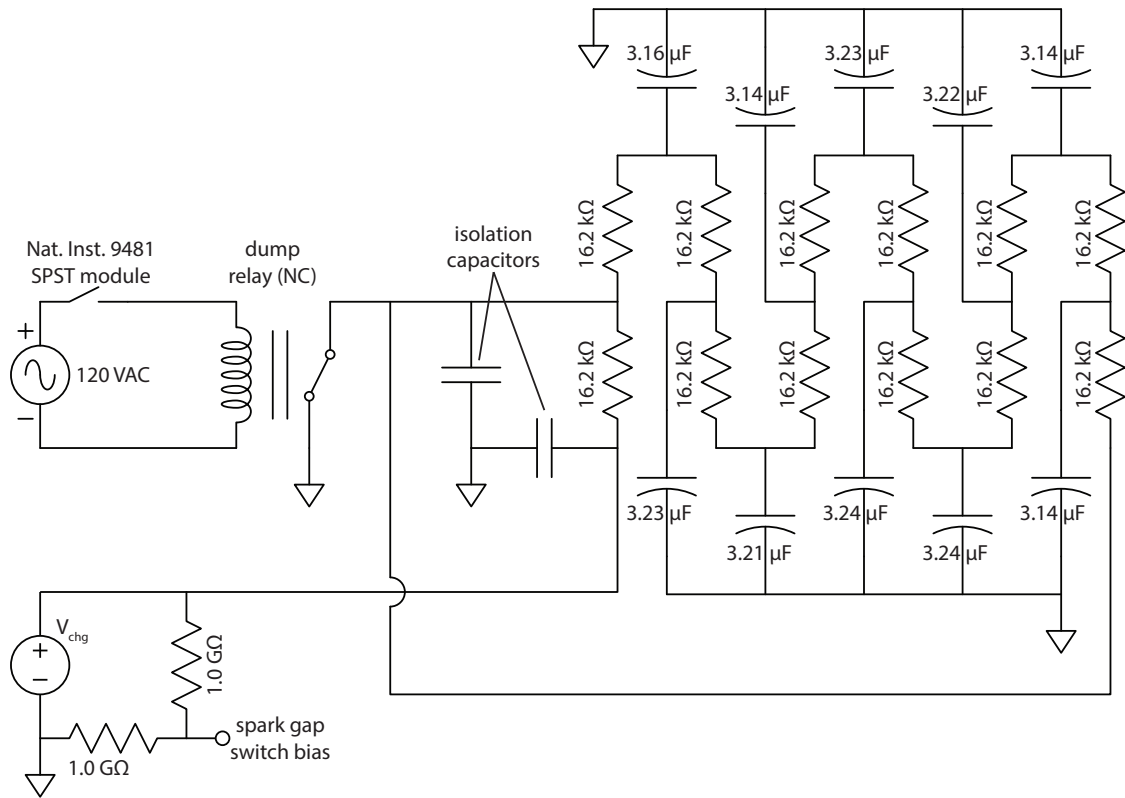


Figure 3.12: Schematic of charge dump tank. A 120 VAC control signal energizes dump relay coil. A high-voltage DC source charges capacitors through $16.2\text{ k}\Omega$ dump resistors. Disabling the 120 VAC signal closes the dump relay, forcing the capacitor bank to discharge through the dump resistor chain.

A master trigger controls discharge timing, which is nearly synchronous, except for up to 30 ns delay due to various trigger cable lengths: the trigger cables have propagation times ranging between 15 and 45 ns. The schematic for this trigger circuit is shown in Figure 3.13. The inherent trigger cable delays are small compared to the ideal current rise time of 1.63 μ s. A high voltage pulse generator⁸ triggers a single spark gap switch; this sends a falling-edge voltage pulse to the spark gap switches on the capacitors. When the falling pulse reaches a capacitor switch, the open circuit at the switch trigger terminal produces a reflected pulse of sufficient amplitude to initiate the spark gap breakdown. The breakdown is sustained while the capacitor discharges its energy. Operation of the master trigger switch is based on the Paschen breakdown principle, and uses the same gas fill pressure as the capacitor bank switches. The master trigger switch operates at half the voltage of the capacitor bank, and to compensate for this half voltage, the electrode gap in the master switch is half that of the capacitor bank switches. This halves the Paschen breakdown voltage by halving the pd product in Equation (2.5).

Control electronics

An electronics cabinet rack contains the control interface that operates MG2 during a shot. The notable contents of this rack include the high-voltage charging source, the trigger pulse generator, a National Instruments CompactRIO (cRIO) chassis⁹, and electronic pressure regulators and transducers. The cRIO chassis contains expansion contains both analog and digital signal terminals, and digitally operated

⁸Maxwell 40168 trigger amplifier, General Atomics/Maxwell Laboratories

⁹National Instruments Corporation, 11500 N Mopac Expwy, Austin, TX 78759-3504

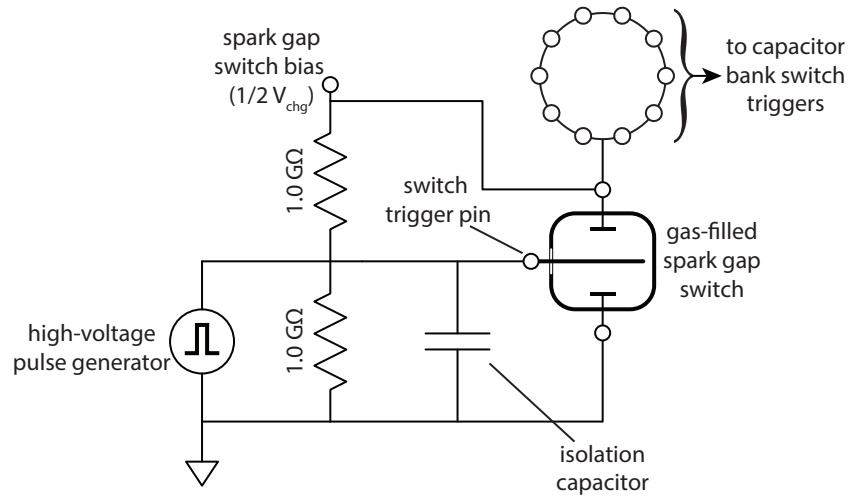


Figure 3.13: Schematic of master trigger tank. A high-voltage pulse triggers the master switch, which shorts to ground and sends a falling-edge pulse ($1/2 V_{\text{chg}} \rightarrow \text{GND}$) to capacitor bank switches. Arrival of this pulse triggers the capacitor bank.

relays. This electronics hub provides the user interface via a remote computer which accesses the cRIO via its local network. National Instruments LabVIEW software operates the cRIO and translates user commands into signals that are sent to the cRIO expansion modules, and these signals operate MG2. This remote operation of the system simplifies operation, and enhances safety.

Pressure control of the spark gap switches' fill gas is managed with an electronic regulator¹⁰ with a closed feedback loop that maintains the pressure setpoint. Electronic solenoid valves manage the switch fill gas supply and exhaust lines. Digital and analog signals from the cRIO manage the Glassman and Maxwell high-voltage sources; their outputs connect to the charge and trigger distribution circuits, respectively. Feedback

¹⁰QB1 electronic regulator, Proportion-Air, Inc., 8250 N. 600 West McCordsville, Indiana 46055

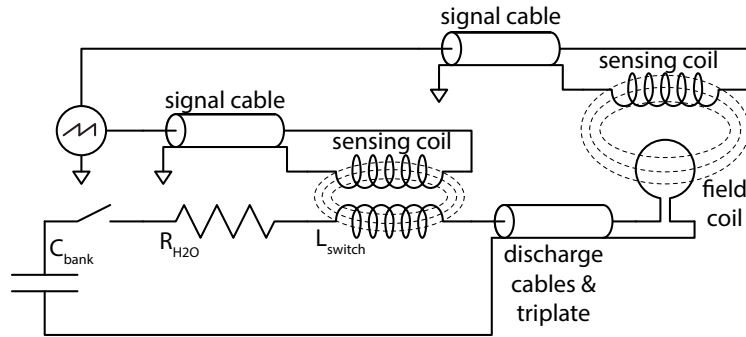


Figure 3.14: Schematic diagram of sensing coils that monitor discharge current.

signals to the cRIO allow the user to monitor important signals, such as capacitor bank voltage, via the LabVIEW graphical interface.

Diagnostics

Inductive pickup coils (B-dots) remotely sense the discharge current, and are the most important diagnostic tools on the MG2 system. Their presence in the system is shown schematically in Figure 3.14. A basic B-dot is a simple wire loop which detects the electric field induced by a changing magnetic field according to Faraday's Law [Eq. (2.8)]. In the simple case of a magnetic field parallel to the axis of a single-turn wire loop, the induced open-circuit voltage is $E_{\theta}\ell$, where E_{θ} is the azimuthal electric field with respect to the magnetic field axis, and ℓ is the loop's circumference. A plastic-encased B-dot bolted to each switch enclosure samples the field generated by the capacitor discharge through the center of the enclosure. This current passing through the center of the switch enclosure induces a voltage in the B-dot, which is recorded by a digitizing oscilloscope.

To calibrate the B-dot voltage with capacitor current, each capacitor is fired

individually into a high-energy, low-value (1.4 kJ, 4.987m Ω) current viewing resistor (CVR). Using Ohm's law with the CVR voltage gives the current from the capacitor ($I_{pk} = V_{pk}/4.987m\Omega$), which can be compared with the time-integrated B-dot signal to generate a scale factor relating the capacitor's current with the B-dot output. This method includes the effects of attenuators on the B-dot circuit, B-dot orientation, and frequency response of the detecting circuit, although a change to the B-dot circuit or the MG2 resonant frequency may necessitate recalibration.

An array of three, four-channel, 500 MHz digitizing oscilloscopes¹¹ record the signals from each capacitor's B-dot, and from an additional, uncalibrated B-dot sampling the magnetic field at the load. The LabVIEW control program includes a function that downloads the digitized signals for later processing. Numerical integration of this data yields the discharge current from each capacitor, the sum of which indicates the total current $\Sigma I(t)$ into the transmission line. The B-dot near the load can be scaled to follow the initial slope of the total discharge, and can indicate if the load reached peak current. If the B-dot signal at the load deviates from $\Sigma I(t)$, this usually indicates the current bypassed the load before peaking, most likely due to arcing.

3.2.5 Circuit analysis

When considering MG2's discharge behavior, all circuit elements should be considered reactive, having some frequency-dependent impedance $Z(\omega)$ that results from some inherent resistance, inductance, and capacitance. However, most elements

¹¹Tektronix TDS 3054B

have one term that dominates the impedance magnitude. For example, at MG2's operating frequency (~ 140 kHz), the inductance of the discharge cables is responsible for most of the cables' impedance. This approximation allows the MG2 system to be simplified to an ideal circuit schematic, which can be further simplified to a single resistor, inductor, and capacitor. This simplified form is the basic series RLC circuit, which can be modeled mathematically as a damped harmonic oscillator. This treatment enables estimation of circuit behavior, and is strikingly accurate if the discharge proceeds as designed.

Although an RLC model provides a useful first-order estimate, it does not account for transmission line characteristic impedances. Mismatching these impedances can result in power reflection, which can affect circuit performance and component lifetimes. Numerical modeling software is often the best approach to calculate impedance matching effects. Modeling software can also account for signal propagation velocities, which can predict effects brought about by varying transmission line lengths or asynchronous capacitor discharges. A tractable, yet versatile software package used at SNL's pulsed power division is BERTHA transmission line simulation software [29], popularized by the Naval Research Laboratory (NRL). Modeling MG2 with this software provides deeper understanding of the discharge behavior, such as ringing voltage and propagation delay effects.

RLC model

The RLC model is useful for quickly estimating the circuit behavior, and is easy to adjust when needed. Inversely, this model can give an estimate of the circuit

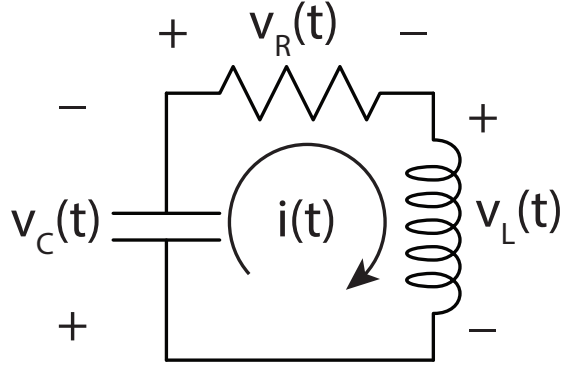


Figure 3.15: This series combination of a resistor, inductor, and capacitor (series RLC) is the simplest form of the circuit schematic for the MG2 system. Solving this circuit for $i(t)$ given the initial condition $v_c(t = 0) = V_{chg}$ will yield an ideal model of the system's behavior.

parameters from the measured discharge curve. Current behavior in the unforced series RLC circuit, shown in Figure 3.15, is described by Kirchhoff's voltage law, given in the form of the integro-differential equation

$$\frac{1}{C} \int i(t) dt + i(t)R + L \frac{di(t)}{dt} = 0, \quad i(t = 0) = 0, \quad (3.3)$$

in which we impose the boundary condition of no initial current. Differentiating with respect to time, the homogeneous second order differential equation

$$\frac{d^2i(t)}{dt^2} + \frac{R}{L} \frac{di(t)}{dt} + \frac{1}{LC} = 0 \quad (3.4)$$

appears. Transforming to the frequency domain by using time-harmonic behavior, where d/dt transforms to complex frequency s , this becomes a second order polynomial in complex frequency s

$$s^2 + \frac{R}{L}s + \frac{1}{LC} = 0, \quad (3.5)$$

for which the roots are

$$s_{1,2} = -\alpha \pm \sqrt{\alpha^2 - \omega_0^2}, \quad \alpha = \frac{R}{2L}, \quad \omega_0 = \frac{1}{\sqrt{LC}}. \quad (3.6)$$

The roots will be complex if $\alpha < \omega_0$, and we will assume this to be the case, although this cannot be known until values are given for R , L , and C . This assumption makes the roots

$$s_{1,2} = -\alpha \pm i\omega_d, \quad (3.7)$$

where $\omega_d = \sqrt{\omega_0^2 - \alpha^2}$. The general solution to Equation (3.4) is

$$i(t) = A_1 e^{s_1 t} + A_2 e^{s_2 t}, \quad (3.8)$$

with boundary conditions determining the values of constants A_1 and A_2 . With s being complex, a damping term and an oscillating term appear, giving the applied solution of

$$i(t) = (A_1 + A_2)e^{-\alpha t} \cos(\omega_d t) + i(A_2 - A_1)e^{-\alpha t} \sin(\omega_d t). \quad (3.9)$$

Ignoring the trivial solution $A_1 = A_2 = 0$, recall the boundary condition of zero initial current. This reveals $A_1 = -A_2$, since

$$0 = (A_1 + A_2) \cos(0) + i(A_2 - A_1) \sin(0) = i(A_1 + A_2). \quad (3.10)$$

Letting $I_0 = i(A_2 - A_1)$, we obtain the condensed expression for current

$$i(t) = I_0 e^{-\alpha t} \sin(\omega_d t), \quad (3.11)$$

where I_0 is interpreted as the current expected if the discharge peaks at $t = 0$, which would occur given vanishing inductance. This I_0 coefficient is the current through

cap bank	R (mΩ)	L(nH)	C (μF)
one capacitor	100	264.7	3.20
ten capacitors	10	40	32.0

Table 3.3: Lumped circuit values for RLC model, derived from individual MG2 component values. Values are estimates.

the impedance presented by the circuit's inductance and resistance, driven by the capacitor charge voltage V_{chg}

$$I_0 = \frac{iV_{chg}}{i\omega_d L + R}. \quad (3.12)$$

The solution indicates I_0 value is a complex number, which is a consequence of the leading of current with respect to voltage in an capacitive element. This is expected after considering the Fourier transform of the relation between current and voltage of a capacitor:

$$i(t) = C \frac{dv(t)}{dt} \xrightarrow{\mathcal{F}} I(\omega) = i\omega CV(\omega). \quad (3.13)$$

Note that the capacitive contribution is not included in I_0 since the capacitive term in Equation (3.3) equals V_{chg} at $t = 0$, which is the time at which I_0 is defined; however, the capacitors' inductance is still included.

Grouping the inductances, capacitances, and resistances from the MG2 circuit schematic in Figure 3.16 gives the values for the RLC model listed in Table 3.3. Inputting these values into Equations (3.11) and (3.12) and taking the absolute value, we arrive at the simple numerical model for the magnitude of the current in the ten-capacitor system:

$$i(t) = 27.472 \cdot V_{chg} e^{-1.25 \times 10^5 \cdot t} \sin(8.75 \times 10^5 \cdot t). \quad (3.14)$$

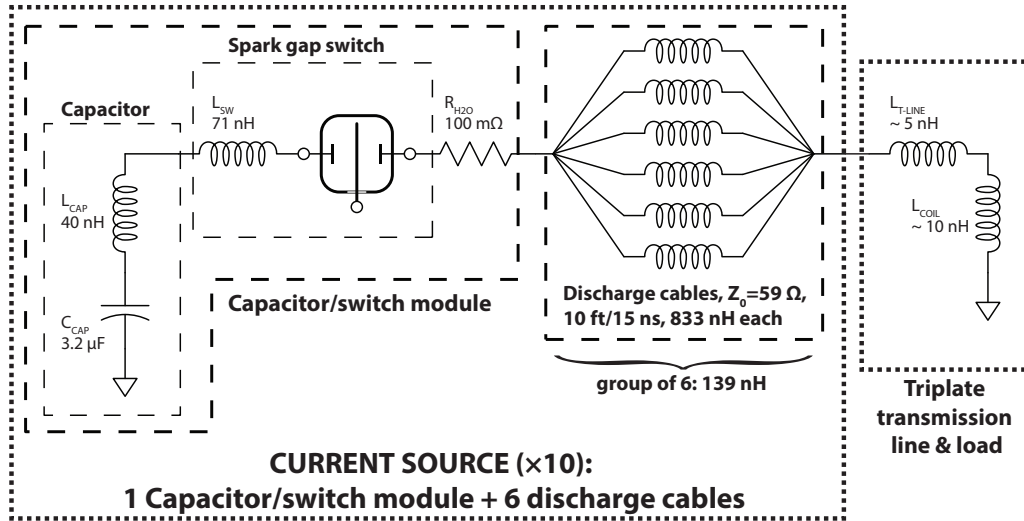


Figure 3.16: This schematic is an electrical representation of the most important circuit elements (resistors, inductors, and capacitors) in the MG2 system. The elements can be combined to produce the simple model in Figure 3.15.

Figure 3.17 plots the discharge versus time, with current normalized to I_0 .

Comparing this ideal model with measured discharge traces can reveal non-ideal behavior, such as the inductance change resulting from an arc during the discharge. It is also a method of determining the inductance change between different loads, since the load contributes little to the total capacitance and resistance. Resolving I_0 , ω_d , and α from a discharge trace is straightforward, and the values for the lumped circuit elements can be solved from those.

BERTHA simulation

Limitations of the RLC model are clear if transmission line behavior is important in the circuit model. Power delivery to the load is dependent upon the reflection

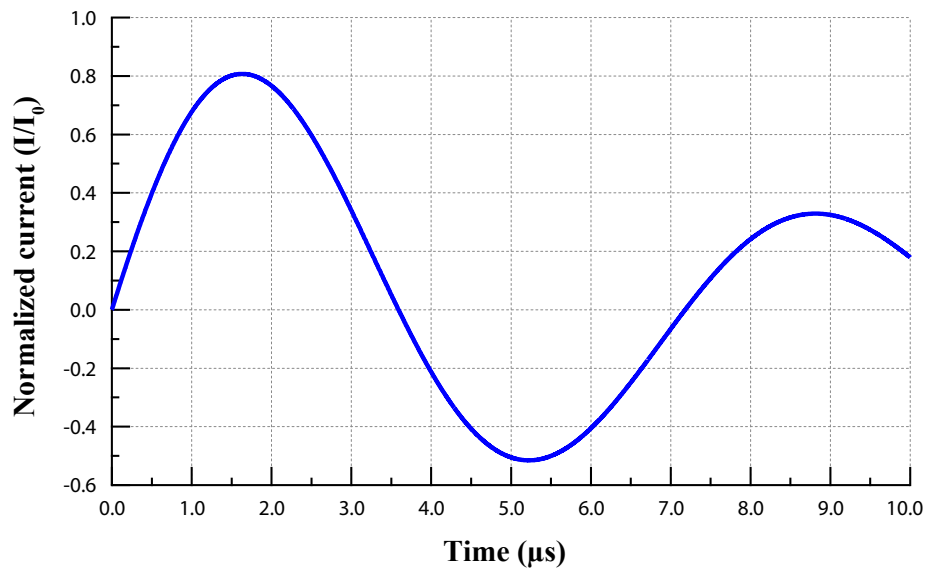


Figure 3.17: Normalized plot of discharge current for the ten-capacitor system Equation (3.14). Maximum current of $0.81I_0$ occurs at $1.63\ \mu\text{s}$; reverse current peaks at $-0.52I_0$.

behavior at component transitions, such as between the discharge cables and triplate line. Also, the RLC model assumes instantaneous power transport; in reality, the current pulse travels through the system with some propagation time, and if some circuit elements are not synchronized with others, this can degrade performance. Consideration of these additional effects requires treatment of the MG2 circuit as a network of transmission lines, which lends itself to numerically solving the circuit with specialized software. Stella computer software is a development environment used in the pulsed power departments at the NRL and SNL. BERTHA [29] is a plugin to the Stella environment, and provides a circuit schematic graphical interface that solves the circuit drawn by the user; Stella's plotting functions visualize the results.

Figure 3.18 compares the simple RLC model with more realistic transmission line models of a BERTHA RLC with nearly zero-length connections, and a BERTHA model with explicit circuit elements and realistic transmission lengths, respectively shown in Figures 3.19 and 3.20. Compare these BERTHA schematics with Figures 3.15 and 3.16, respectively. All models are subject to the initial condition of $V_{chg} = 50$ kV.

Two distinctions are obvious: the amplitudes of the BERTHA models are slightly greater than that of the simple RLC, and the response of the model with the realistic cable lengths appears jagged. When magnified, this jagged appearance is found to be an oscillation with a period of approximately 83 ns. Notice that this effect does not appear significant in the BERTHA-run basic RLC where cables are ignored, and is by definition not a feature of the ideal RLC.

Extending the BERTHA model to a ten-capacitor layout, switch timing, and triplate line characteristics produces an even more detailed model. This model was

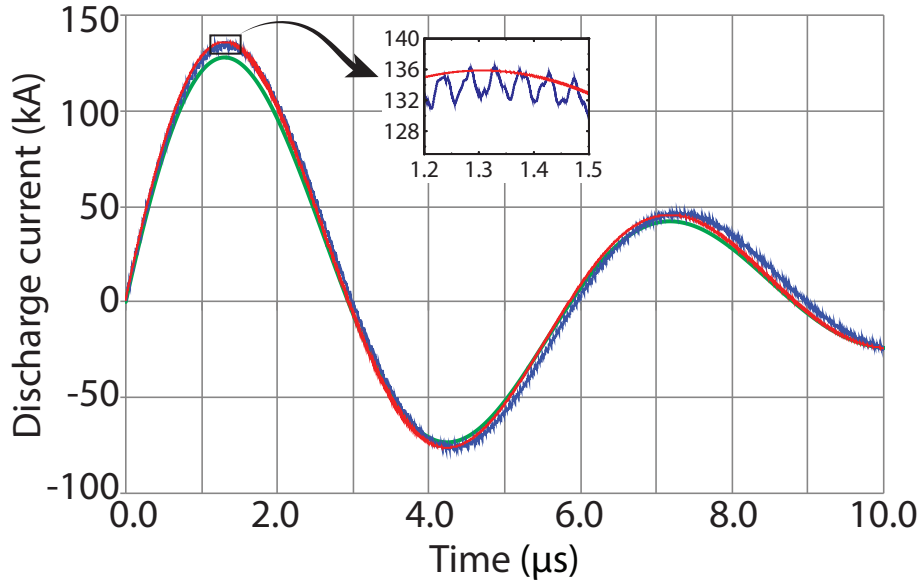


Figure 3.18: Comparison of discharge models using a single capacitor module. Green trace (not shown in inset): analytic RLC model prediction. Red trace (inset, smooth profile): numerical BERTHA simulation with a simple RLC arrangement as in Figure 3.19. Blue (inset, oscillating profile): numerical BERTHA simulation with component-specific simulation elements (Figure 3.20).

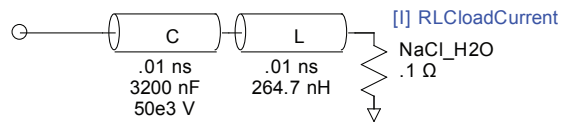


Figure 3.19: BERTHA schematic of a simple RLC model, using values from Table 3.3 for a single switch. Compare with Figure 3.15.

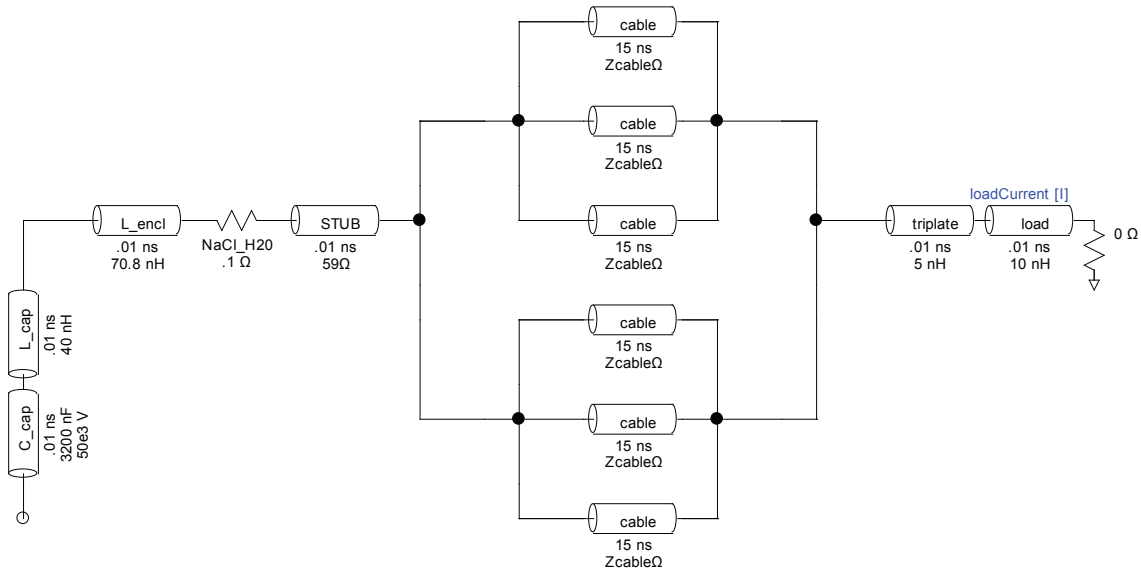


Figure 3.20: BERTHA schematic representing MG2 using one capacitor, with distinct circuit elements. Compare with Figure 3.16.

initially developed by Dr. Kenneth Struve of SNL, who commissioned the original MegaGauss project in collaboration with UT-Austin [57]. An individual capacitor and switch enclosure module is represented by a single element named Cap & Switch in Figure 3.21, and is an abstracted element that refers to another BERTHA schematic. The triplate line is also divided into segments to allow BERTHA to compute the impedance effects at the junctions. This model can be adjusted to observe changes brought about by mistimed capacitor discharges, for example. Figure 3.22 displays the effect of an asynchronous discharge, for which the peak current drops and occurs later than it does in the perfectly timed case. The ideal RLC curve is overlaid for comparison with the BERTHA simulation, with $V_{chg} = 50 \text{ kV}$ for all models.

The ideal RLC model provides a close estimate of the circuit behavior which is

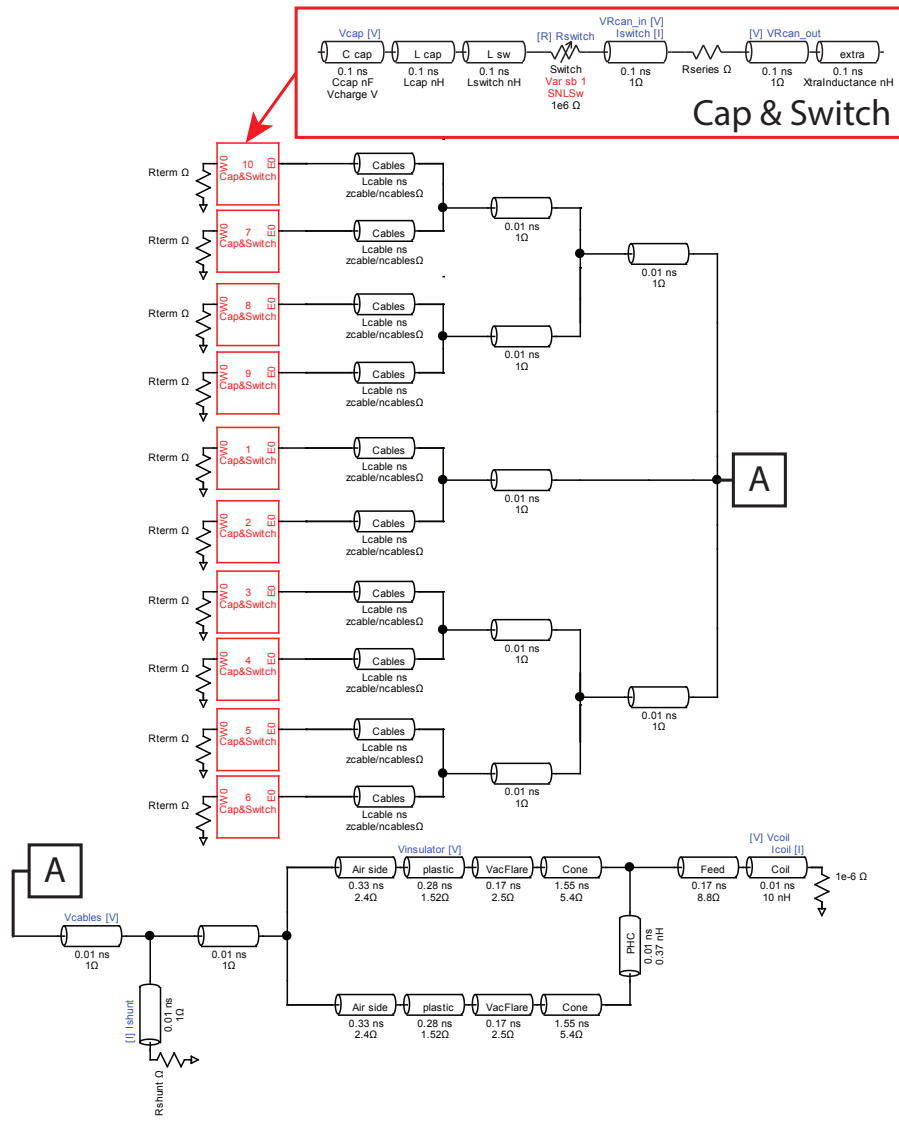


Figure 3.21: BERTHA schematic of entire ten-capacitor system. Top: capacitor bank; bottom: triplate transmission line and coil load. Schematic is split at node “A” to better fit the schematic into a single figure.

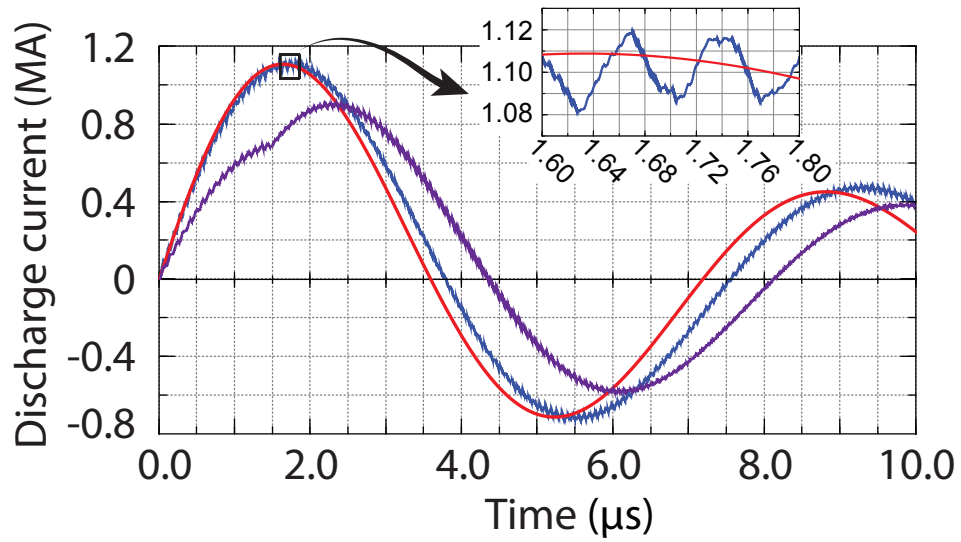


Figure 3.22: Illustration of the resulting total discharge current when four switches in the BERTHA schematic of Figure 3.21 are delayed by $1.5 \mu\text{s}$. Total current has a dimple caused by the asynchronous switches peaking late. A proper discharge, and an ideal RLC model are shown for comparison; notice the high-frequency ringing in the BERTHA simulation plots.

acceptable for predicting the approximate discharge. However, the truer representation of the system is found in the BERTHA model, which considers reflections and propagation delays when solving the circuit.

3.3 Performance

Experimental verification of MG2's design showed viability in both atmospheric and vacuum conditions, although high current vacuum shots showed a great tendency to arc prematurely before the vacuum chamber modification. Vacuum operation at high current was more successful if the cluster gas jet was not included in the shot. Atmospheric operation was highly successful; the presence of atmospheric pressure in the triplate seemed to suppress the arcing modes responsible for vacuum failure.

With most shots, the primary diagnostic for determining the success of a shot was the collective signals of the capacitor B-dots. An additional B-dot near the load picked up the field from the current in the load, and facilitated comparison with the sum of the switch currents $\Sigma I(t)$. Ampere's law

$$\nabla \times \mathbf{B} = \mu_0 \mathbf{J} + \mu_0 \epsilon_0 \partial \mathbf{E} / \partial t \quad (3.15)$$

implies we can expect a linear relation between the detected field at the load B-dot and the load current $I_L(t)$, and assuming lossless operation such that $\Sigma I(t) = I_L(t)$, the signal at the load B-dot should follow $\Sigma I(t)$, with some proportionality constant. This constant can be estimated by accepting the $\Sigma I(t) = I_L(t)$ condition, and using the calibrated capacitor B-dots to calibrate the load B-dot. In practice, however, this is not the best approach.

In between shots, the load B-dot moves, which invalidates its calibration. Instead of recalibrating before every shot, the post-shot load B-dot signal is scaled to match the initial few hundred nanoseconds of $\Sigma I(t)$. During this initial time, experience shows breakdown is highly unlikely, even in breakdown-prone conditions. This scaling method is usually sufficient to reach a very close estimate of the proper scaling coefficient, and a few iterations brings the load B-dot signal to a scale that allows clear comparison with $\Sigma I(t)$. In the rare condition that this is inconclusive, the inductance of the discharge may be calculated; a reduced effective inductance usually indicates the current took a less inductive path by bypassing the load through an arc. Figures 3.23 and 3.24 show discharges indicative of an inductance change.

Discharge attributes

Over seven hundred MG2 shots have uncovered some general rules that summarize system behavior. These rules are useful for estimating peak current and resonant frequency, and offer some predictive insight into the likelihood of experiment success. The rule of thumb for peak current I_{pk} is

$$I_{pk}[\text{kA}] \approx 2N \cdot V_{chg}[\text{kV}], \quad (3.16)$$

where N is the number of capacitors used in the system, and V_{chg} is the charge voltage of those capacitors.

In the ideal RLC model, under the approximation that the damping coefficient α is much less than the undamped resonant frequency ω_0 , then $\omega_d \approx \omega_0 = (LC)^{-1/2}$, which is inversely proportional to the square root of the total inductance. A change in resonant frequency, best indicated by a change in the time to peak (τ_{pk}), is indicative

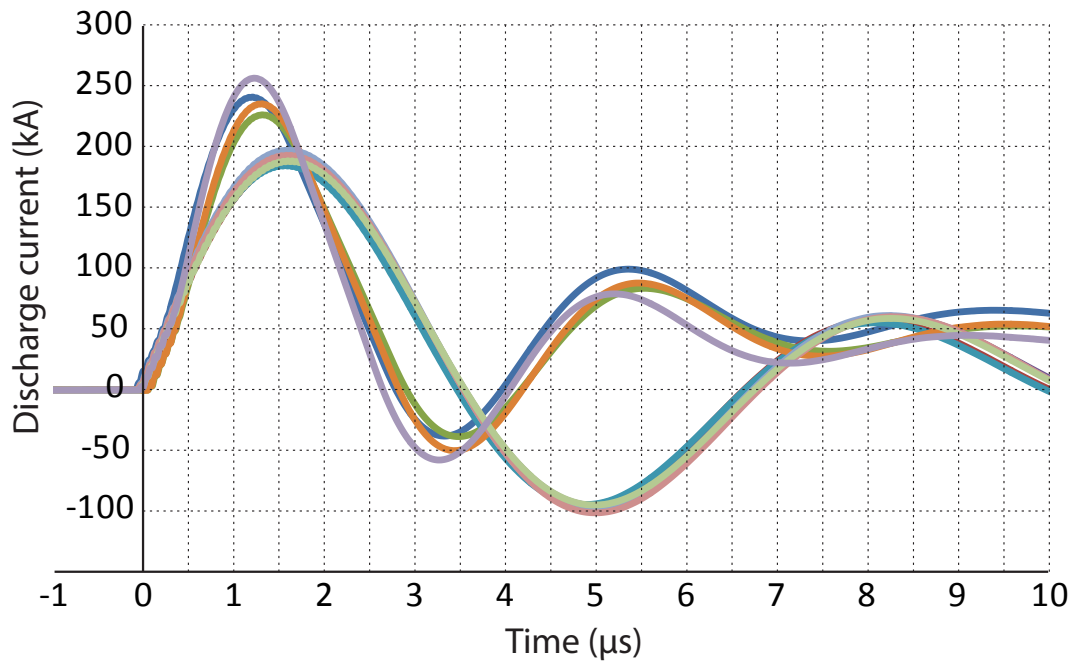


Figure 3.23: In Shot 450, several switch/capacitor assemblies arced inside the switch enclosure. This bypassed the discharge cables and subsequent circuit elements, reduced the inductance of that sub-circuit, and resulted in a faster discharge.

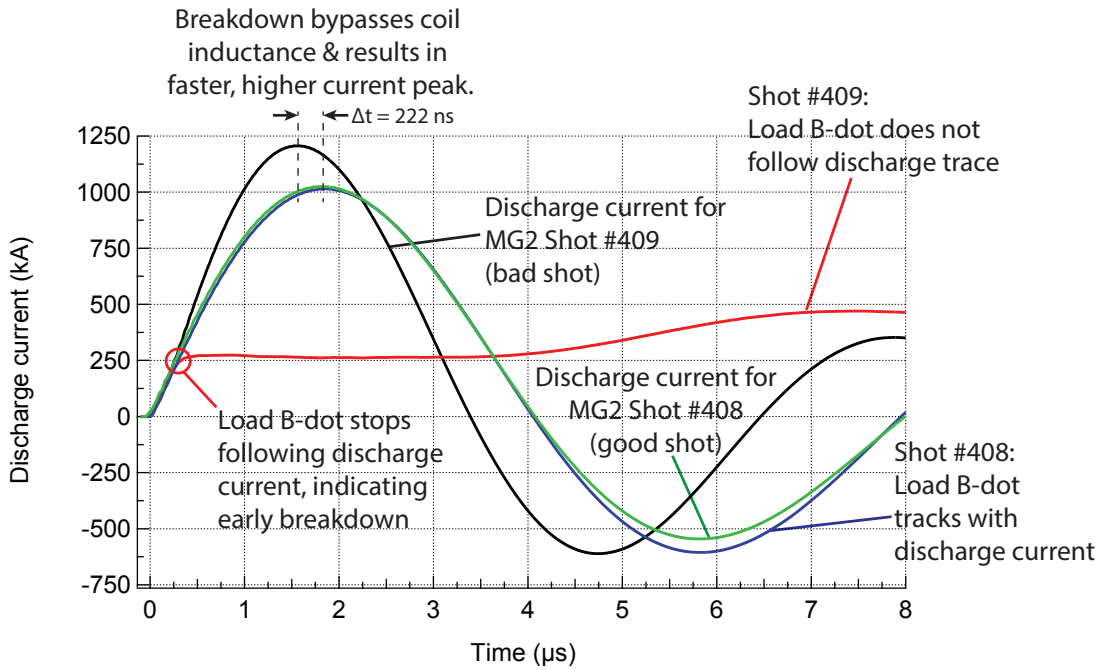


Figure 3.24: Comparing the load B-dot signal with the sum of the capacitor currents can reveal if there was a fault in field production before the peak field occurred. A sudden deviation from expected behavior almost always indicates an arc (e.g. Shot #409).

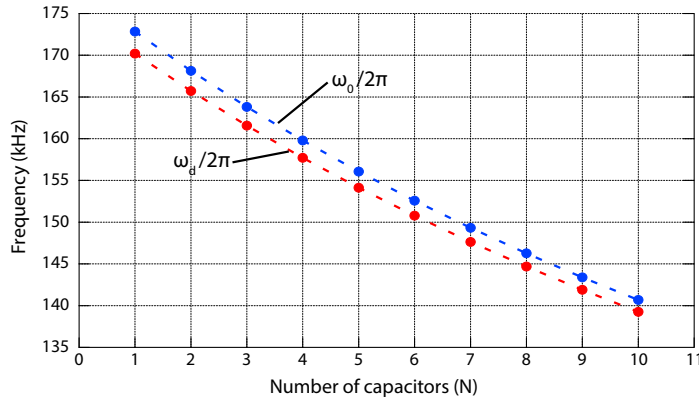


Figure 3.25: Resonant frequency and time to peak for the MG2 system is dependent on the number of capacitors involved in the discharge. As the number of capacitors (N) decreases, the overall system inductance falls, making the discharge faster.

of an inductance change, usually by an arc in a switch enclosure or in the vacuum chamber. Changing the size of the capacitor bank increases the inductance and decreases the capacitance of the capacitor bank by a factor of N , the number of capacitor modules in use. This keeps the resonant frequency of the system quite steady for any capacitor bank size, since most of the inductance and practically all of the capacitance in the expression for ω_0 is controlled by N . The slight dependence on N illustrated in Figure 3.25 is a result of the inductance of the transmission line triplate and the load, which are not dependent on N .

Experiment summary

MG2 performance after initial assembly at The University of Texas at Austin (UT-Austin) had mixed success when operating at vacuum, but this was before the vacuum vessel modification. Cluster gas jet operation appeared responsible for this poor vacuum behavior, since many of these shots were of low enough current that

vacuum operation should be successful. A flow line that directed the cluster gas away from the transmission line improved vacuum performance, and enabled an exploratory magnetized cluster plasma experiment on the Glass Hybrid OPCPA Scale Test (GHOST) [19] laser at UT-Austin in collaboration with Matthew McCormick (UT-Austin). During that experiment, most shots were in vacuum, yet the gas jet did not interfere with the pulsed power discharge, and most vacuum shots reached peak field. Most of these shots only used a small portion of the capacitor bank—usually Switches¹² 5 and 10.

The next shots (Faraday rotation) directly measured the field strength, and initially met with trouble in vacuum. These shots used all ten capacitors, although this configuration made breakdown in vacuum more likely. To avoid breakdown complications, we operated the system at atmospheric pressure during Faraday measurements. The resulting Faraday rotation measurements of the on-axis field profile supported the estimated field values, which were based on approximate coil geometry and the assumption that all drive current passed through the coil. These Faraday rotation shots were a joint effort with Sean Lewis (UT-Austin).

The upgraded vacuum vessel (designated VB) was installed following the Faraday shots, but this change did not improve vacuum performance improvement initially. Troubleshooting revealed breakdown was still occurring across the A-K gap between the AP and UCP, and installation of a ring-shaped insulator at this position arrested these breakdowns. Strategically placed strips of Mylar[®] insulation blocked a

¹²In this work, the word *switches* with a number following is common parlance when referring to an entire capacitor module.

handful of other arcing-vulnerable points, and successful high-field shots in vacuum followed. An 80 kV shot (typical operation uses $V_{chg} = 50$ kV) with all 10 capacitors caused a catastrophic breakdown across the atmosphere-insulated gap outside the VB chamber, damaging several plastic insulators. This suggested the triplate line may not be able to hold off the inductive voltage from such a high-current shot, and discouraged operation at peak currents above 1.1 MA (50 kV charge) until the triplate could be upgraded or further studied to determine the breakdown causes.

Addition of the cluster gas jet to the VB chamber brought back premature arcing, and this problem was not resolved in time for the scheduled TPW experiment. The operation of the gas jet was not the only issue—the presence of the metal-bodied gas valve encouraged arcing in the smaller space of the VB vessel, although this conclusion may be premature with the limited data available. MG2 was reassigned to a planned magnetized blast wave experiment, which proved successful in vacuum using an enlarged coil containing a gas cell assembly. This experiment is discussed at length in Chapter 4.

High-field coil destruction

Driving a high current through the high-field coils usually destroyed the coils. The coil's form factor controlled the dominant failure mode. For relatively low-mass coils with holes or slots cut into the coil's wall, more fragmentation occurred, most likely due to the structural weakness seeded by those features. On the other hand, solid loop coils fragmented into only a few pieces, and showed much more necking. On a few rare occurrences, an arc shorted the coil after it had begun to expand, leaving

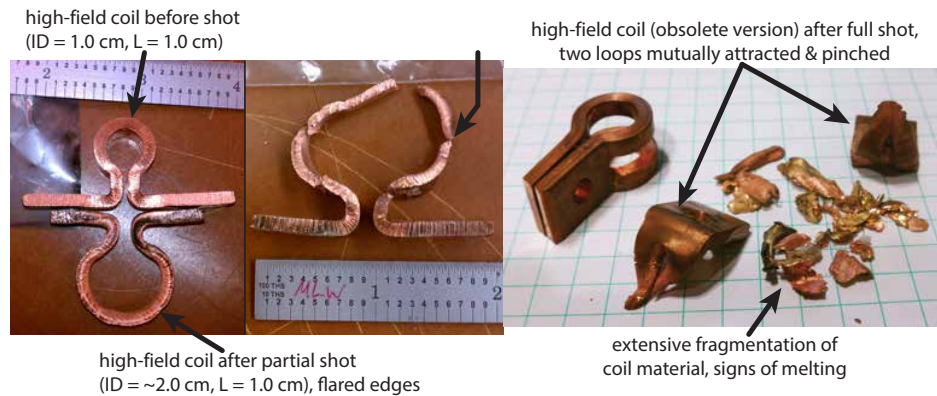


Figure 3.26: From left to right, coil failure modes range from dramatic expansion, necking to the point of coil separation, or complete fragmentation. These affects are driven by the magnetic pressure within the coil, although melting may play a role in generating the small pieces of debris as in the rightmost image.

an intact coil with an increased diameter. This gave a fascinating glimpse into the appearance of a coil just before failure. Figure 3.26 illustrates some high-field coils that exhibited these failure modes.

Synchronization of currents

Ideal discharge behavior assumes perfect superposition of the individual capacitor discharges, which all are assumed to be equivalent. Realistically, there is some jitter in the timing of the individual discharges, which are not equivalent, although they are similar enough to neglect the differences in this discussion. There is some fixed jitter in the system due to trigger cables of different lengths, but this yields a jitter of about 20 ns, which is insignificant in a discharge with $\tau_{pk} = 1.63 \mu\text{s}$. A significant effect appears when the jitter approaches τ_{pk} ; the BERTHA simulation in Figure 3.22 simulates the staggered discharge that results. This effect presented itself

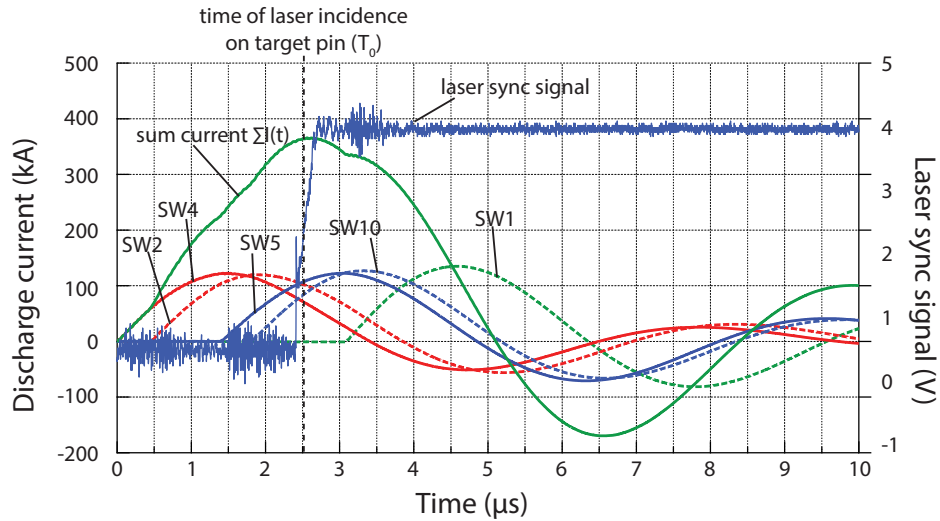


Figure 3.27: Asynchronously discharging capacitors can result in a poor superposition of currents. This reduces the peak current, which here occurs much later than the ideal-case $1.63 \mu\text{s}$.

severely during the Magnetized Blast Waves experiment #1 (MBW-1) experiment at the TPW, as demonstrated in Figure 3.27. Dirty spark gap switch electrodes can cause this, as can an improper switch gas pressure. In the case of MBW-1, dirty switches and aged trigger resistors were the likely culprit in the poor discharge synchronicity.

3.4 Magnetic field measurement

3.4.1 Coil types

Cluster fusion coil

MG2 experiments used two types of single-turn field coils as loads. The high-field coil, designed with magnetized cluster fusion in mind, is designed to yield as much field as possible in a 1.0 cm ID coil. The path of the cluster gas through the

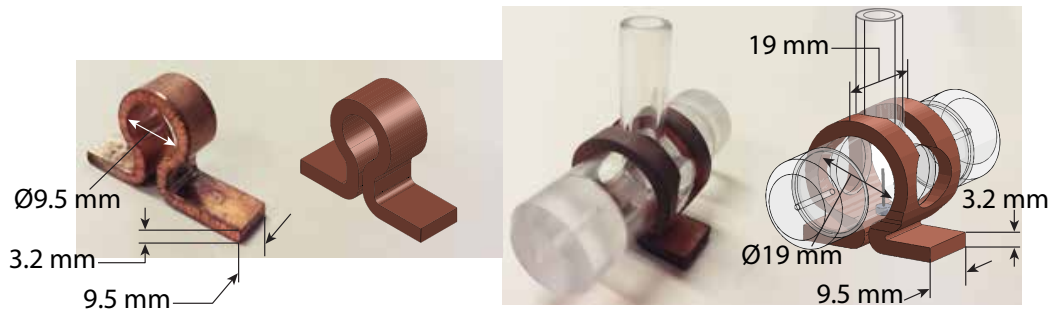


Figure 3.28: Photos of field coils and their CAD models with dimensions. Left: a high-field coil meant for maximum field generation for cluster fusion experiments. Right: a gas cell assembly for astrophysical blast wave experiments.

coil volume constrains the coil width to a minimum of about 1.0 cm, generating a mirror field. This path requires a cross-drilled hole of several millimeters on both sides of the coil. This precludes further reduction of the coil width, since there would not be sufficient material to withstand the shot's magnetic pressure, and the coil would tear apart before peak field. The high-field coils also served as the load during the high-field Faraday rotation measurements. Some of these coils, such as the one shown in Figure 3.28, did not have cross-drilled holes for the gas jet; this increased the strength of the coil for high-field shots and reduced fragmentation.

Blast wave gas cell coil

The second coil type is a portion of the overall target assembly for the magnetized blast wave experiment (MBW-1) on the TPW laser. This gas cell coil, pictured in Figure 3.28, is much larger, with an ID and length of 1.9 cm, and wraps around a polycarbonate gas cell of OD 1.9 cm and length 6.2 cm. The increased size of the coil reduces the field-to-current ratio, but this is acceptable with the low field (5-15 T)

requirement of the experiment. The lower field strength does not expand the coils as in the high-field case, but the two parallel loops attract each other by the $\mathbf{J} \times \mathbf{B}$ force, which can crush the gas fill tube attached to the top of the gas cell.

3.4.2 Field estimation with simplified model

Equation (2.3) can estimate each coil's on-axis magnetic field based on its geometry. Choosing a higher number of infinitesimal current loops distributed uniformly along the coil length approaches the more realistic picture of a continuous current distribution. In Figure 3.29, a model with nine current filaments better reflects the uniform current distribution model in the high-field coil; likewise, four filaments make up the current in the MBW-1 coil.

These field profiles are estimates since they do not consider effects such as distribution below the coil's inner surface due to the skin effect, nor heating and mutual inductance effects. The more rigorous filamentary current models in [42] and [47] take these effects into consideration, and give a method for numerically computing the time evolution of the current. This approach is a more advanced, dynamic version of the very simplified model of Figure 3.29. The numerical method can also calculate magnetic pressure, giving insight into the coil deformation during the shot.

Both the analytical and numerical models discussed here remain susceptible to errors arising from their assumptions. In both cases, cylindrical symmetry is not accurate, since the coils are not cylindrically continuous at the coil base. Coil features, such as holes drilled into the sides for a gas jet or probe beam, are cylindrically asymmetric features, cannot be addressed rigorously with these two-dimensional (2-D)

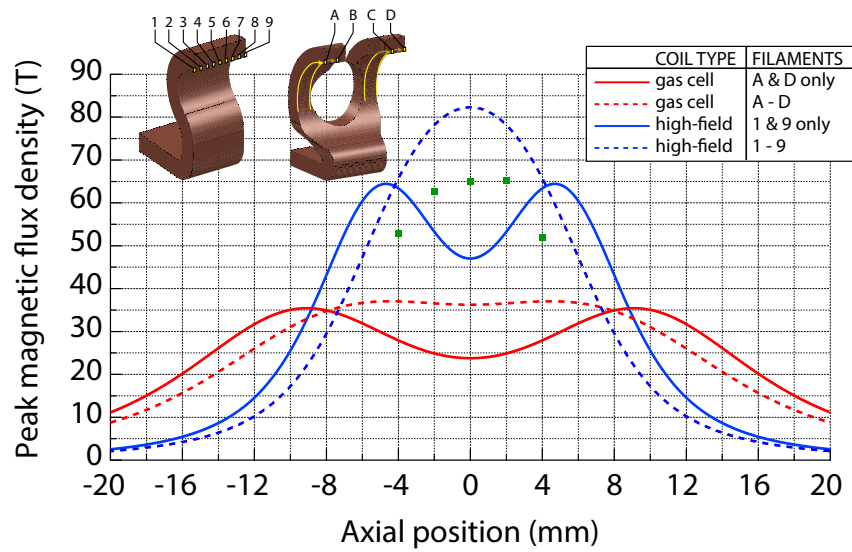


Figure 3.29: The magnetic field can be estimated by assuming the current is distributed along the coil length among several infinitesimally thin filaments lining the inner surface of the coil. Points are Faraday rotation measurements obtained from high-field coil shots (courtesy of S. Lewis).

methods. Also, axial deformations such as necking, or fissures at the coil edges cannot be considered in 2-D; although necking could raise current density through a narrowing conductor cross-section, and modeling fissures could help explain coil failure modes like tearing of the coil wall.

3.4.3 Faraday rotation measurement

Faraday rotation provides a direct measurement of magnetic field evolution by passing a polarized 5 mW, 532 nm laser beam through a cylindrical (OD 4.2 mm \times 4.0 mm) TGG crystal, which has a Verdet constant of 190 rad/(T·m) at the laser wavelength. The beam experiences polarization rotation when it passes through the magnetized TGG according to

$$\theta = \ell\nu B \tag{3.17}$$

where θ is the polarization rotation, ℓ is the length of the magnetized crystal, ν is the Verdet constant of the crystal, and B is the magnetic flux density.

A set of photodetectors measure the intensity of the S and P polarized components of the beam, and deconvolving the recorded intensities reveals a polarization rotation with respect to time. Dividing the polarization rotation angle by the Verdet constant and the crystal length gives the magnetic field, as in Figure 3.30.

Varying the crystal's axial position in the coil yields an axial field profile. A plastic fixture shaped to fit tightly inside the coil bore holds the crystal in a consistent location during these measurements. The field measurement is integrated across a small volume, defined by the beam diameter and the crystal length, and

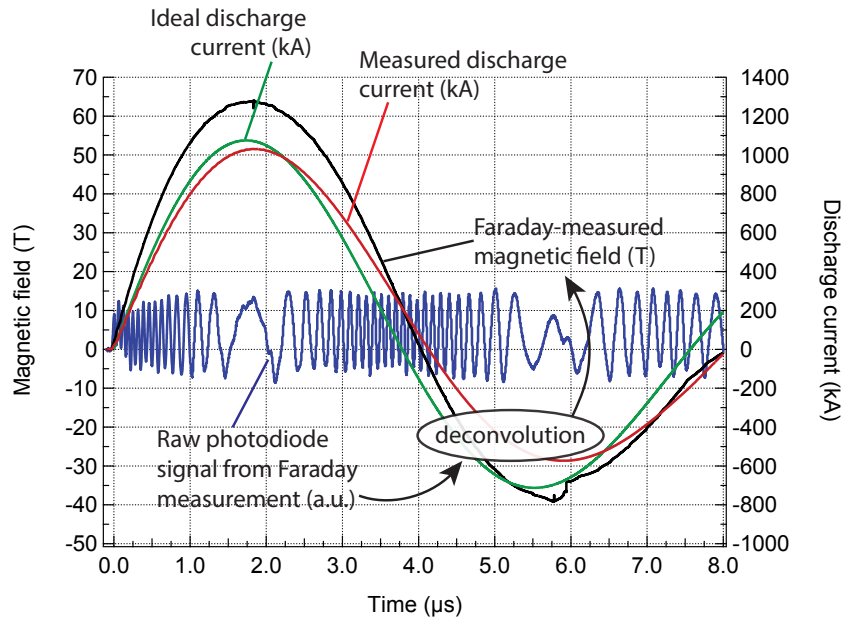


Figure 3.30: A measurement of the changing intensity of the S and P polarized components of a probe beam undergoing Faraday rotation yields the high-frequency trace, which is deconvolved using Equation (3.17) to give a magnetic field measurement. Expected and measured discharge currents are plotted for comparison with the field measurement.

the field measurement is an average across that volume. An ideal calculation using Equation (2.1) takes a moving spatial average of values from a field profile estimate, where the averaging window equals the crystal length. In this discussion, the beam will be considered infinitesimally narrow, the crystal's integration length will be set to its physical length of 4.0 mm, and the field calculations suppose $I_{pk} = 1.0$ MA unless otherwise noted. Sean Lewis (UT-Austin) played a key role in these measurements, primarily with the polarization detection circuit and subsequent numerical processing of those measurements.

High-field coil

At the coil center, the high-field coil's measured magnetic field, shown in Figure 3.31, is approximately 65.1 Tesla, and diminishes as the axial distance from the coil center increases. This is inconsistent with the mirror field predicted by a simple two-loop Biot-Savart calculation with the current loops on the edges of the coil, pictured in Figure 3.29 (filaments 1 & 9 only). This disagreement suggests the current is distributed along the whole length of the coil, and not just the edges. Adjusting the current distribution to be uniformly distributed (approximated with 9 equal loops along the coil length), the ideal model predicts an at-center field of 82.3 Tesla, although the axial field profile falls off axially. This overestimation suggests a current profile that is not strictly concentrated at the coil's inner surface, making the effective radius of the coil current greater. Likely causes for this are resistive heating in the skin layer that drives the current to the cooler outer layers of the coil, and coil expansion carrying the current away from the center. Additionally, the curvature of

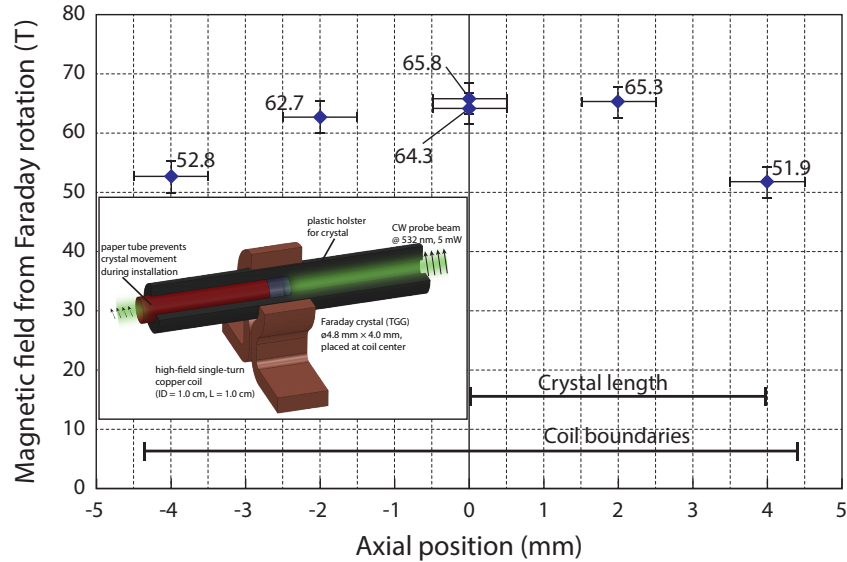


Figure 3.31: Faraday rotation measured values for magnetic field at several axial positions along the coil. Inset: TGG crystal placement inside high-field coil representative of the positioning method during collection of the plotted data. Horizontal error bars reflect uncertainty in crystal position; vertical bars are measurement error. Data points courtesy of S. Lewis.

the 9-loop model does not resemble the curvature of the data points.

Adjusting the ideal model of the coil to fit the Faraday measurements can produce a model that can better predict the field profile of a high-field coil, like the one in Figure 3.32. Note that these arguments and models only apply to an ID 1.0 cm \times 1.0 cm coil without the cross-drilled holes for cluster jet access. Faraday measurements using the accessed coils were not performed. More sophisticated models as discussed in [42, 47] can solve a dynamic current model and give a more realistic current distribution, such as the one shown in Figure 3.33.

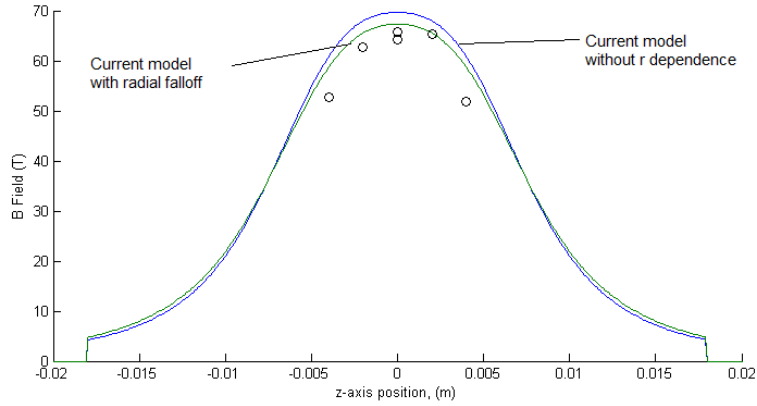


Figure 3.32: Using an axial distribution in combination with a radial falloff of current takes the estimate closer to the real measured field. Courtesy: S. Lewis.

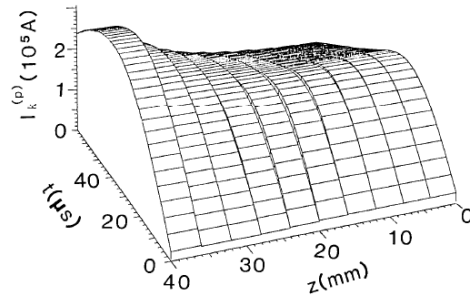


Figure 3.33: A more advanced model of current distribution, such as this one, from [42], can better simulate the magnetic field. However, generating such a model is more complicated compared to the simpler static model as in Figure 3.29.

Blast wave experiment coil

Time constraints limited the Faraday measurement of the gas cell coil field strength to a single shot (Shot 512), and its field measurement agrees with a simplified four-filament model shown in Figure 3.29. For this shot's maximum current of 543 kA, the measured field is 20.2 T at the coil center; the ideal model predicts 20.1 T. This gives a field-to-current scale factor of 0.0372 T/kA for the blast wave coil. The accuracy improvement is likely due to the two-loop shape of the gas cell coil, which reduces the uncertainty in axial current distribution. Additionally, the reduced current in the shot (543 kA vs. 1.0 MA) and the increased conductor cross-section diminish the heating and expansion effects that were likely causes for the inaccuracy in the high-field coil model.

Chapter 4

Experiment design and execution

4.1 Initial experiments

The designed purpose of the MG2 pulsed power system is to access the magnetized HED plasma [57]. Laser-generated cluster plasmas offer a path to this goal, and was the initial experimental focus after MG2 was operational. The next major MG2 experiment effort explored the effect of a strong magnetic field on radiative blast waves, and proceeded after the cluster fusion effort.

4.1.1 Cluster plasma generation

Clusters as an HED plasma source

Cluster production can occur when a fast-actuating valve releases a high-pressure backing gas into a supersonic nozzle [25]. The gas exiting the nozzle orifice into the expanding conical nozzle rapidly cools, and van der Waals' attractive forces cause the molecules to agglomerate into solid density droplets, which is schematically depicted in Figure 4.1. Gas backing pressure and temperature, nozzle design, and molecular weight affect cluster formation efficiency.

This is seen in the parameter Γ^* , introduced by Hagena [26], and expressed in

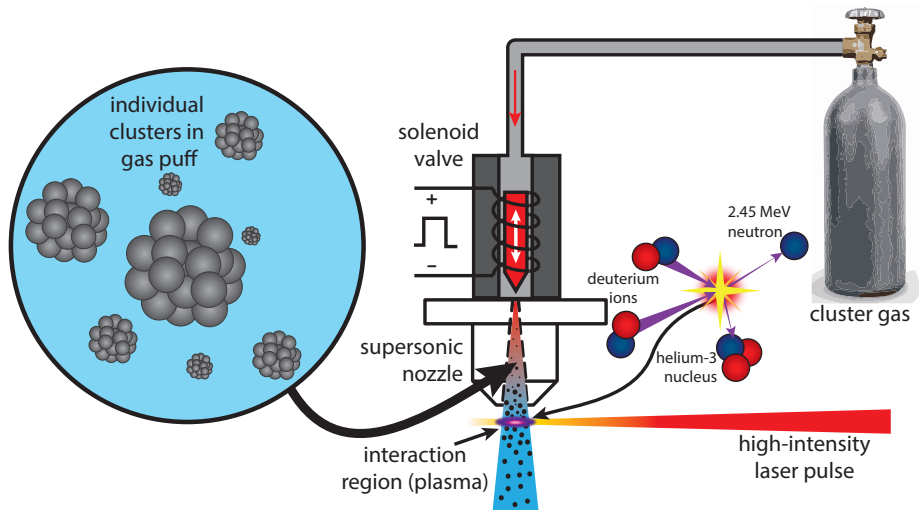


Figure 4.1: Clusters are created by releasing a burst of high-pressure (20 - 70 bar) gas through a supersonic nozzle. A high-intensity laser pulse ionizes the cluster plume 2 mm below the nozzle opening. High plasma temperature can yield nuclear fusion can occur if clusters contain deuterium.

more practical terms below, such that

$$\Gamma^* = k_h d^{0.85} [\mu\text{m}] P_0 [\text{mbar}] T_0^{-2.29} [\text{K}], \quad (4.1)$$

where k_h is a unitless gas-dependent constant, d is the nozzle aperture, P_0 is the backing pressure, and T_0 is the gas temperature [32]. The value of Γ^* will indicate the likelihood of clustering. Previous work has explored this parameter space; high-pressure, heavy noble gases are excellent for forming large clusters [25, 32, 36].

Clusters containing deuterium can generate hot ions by laser-cluster irradiation. Hot deuterons from neighboring clusters can collide and yield DD fusion, and the number of fusion events is measured with a neutron detector, such as a plastic scintillator coupled to a photomultiplier tube. This DD neutron yield has been

recorded in several experiments, including recent work at UT-Austin with the TPW Laser [3, 14, 65]. Preparatory work by the author on the smaller-scale GHOST Laser also showed evidence of DD neutrons from deuterium (D₂) and deuterized methane (CD₄) clusters.

Laser interaction & Coulomb explosion

Laser irradiation of clusters will result in cluster ionization when the electrons are accelerated out of the cluster by the laser's electric field. The percentage of electrons extracted by the laser pulse depends on the laser's intensity and frequency, and the cluster's size [5]. The ions, which are massive compared to the electrons, do not respond as readily to the field, resulting a net positive charge in the cluster once the electrons escape. Repulsion between the cluster ions can drive them apart with energies of several keV [6, 13, 39, 60]. This mechanism is known as Coulomb explosion, and is the primary method by which hot ions arise by cluster irradiation.

For Coulomb explosion to occur, at least some of the cluster electrons must be removed. For all electrons to be removed, leaving a fully stripped cluster, the electric field of the pulse must satisfy the inequality

$$R \ll \frac{eE_0}{m_e\omega^2} = 1.36 \times 10^{-7} I^{1/2} [\text{W}/\text{cm}^2] \lambda^2 [\mu\text{m}], \quad (4.2)$$

where E_0 , I , ω , and λ are the laser electric field, intensity, frequency, and wavelength, respectively, and R is the cluster radius [5]. Clusters with radii of a few nanometers can be fully stripped by a laser with $I \geq 10^{15}$ W/cm² and $\lambda = 1$ μm, which is accessible to many pulsed laser facilities. A cluster may also be partially stripped if the laser field is not strong enough to overcome the ions' attractive force on all of the electrons.

In addition to the intensity¹³ requirement, the laser pulse duration should be at most of the order of the ion motion time ($\tau_{laser} \lesssim 1/\omega_{pi} = \tau_i$) to use the simplification of stationary ions [5]. This is not a trivial requirement: for a deuterium cluster at solid density, $1/\omega_{pi}$ is only 11 fs; krypton clusters are slower at 70 fs, but will form larger clusters and require more laser intensity to fully strip.

4.1.2 Magnetized cluster fusion

Experiment concept

By applying a strong magnetic field to the cluster plasma, it should be possible to limit the plasma's expansion along the direction perpendicular to the field lines. A focused laser beam irradiating a cluster jet plume within an axial magnetic field will generate a cylindrical cluster plasma, which the field should confine radially if $\beta \sim 1$, although the plasma can escape freely out of the ends of the plasma, that is, along the field lines. Successful suppression of radial expansion will have the effect of increasing the plasma confinement time. For a plasma containing hot (several keV) deuterium ions, this would effect an increase in neutron yield, which could be detected as in [3]. MG2's magnetic field should accomplish this confinement by flowing a large drive current through a sufficiently small coil, generating fields approaching 100 tesla.

¹³The relation between intensity and electric field is: $I_0 = c\epsilon_0 n |E_0|^2 / 2$, where I_0 is laser intensity, n is the refractive index, and E_0 is the laser electric field.

Gas jet interaction with high voltage

The initial placement of the cluster jet assembly directed the cluster gas vertically, entering the top of the coil and injecting the cluster gas toward the A-K gap. Experiments with MG1 showed that this orientation caused arcing due to the gas's presence in the transmission line, which was likely providing opportunity for localized Paschen breakdown. Diverting the gas away from the transmission line prevented breakdown, but exploratory X-ray and neutron yield measurements suggested this compromises cluster formation in the magnetic field region.

Reorienting the gas jet to enter along the coil's side and exit through the opposite side via cross-drilled holes in the coil avoids breakdown since the exiting gas is directed away from the A-K gap. However, this requires placing the stainless steel gas jet assembly close to the transmission line, which promotes breakdown. The technical difficulty of the magnetized cluster fusion experiment remains unsolved due to this precarious balance between cluster production and arcing avoidance.

These cluster injection complications mandate a significant change to the experiment. A parallel plate or coaxial transmission line in lieu of a conical one may be a solution, much like MIFEDS or the pulsed power device in [38]; this would distance the gas jet hardware from high voltage elements, reducing the chances for arcing to those components. More robust insulation in the coil and A-K gap vicinities may also prevent these arcs. Further complications arise with high field coils exploding into the gas jet assembly: supersonic nozzles can be fabricated cheaply, but one solenoid pulse valve costs several hundred dollars, making each shot costly if this valve is destroyed.

4.2 Magnetized blast waves

MegaGauss 2 fields can simulate an astrophysical condition in which a blast wave (e.g. from a supernova) propagates into a background magnetic field. Vishniac [61, 62] expected a perturbation growth rate in a blast wave into a surrounding medium, which has applications to phenomena including the propagation of supernova blast waves into the interstellar medium. Vishniac also proposed that the addition of a magnetic field may provide a stabilizing force which changes the growth of the perturbation. A high-intensity pulsed laser irradiating a solid target immersed in a gas can generate comparable blast wave conditions in the laboratory. Adding MG2 to this arrangement gives the opportunity to observe the magnetic field's effect on the blast wave, such as the field strength at which the blast wave characteristics are altered, the nature of those alterations, and the effect on the growth rate of the perturbation Vishniac predicts. This is of primary interest to Nathan Riley (UT-Austin), who is investigating the behavior of the blast waves; the MG2 system serves as the magnetic field source.

4.2.1 Description of target

Polycarbonate gas cell

A polycarbonate gas cell, pictured in Figures 4.2 and 4.3, consisting of a hollow cylinder (OD 19.1 mm), two end caps, and a fill tube contains the background gas into which the blast wave propagates. A vacuum-compatible adhesive joins these pieces into a miniature chamber, and fixes a nylon pin (OD 0.7 mm) to the bottom of the cylinder, with the pin's tip at the center of the gas cell. A 1.2 mm pinhole through each end cap provides access for the long-focus (f/40) pump beam. For optical

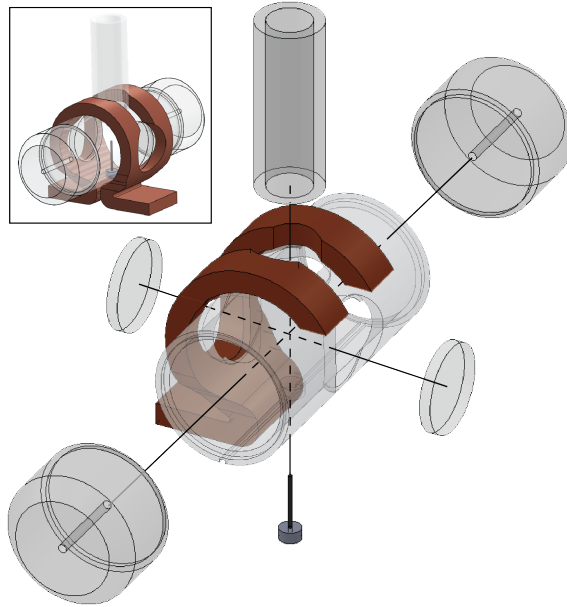


Figure 4.2: Exploded diagram of the gas cell assembly, with coil partially hidden to expose features on the polycarbonate body. The target pin is glued into a socket at the bottom of the body. Once the pin is secure, the body is inserted into the coil, and the remaining gas cell pieces are added. Inset: a completed assembly.

diagnostics, AR coated windows (OD 12.7 mm) are adhered to fitted sockets on either side of the cylinder. A flexible fill gas line presses tightly around the fill tube (ID 6.4 mm), which is adhered to the top of the cylinder. During evacuation, the cell exhausts through the pinholes in the end caps. The time scale of this evacuation is short enough that the gas cell volume is not troublesome for vacuum pumping; but is long enough to maintain a steady background pressure on the time scale of the blast wave during a shot.

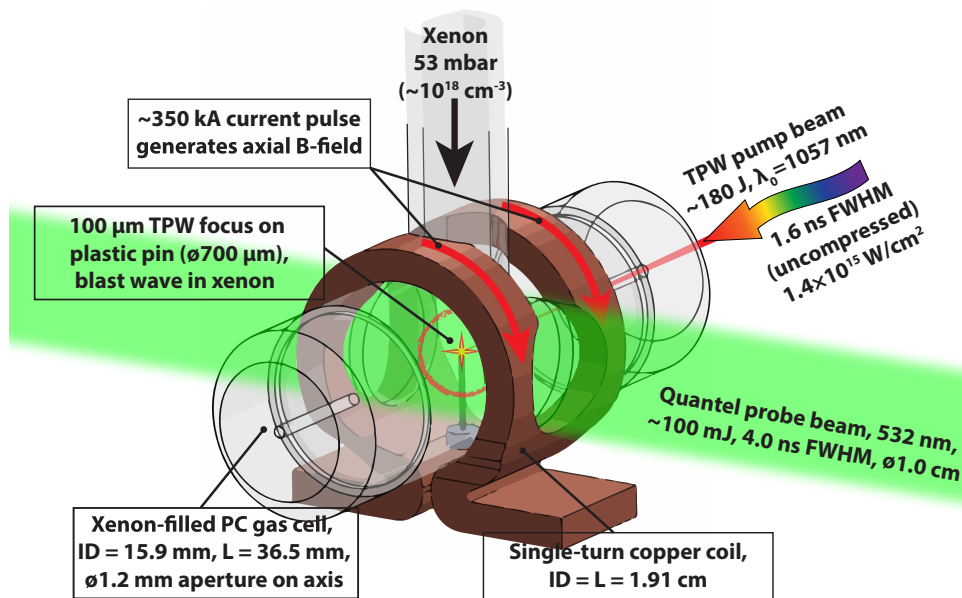


Figure 4.3: Target designed for MBW-1 experiments. Field coil wraps around polycarbonate gas cell. TPW beam enters and exits through pinholes along the long axis of the gas cell; diagnostic beam is perpendicular to the long axis and passes through AR windows on the gas cell.

External field coil

A field coil with ID 19.1 mm fits around the gas cell assembly. A shaping press forms the coil from a single strip of 3 mm copper, and a computerized milling machine cuts access holes for the fill tube and diagnostic windows. The coil's end-to-end length matches the cylinder's at 19.1 mm, and has a 6.4 mm slot in the middle, effectively forming two parallel loops. This slot stops at the coil base, which tapers to a width of 12.7 mm to match a coil clamp bolted to the top of the triplate transmission line. Since the fill tube and diagnostic windows extend beyond the OD of the cylinder and end caps, the gas cell must be assembled in place, inside the coil. The gas cell and coil fit together concentrically, and if the target pin is placed correctly, the tip of the target pin, the center of the coil, and the center of the gas cell will all be coincident.

4.2.2 Gas fill testing with pulsed power

In preparation for MBW-1, a miniature pressure transducer fitted to a gas cell measured the time behavior of the internal pressure of the cell. A solenoid valve¹⁴, similar to the type used in the cluster experiments, gated the fill gas entering the cell. By varying both the backing pressure and the valve open time, the fill trials gave the ideal operating parameters that filled the cell with 40 Torr of nitrogen¹⁵. A digitizing oscilloscope¹⁶ monitored the pressure transducer's signal and measured the time to

¹⁴Parker Hannifin 009-0089-900

¹⁵To conserve xenon (the experiment's fill gas), the fill times for nitrogen and xenon were assumed to be equal. In reality, this may be inaccurate, and xenon pressure during MBW-1 could be less than measured in these fill trials.

¹⁶Tektronix TDS 3054B

reach the 40 Torr setpoint as a function of backing pressure and open time. An Iota One pulse valve driver¹⁷ controlled the solenoid valve's open time, and a compound pressure gauge gave a measurement of the backing pressure. For all trials, the gas cell was in vacuum to observe the balance between cell fill time and cell evacuation time, and the ambient pressure was at most 200 mTorr. Refer to Tables 4.1 to 4.4 for the gas fill results.

With the optimized parameters of 1.0 atm backing pressure and an open time of 6 ms, MG2 shots indicated that the addition of the gas fill did not interfere with the pulsed power discharge. This was a critical result, in light of the difficulty of operating the cluster jet and pulsed power together. The gas cell diverts the injected gas, forcing the gas to exit through the end cap pinholes and away from the A-K gap. In addition, positioning the solenoid valve outside the MG2 vacuum chamber situates the valve's metal elements far from the high voltage region.

4.2.3 TPW description

Beam characteristics

Blast wave generation is driven by the TPW Laser operating in its long-focus (f/40) mode. In this mode, the beam comes to focus in the TPW Target Area 2 (TA-2), where MG2 integrates with the preexisting vacuum system. At full energy, the compressed TPW pulse is 190 J with a full width half maximum (FWHM) of 170 fs, and is frequency-chirped with a center wavelength of 1057 nm. Cool-down

¹⁷Parker Hannifin 060-0001-900

Backing pressure (atm)	Open time (ms)	Pressure (Torr)	Fill time (ms)
0.3	5	13	5.9
0.3	10	29	8.7
0.3	15	43	13.5
0.7	5	27	6.4
0.7	10	61	9.3
0.7	7	41	7.3
0.7	9	51	8.4
1.0	5	39	6.7
1.0	7	62	7.6
1.0	9	78	8.4
1.0	11	98	10.2
1.5	5	65	6.4
1.5	3	38	5.5
1.5	4	53	6.2
1.5	2	26	5.4
1.5	6	87	7.0
2.0	2.5	47	5.3
2.0	2	37	5.3
2.0	1.5	28	5.0
2	3	59	5.2

Table 4.1: Gas fill trial #1: Parker 099-0065-900 pulse valve (flow aperture ID .76 mm).

Backing pressure (atm)	Open time (ms)	Pressure (Torr)	Fill time (ms)
0.3	5	13	5.9
0.3	10	29	8.7
0.3	15	43	13.5
0.7	5	27	6.4
0.7	10	61	9.3
0.7	7	41	7.3
0.7	9	51	8.4
1.0	5	39	6.7
1.0	7	62	7.6
1.0	9	78	8.4
1.0	11	98	10.2
1.5	5	65	6.4
1.5	3	38	5.5
1.5	4	53	6.2
1.5	2	26	5.4
1.5	6	87	7.0
2.0	2.5	47	5.3
2.0	2	37	5.3
2.0	1.5	28	5.0
2	3	59	5.2

Table 4.2: Gas fill trial #2: Parker 009-0089-900 pulse valve (flow aperture ID 2.95 mm).

Backing pressure (atm)	Open time (ms)	Pressure (Torr)	Fill time (ms)
1	5	30	5.8
1	7	53	7
1	9	75	7.8
1	11	99	9.4
1	6	42	6.8
1	5.5	34	6.4
1	5.8	38	6.7
1	5.8	38*	6.8*

Table 4.3: Gas fill trial #3: Same as trial #2, but a plastic fill tube length (4.4 cm) was added to electrically insulate the pulse valve from the MG2 chamber. *8-point average.

Backing pressure (atm)	Open time (ms)	Pressure (Torr)	Fill time (ms)
1.0	4	20	5.8
1.0	5	32	6.0
1.0	6	41	6.4
1.0	7	53	6.8
1.5	4	11	5.7
1.5	5	28	5.9
1.5	6	50	5.9
1.5	7	66	6.2

Table 4.4: Gas fill trial #4: Same as trial #3, but pressures and fill times are 4-point averages. A turbopump reduced ambient pressure to <10 mTorr to remove potential influence on the gas fill time.

time between full-energy shots is 1 hour; lower energy shots are also possible at 7 J with a 15 minute cool-down or 100 mJ at 2.5 Hz [34]. A continuous wave (CW) beam propagating through the laser chain along a path collinear with the main beam serves as an alignment aid during target setup.

Chirped pulse amplification (CPA) is the principal technique that enables the creation of the high-intensity, ultrafast pulses in the TPW. By temporally stretching an initial frequency-chirped pulse, the pulse can pass through a chain of laser amplifiers without the threat of optics damage from an intense beam. Once the amplification is complete, the pulse is temporally re-compressed, which greatly raises the pulse intensity. Technical details of CPA will not be discussed here, but are partially illustrated in Figure 4.4, and discussed briefly in [21].

In the case of the blast wave experiment, beam intensity is not as crucial as in experiments that explore high-intensity effects (e.g. cluster ionization). Rather, pulse energy is the relevant parameter, and the pulse compression stage can be bypassed. Operating in this long pulse mode reduces the chance of damaging optics with the high-intensity compressed pulse, and avoids beam self-focusing in the gas cell. The f/40 focusing mirror concentrates the beam to a focal diameter of 100 μm (FWHM), with a 2.0 ns FWHM duration in the uncompressed state, giving a focal spot peak intensity of 1.2×10^{15} W/cm².

The f/40 focusing mirror is on a combined translation and 2-axis kinematic stage, allowing the focus to move horizontally, vertically, and along the beam's propagation axis. Because the target pin is 700 μm in diameter, the entire 100 μm focus should strike the pin, given an accurate alignment. Any remaining laser energy

that misses the target continues downstream, defocuses, and eventually is absorbed by the TPW main beam dump.

Laser layout

The TPW Laser area, shown in an overhead view in Figure 4.5, is divided into two large rooms: the laser bay, and the target area. The laser bay is restricted mostly to TPW staff, and houses the majority of the optical components, such as the pulse stretcher, amplifiers, and beam diagnostics. The target area houses the pulse compressor, the vacuum chambers where the laser comes to focus, and most of the beam tubes that maintain high vacuum for the pulse's safe propagation. All experiment apparatus typically resides in the target area only, since the focused beam is delivered there.

Due to the geometry of the blast wave experiment, the long, narrow focus provided in TA-2 is preferable to the short focal length of the $f/3$ mirror in Target Area 1 (TA-1). Additionally, the application of the pulsed power equipment demands sizable floor space, which is not available in TA-1. Within TA-2, there is sufficient space in the beam tube chain to remove elements and replace them with MG2 components, most significant of which is the MG2 chamber itself. Although limited, there is empty floor space near the beam tube chain where the capacitor bank fits, and is close enough for the 3.0 m discharge cables to reach the chamber after it is integrated into the beam tube.

Before firing a full-energy shot (system shot), the TPW staff performs a security sweep of the laser bay and target area to ensure no personnel are in the vicinity during

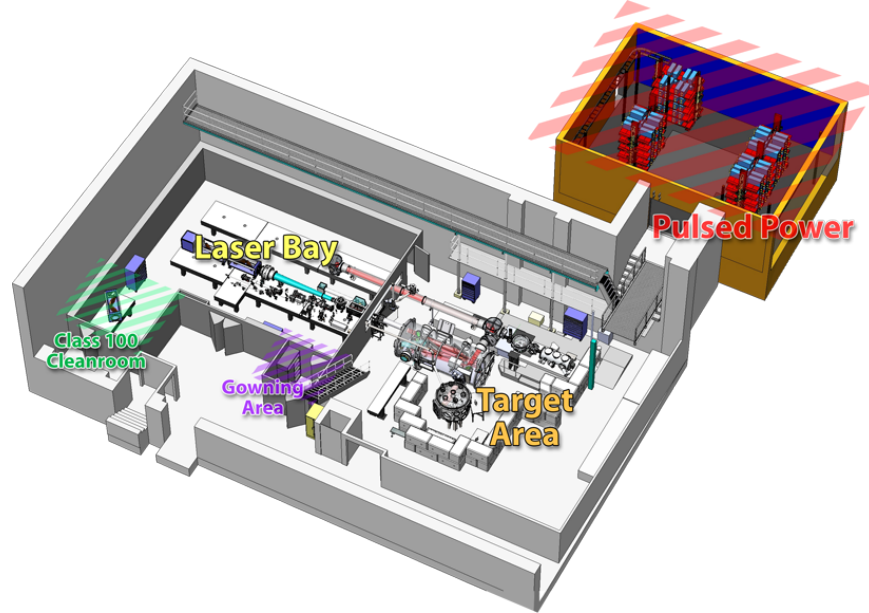


Figure 4.5: Floor plan of the Texas Petawatt Laser [1]. The region labeled Target Area hosted the MBW-1 experiment.

the shot. Both rooms are designed with safety interlocks on all entries that interrupt laser operation when broken. A 60 cm thick concrete wall surrounds the target areas to attenuate radiation from experiments; outside this wall, there is additional floor space for peripheral devices, target preparation, etc. In the blast waves experiment, this space accommodated MG2’s charging, triggering, and control equipment.

4.2.4 Implementation of MG2 on TPW

Vacuum design

To deliver the TPW laser pulse onto the target pin inside the MG2 chamber, the MG2 chamber must be integrated into the TPW vacuum system. Ordinarily, a general-use chamber resides at the focal position of the long focus beam line. The

MG2 chamber replaces it, and this change requires modification of the vacuum pump ports and coupling tubes between chambers. Computer-aided design (CAD) software gives a visualization of the design changes that make the TA-2 beam line compatible with this new hardware. TPW staff provided original CAD models of TA-2 as a starting point for MG2 chamber integration and capacitor bank positioning. Due to the small volume of the chamber, the original roughing vacuum pump and turbopump arrangement in TA-2 is sufficient to evacuate the modified vacuum system.

Layout of system in target area

The default layout of TA-2 has three experiment chambers in the beam line; the largest chamber is provided for general experiment use, and is positioned at the focus. In the layout for MBW-1, the MG2 chamber replaces this chamber. The other two chambers provided convenient pumping and adaptation ports, and remained in the vacuum arrangement. The MG2 chamber is placed such that the TPW beam comes to focus at the gas cell target's center, on the target pin, as in Figures 4.6 and 4.7. The small apertures of the gas cell and the chamber's KF-16 vacuum ports (ID 1.2 mm and ID 16 mm, respectively) require the chamber position to be fixed such that the gas cell entry pinhole is concentric with the laser axis. Since the KF-16 port, chamber, coil clamp, coil, and gas cell are all rigidly fixed to each other, moving either the MG2 chamber or the beam are the only alignment options. During the alignment process, it became apparent that if the beam was approximately concentric with the KF-16 port, manipulating the focusing mirror's kinematic stage to point the beam into the gas cell pinhole was straightforward.

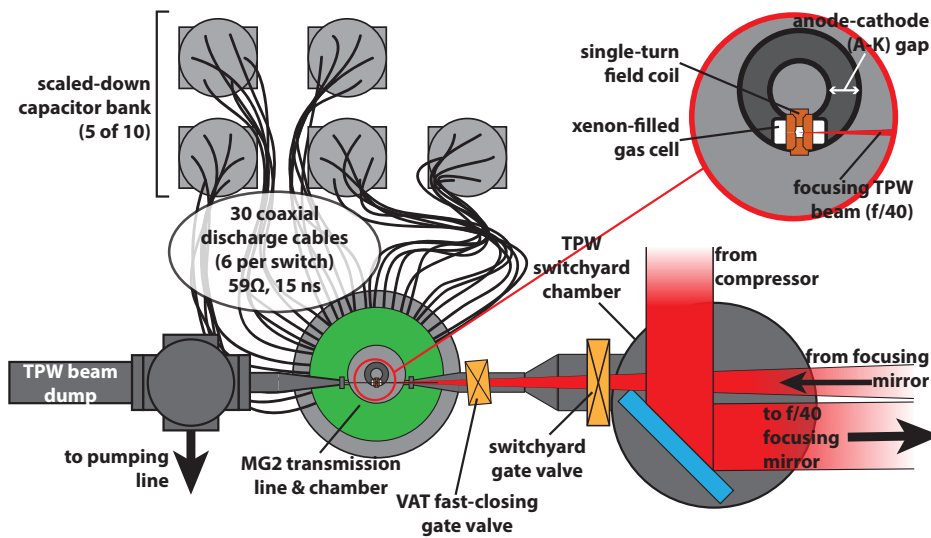


Figure 4.6: Schematic layout of MG2 in the TPW target area for the blast waves experiment shows the placement of the capacitor bank and chamber in the TPW beam line.

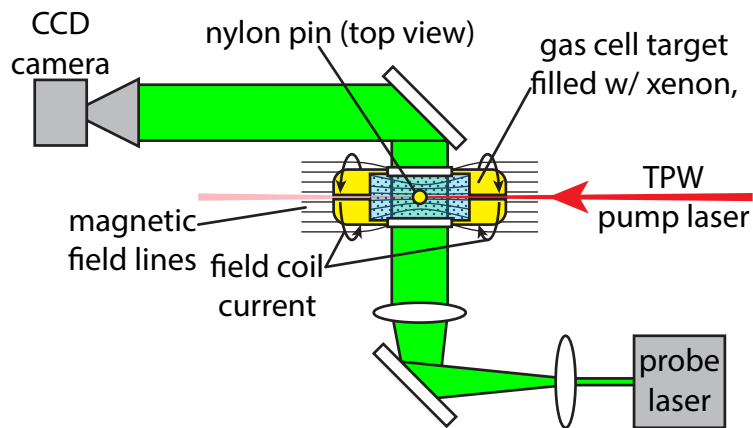


Figure 4.7: Schematic arrangement showing relation of TPW beam, diagnostic path, and target.

Five capacitor bank modules can provide more than enough current to drive the 5–15 T magnetic fields needed for MBW-1. Due to the size of the capacitor modules and the discharge cable length constraint of 3.0 m, the most reasonable position for the bank was an area adjacent to the TA-2 laboratory table that supports the MG2 chamber. This position gave easy access to the opposite side of the MG2 chamber for target replacement.

The charge dump tank, electronics control rack, and B-dot oscilloscopes resided in the target preparation area behind the concrete shielding wall, about 15 m from the capacitor bank. The trigger tank stood halfway between the charge dump tank and the capacitor bank since the trigger cables are considerably shorter than the capacitor charge cables. Oscilloscopes monitored each capacitor's B-dot current sensor via RG-58 signal cable routed through the concrete wall.

A high-pressure xenon cylinder pressurized an intermediate vessel to the desired fill gas backing pressure. The xenon manifold, including the intermediate vessel, was purged of air by closing the xenon cylinder, opening all other valves on the fill manifold, and triggering the solenoid pulse valve intermittently with the MG2 chamber at vacuum. Once the chamber pressure ceased to rise while the valve was open, the manifold was sufficiently purged. After the purge, the xenon cylinder, with a low pressure on its output regulator, slowly filled the intermediate vessel with 1.0 atm of xenon. Once the intermediate gas vessel reached 1.0 atm, the main xenon cylinder was closed, leaving the intermediate vessel to provide the backing pressure to the pulse valve.

Integration with TPW safety procedures

The TPW door interlock signal controlled a normally open mechanical relay that gated the 120 VAC coil current that opens the dump relay. This prohibits the capacitors from charging unless the TPW interlocks are closed. This arrangement bypasses any control electronics, and will dump the charge bank in the event of a power failure. A brass plate under all five capacitors provided a common ground for the capacitors' cases, and all capacitors had a dedicated grounding strap secured to a nearby earth ground in TPW Target Area 1 (TA-1). The capacitor shorting levers in each switch enclosure remained in their safe position until the TPW staff performed the safety sweep just before a system shot.

A network connection to the control electronics rack enabled remote control of the MG2 electronics from the TPW control room. With the interlock system engaged, MG2 operated in synchronization with the command of the TPW operator. The TPW operator coordinated with the MG2 operator such that the laser flashlamps' capacitor bank and the MG2 capacitor bank completed their charge sequences simultaneously. Minimizing the voltage hold time reduced capacitor stressing and reduced the chance of an MG2 prefire. In addition to these engineered safety features, an updated TPW hazard list included the pulsed power hazard in the target area, signs indicating these new hazards were posted on all target area entries, and personnel access was reduced to those who had been trained on the new hazards introduced by MG2.

Integration with TPW timing and triggering

During the pre-experiment setup, with the TPW operating in 2.5 Hz (~ 100 mJ) mode, a photodiode placed in the target chamber detected the laser's arrival in the chamber. This arrival time is measured with respect to a master timing pulse from the TPW timing system to determine the exact delay between the master timing pulse and the laser's arrival in the chamber. This gives a measurement for the laser arrival time T_0 , from which other experiment events such as the gas fill, MG2 trigger, and diagnostics probe pulse are delayed.

4.2.5 Diagnostics

Schlieren photography

Schlieren photography, schematically explained in Figure 4.8, highlights the blast wave evolution at an instant in time by revealing the blast wave's scattering of probe beam light. After passing through the gas cell, the probe beam is focused to a point, which is obstructed by a beam block. Undisturbed light that cleanly focuses to a point is blocked, but the light scattered by the blast wave is not, and misses the beam block. This leftover light is collected, the image of which shows the form of the blast wave. This is a 2-D diagnostic, although imaging into a framing camera can add time-resolved information.

In the case of MBW-1, only one probe beam and the absence of a framing camera limited data to one Schlieren image per shot. The beam block in this case was a razor blade, which blocked one half of the scattered light. The resulting image appears to have the density gradients illuminated from one direction, similar to the

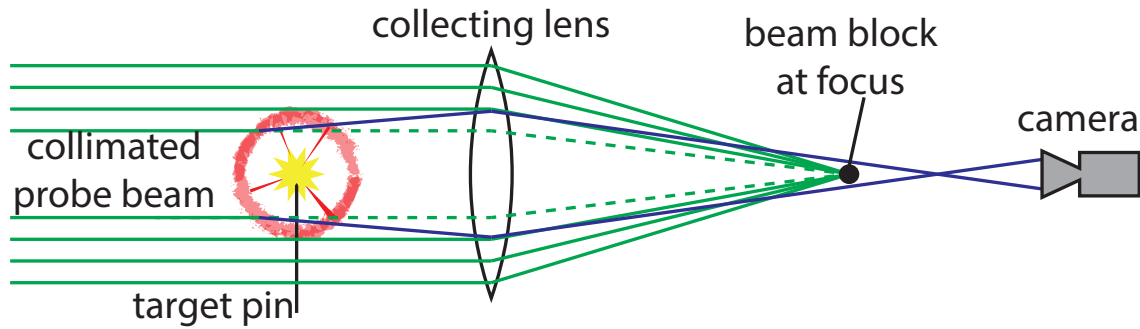


Figure 4.8: Schlieren photography schematic. Unscattered light encounters a beam block at the focus of a collecting lens. Light scattered by density perturbations (e.g. a blast wave) has its trajectory modified, and is thereby diverted around the beam block to be captured by a camera.

appearance of a textured object exposed to light from a steep angle, much as a relief sculpture illuminated by an overhead light [50].

Nomarski interferometry

Interferometry is a common diagnostic in plasma physics, since the plasma density has an effect on the refractive index. This provides a 2-D snapshot of the plasma density once the appropriate phase deconvolution is applied. Thinking of the probe beam as a collection of collimated rays passing through the plasma, with each ray slowed some Δt depending on plasma density, the probe beam can accumulate rays with different phase delays. This generates a map of phase shifts across the probe beam, such that $\phi(x, y) = 2\pi c\Delta t/\lambda$, where $\phi(x, y)$ is the 2-D phase map over the probe beam's area and λ is the wavelength of the probe beam. When the phased (sample) beam is interfered with an unphased (reference) beam, their constructive and

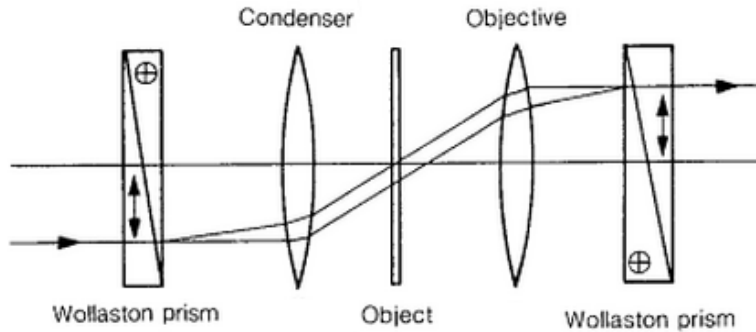


Figure 4.9: Nomarski interferometry can use a single beam to produce an interferometric measurement by dividing a single probe beam into two oppositely polarized beams [27].

destructive interferences appear as light and dark regions corresponding to the 2-D density map of the plasma.

In the MBW-1 diagnostics configuration, the reference beam also had to pass through the plasma, making the interferogram a measurement of not absolute, but relative phase change. Separation of the two beams, which were constrained by the target geometry to be approximately collinear, was a problem in this configuration. A solution to this problem is the Nomarski interferometer, pictured in Figure 4.9, which uses a polarizing prism (e.g. Wollaston prism) that splits the probe beam into its consistent perpendicular polarizations, with a slight separation between the beams. After passing through the plasma, the two beams are recombined, producing an interferogram.

4.2.6 Expectations

Effect on blast waves

The primary purpose for applying the magnetic field to the blast wave is to observe its effect on the blast wave's temporal evolution. One effect that could be observed is a modification of the Taylor-Sedov solution, a relation between the blast wave radius and time such that $r \propto t^n$, where n is the number posed by the Taylor-Sedov solution. Additionally, the Vishniac perturbation may exhibit special behavior under the influence of a magnetic field, as predicted in [61]. The magnetic field can provide an environment to study this effect. Most of these blast wave effects are of primary interest to Nathan Riley (UT-Austin), who is studying the spherical blast waves generated in this and future experiments. Riley will publish the results of his studies at a later date, and thus are not the subject of this dissertation.

Plasma confinement

Application of the magnetic field will have the additional effect of confining the radial expansion of the plasma generated by the laser's interaction with the target. Plasma can also arise as a result of the blast wave heating the surrounding gas, but the following discussion focuses on the more general plasma confinement concept, not the particular applications of the blast wave to that effect. In general, plasma confinement will occur when the plasma pressure nkT is balanced by the magnetic pressure $B^2/2\mu_0$, or $\beta = 1$, where β is the ratio of plasma pressure to magnetic pressure. The mechanism by which the confinement takes place is the application of the Lorentz force on the radially-traveling electrons, diverting the electrons along the

azimuthal direction, causing the electrons to orbit the field lines, instead of allowing them to escape radially.

In the unconfined case, the relatively low-mass electrons attempt to escape first, but the oppositely-charged ions detain them as the space charge between the opposite charges grows. Thus, it may be said that the electrons “drag” the more massive ions along; this occurs at the sound speed

$$C_s = \sqrt{\frac{\gamma Z k T_e}{m_i}}, \quad (4.3)$$

where γ is the adiabatic constant, which is 5/3 for a monatomic gas such as xenon.

For $\beta = 1$, the field restricts the electrons’ radial motion by redirecting their travel with the $J \times B$ force, although they can escape freely out of the ends of the plasma. If the plasma’s length is much longer than its radius, the electrons must travel much further to escape, slowing the overall plasma expansion. In the radial confinement picture, the electrons will orbit the field lines with a characteristic gyroradius (Larmor radius), given by

$$\rho_L = \frac{m_e v_\perp}{eB}, \quad (4.4)$$

or practically, $\rho_L[\mu\text{m}] = 2.38 T_e^{1/2}[\text{eV}]/B[\text{T}]$. Here, v_\perp is the component of the electron’s velocity that is perpendicular to the field line it orbits, and T_e is the electron temperature. Note that $v_\perp = \sqrt{k_B T_e / m_e}$ for an electron where $|\mathbf{v}| = v_\perp$.

At the fields expected for MBW-1 (5 T in this example), $\beta = 1$ for a plasma pressure of 9.9 MPa. Assuming a singly ionized plasma formed from a 20 Torr background gas at room temperature, the number density n is $6.4 \times 10^{17} \text{ cm}^{-3}$, and at $\beta = 1$ the plasma temperature is 96 eV, with a Larmor radius of 4.7 μm . This Larmor

radius is small compared to the initial plasma size ($\sim 100 \mu\text{m}$, the laser focus diameter), and this implies plasma confinement will be very strong. That is, the plasma should not expand greatly beyond its initial diameter. Expansion beyond this Larmor radius scale would suggest the electron temperature exceeds 96 eV, and the plasma should expand until $\beta \approx 1$. Effects such as collisions can reduce the confinement effectiveness; this is discussed in Chapter 5.

Chapter 5

Experiment results from MBW-1

5.1 Pulsed power performance

Field delivered

To meet the minimum field requirement of 5 T, the drive current must peak at 134 kA. The two-capacitor configuration is sufficient to reach this current, provided the capacitors discharge synchronously. Adding capacitors to the circuit will raise the maximum current and field. In the case of MBW-1, a timing pulse synchronized with the laser signaled the time of incidence (T_0) on the target pin with respect to the discharge. This timing pulse, visible in Figure 5.1, provides a method of knowing the discharge (i.e. field) level at T_0 , rather than assuming the laser and the pulsed power discharge are synchronized.

Each shot is assigned a calculated peak field based on the discharge value at T_0 . The scale factor of 0.0372 T/kA was obtained by Faraday rotation measurement, detailed in Section 3.4.3. The discharge current is the sum of currents from each switch, including any asynchronous effects that may occur due to poor switch triggering; that is, all currents are measured with respect to the same trigger pulse from the high-voltage Maxwell trigger generator. Usually, T_0 and the discharge peak will not occur simultaneously, making $B(T_0) < B(\tau_{pk})$.

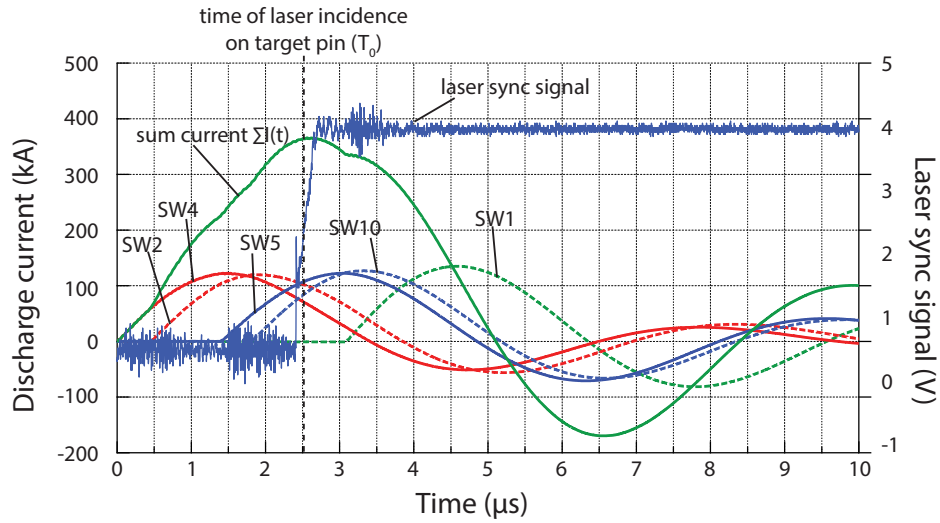


Figure 5.1: MG2 Shot 534 shows asynchronously discharging capacitors resulting in a poor superposition of currents. This reduces the peak current, which here occurs much later than the ideal $1.63 \mu\text{s}$. A laser sync pulse shows the laser's arrival on target with respect to the discharge timing.

In the first shot mode, the experiment plan called for a relatively high field of 15 T. Significant asynchronicity between the capacitor modules required all five capacitors charged to 50 kV to reach this field. Although the expected peak current from such a shot is 500 kA, the poor superposition of the discharges resulted in less. Next, the shot plan called for 5 T, attainable with two synchronized capacitor modules charge to 30 kV. The third and final series of shots doubled the charge on both of the capacitors to reach for an intermediate field strength between the first two. The discharge currents and magnetic field densities are shown in Figure 5.2.

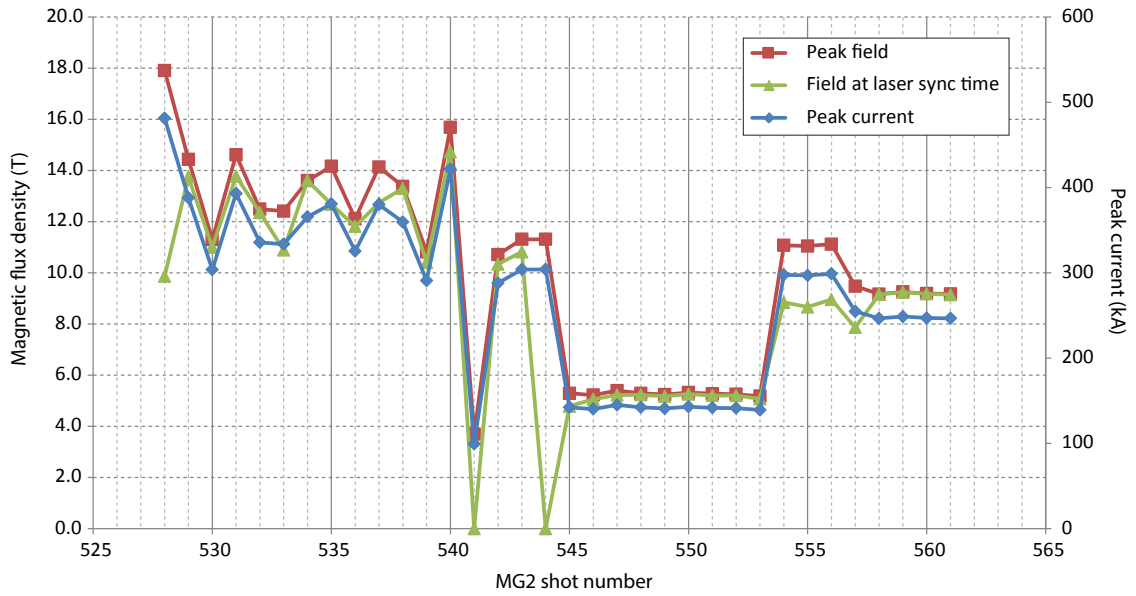


Figure 5.2: Peak current and field, and field upon laser incidence on target for each MBW-1 shot. Increase in consistency in second and third shot groups is due to reduction from five to two capacitor modules, which improved discharge synchronization. Zero values are due to failed measurement or discharge faults (e.g. breakdown).

Asynchronous capacitor discharges

Recall the rule of thumb formula for estimating MG2’s peak discharge current

$$I_{pk}[\text{kA}] \approx 2N \cdot V_{chg}[\text{kV}], \quad (5.1)$$

as stated before in Equation (3.16). With the reduced capacitor bank ($N = 5$) used in the experiment, a 50 kV charge should result in a 500 kA (19 T) current peak. In fact, average peak current under these conditions yielded an average of 366 kA (14 T), seen in Figure 5.2. Asynchronous discharging of the capacitors was the cause of this current reduction, and this prevented superposition of the individual capacitor module discharges.

This asynchronous discharge is clearly visible in Figure 5.1, a plot of individual switch currents and the resulting sum current. This effect was pervasive throughout the experiment, and could not be corrected by adjusting the spark gap switch pressure. In a few shots, one switch did not discharge during the oscilloscopes’ acquisition time, giving low (≤ 300 kA) peak currents. Post-experiment, an examination of the switches revealed electrode contamination caused these faults. During the run, two switches were approximately synchronous, and these were later isolated and used exclusively during the second and third stages of the experiment. Limiting the capacitor bank to these two reliable switches reduced the peak current variation, as is seen in Figure 5.2 for Shots 545–561.

Varying β conditions

Magnetic fields of different strengths will affect the plasma differently, and this is expressed in terms of the plasma’s β value, the ratio of the plasma pressure

to the magnetic pressure. A plasma in which $\beta \leq 1$ is said to be magnetized. Such a plasma will not expand hydrodynamically according to the plasma pressure nkT . Instead, its expansion across the field lines will be inhibited, and the expansion will proceed mostly along the field lines. This gives rise to a topological difference in the plasma's appearance: in the unmagnetized case, a spherically or cigar-shaped plasma expanding in all directions is likely, but in the magnetized case, this initial shape should only expand along the ends of the plasma, elongating the plasma's shape. The plasma temperature for which $\beta \leq 1$, assuming constant density, will scale as the square of the field. For the three field conditions, nominally 5, 10, and 15 T, assuming a plasma density of $1.3 \times 10^{18} \text{cm}^{-3}$, the field will magnetize plasmas with $T \leq 47$, 191, and 430 eV, respectively. If the plasma temperature exceeds the maximum confinable temperature, it will expand until $\beta \approx 1$, at which time the plasma becomes magnetized.

An unrestricted plasma will expand hydrodynamically at a characteristic time found by calculating the sound speed with Equation (4.3). For singly ionized xenon at 430 eV, $C_s = 22.9 \text{ km/s}$. If plasma is in a vacuum with no magnetic field, 50 ns after plasma generation, the characteristic radius should grow by 1.14 mm, and should continue to grow at that rate until obstructed. Application of the magnetic field can reduce that expansion speed for a time, until other phenomena such as plasma cooling by radiation, magnetic field diffusion into the plasma, or reduction of the magnetic field become significant enough to affect the plasma's development.

The pulsed nature of the MG2 field driver makes this last effect of particular interest. As the plasma expands, it may experience a slight variation in field strength if

the plasma lifetime is of the order of 100 ns or more. Note that in common practice, this small variation is ignored for simplicity when making order-of-magnitude estimates for β . The field's time behavior results in a varying β during the experiment as demonstrated in Figure 5.3, which may allow the plasma to expand slightly as the field relaxes. The 10-capacitor model in Equation (3.14) predicts the field will be 93% of its peak value 300 ns after the peak field occurs; the resulting fall in magnetic pressure is 87% of its peak value ($p_{mag} \propto B^2$). With $nkT \propto R^{-3}$, where R is the radius of the plasma, the plasma number density (n) falls rapidly as the plasma expands, and will reach the $\beta \approx 1$ threshold quickly for the sound speed expected for MBW-1, even with the slight reduction of the magnetic field over the plasma's lifetime. This slight variation is thus not a critical problem with the field source; the field is 90% of the peak or greater for 1.00 μ s, given ideal performance.

In a similar manner, blast wave ram pressure ($P_{ram} = \rho v^2$) can be countered by magnetic pressure if the blast wave material is ionized. This is certainly the case in this experiment, and the field dramatically affects the appearance of the blast wave. Whether the plasma is in the form of an expanding plasma volume or a blast wave, both will be subject to elongation as the field suspends radial expansion.

5.2 Plasma channel

Application of the magnetic field showed a significant change in the topology of the plasma generated by the laser interaction. Before discussing these changes, it will be useful to define the scope of the following discussion. The primary focus will

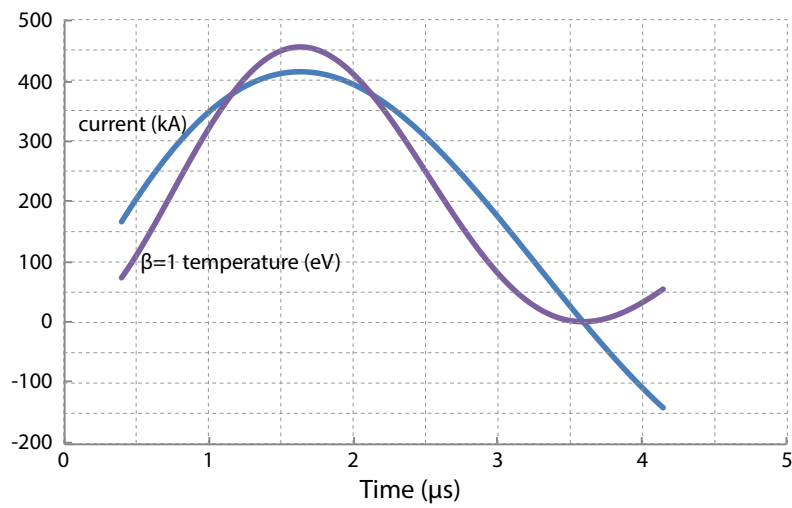


Figure 5.3: A varying discharge produces a varying magnetic pressure, giving a time dependence on the maximum temperature (kT in nkT) for which $\beta = 1$. This temperature is plotted versus time for the 15 T mode in MBW-1. The temperature variation is least near the peak where $di(t)/dt \approx 0$. Density $n = 1.3 \times 10^{18} \text{ cm}^{-3}$.

be the apparent contraction of what should be spherically evolving features, and the interpretation and explanation of the contraction. The perturbations of the blast wave profile are not discussed here, nor is the propagation velocity of the blast wave; these are topics that will be addressed by Nathan Riley (UT-Austin) in a future work. The means of generation of the plasma generation, whether it be by direct laser ionization, ionization by fast electrons launched from the laser focus on the pin, or a combination of these or other phenomena is not rigorously explored, although some discussion arises when interpreting the reason for different plasma structures with and without the field. Figure 5.4 summarizes the features which will be discussed in later sections.

The following discussion will begin by qualitatively assessing the experiment images, acquired by Schlieren photography using a razor blade beam block obstructing the focus, and the lower half of the scattered light. This results in only the upper surfaces of the plasma features being illuminated since the razor blade blocks the light refracted downwardly. When interpreting the images, it is helpful to suppose a topologically similar structure reflected about the image's equator occupies the lower half of the field of view (FOV). Of course, this is nothing more than an extrapolation that may prove helpful in understanding the images. What features actually appear in the lower half of the FOV are likely the result of some upwardly refracted light from a feature at that position. Bearing in mind this imaging limitation, several interesting features are apparent in the set of images acquired during MBW-1, especially when comparing no-field and high-field (> 10 T) shots. The following images have an overlaid crosshair for scale. Each concentric circle has a number attached to it, which indicates its diameter, scaled to match the scale of the image (1 pixel = $12\ \mu\text{m}$).

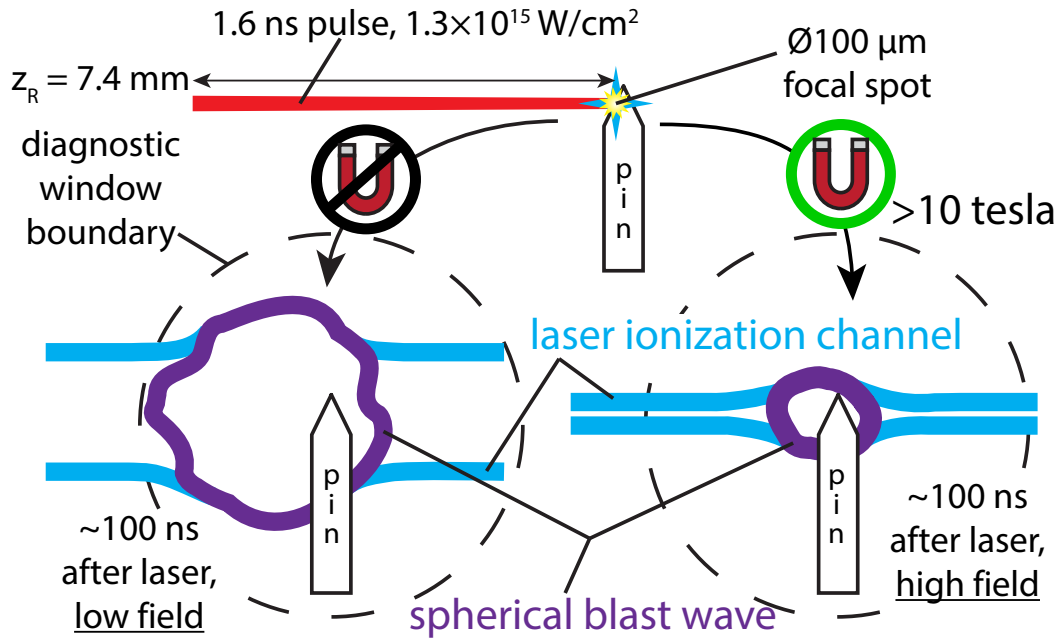


Figure 5.4: Comparison of the no-field and high-field case. The no-field case does not seem to affect the spherical blast wave’s expansion, but the high-field ($> 10 \text{ T}$) case contracts the spherical blast wave and reveals a contracted laser filament. Dashed circle around the pin represents the field-of-view boundary. Note that these features are not always visible in experiment images; and are only meant to be interpretive aides.

Original images (16 bit grayscale, 1648×1236 pixels) have been color-inverted and sharpened to elucidate features. The large circle that borders all the experimental images is caused by light scattering off the edge of the diagnostic window.

Structure observed without field

Without the field, the laser is able to drive what appears to be a blast wave expanding into the 40 Torr xenon background gas, as expected. The best examples of this are Shots 7010, 7014, 7055, and 7070 in Figure 5.5, where dark strips appear due

to significant density gradients at those positions. Shot 7055 is a clear example of the expected blast wave shape, especially imagining a similar structure on the lower half of the FOV. Since the laser strikes the left side of the pin only, it is understandable that the blast wave is not symmetric left to right. Formation of the plasma surface on the pin at the start of irradiation exacerbates this asymmetry. This causes the blast wave to appear to originate from a point upstream of the point of incidence.

Due to the limited number of shots, it is not possible to compute a confident value for a radial expansion rate, but an order-of-magnitude estimate may be 1 mm/100 ns, or 1000 km/s.

Structure observed with low field (≈ 5 tesla)

Shots 7094 and 7100, pictured in Figure 5.6, are the only shots in the low-field mode, but show an interesting effect of thinning the blast wave front. The physical reason for this goes beyond the scope of this work, but this effect is of great interest to those studying blast wave instabilities predicting in these experiment conditions. These images do not show a noticeable difference in blast wave radius, and the sample size is too small to make a definitive conclusion even if they did, but the blast wave certainly appears to be thinner in both images. This effect warrants additional emphasis on the low-field condition in future magnetized blast wave experiments.

These low-field images support the tentative supposition that the blast wave is at least partially composed of ionized matter; a magnetic field would not have an effect on the neutrals within the gas cell (i.e. the xenon background gas and nylon target pin). Of course, blowoff of ionized material is an expected result of laser irradiation of

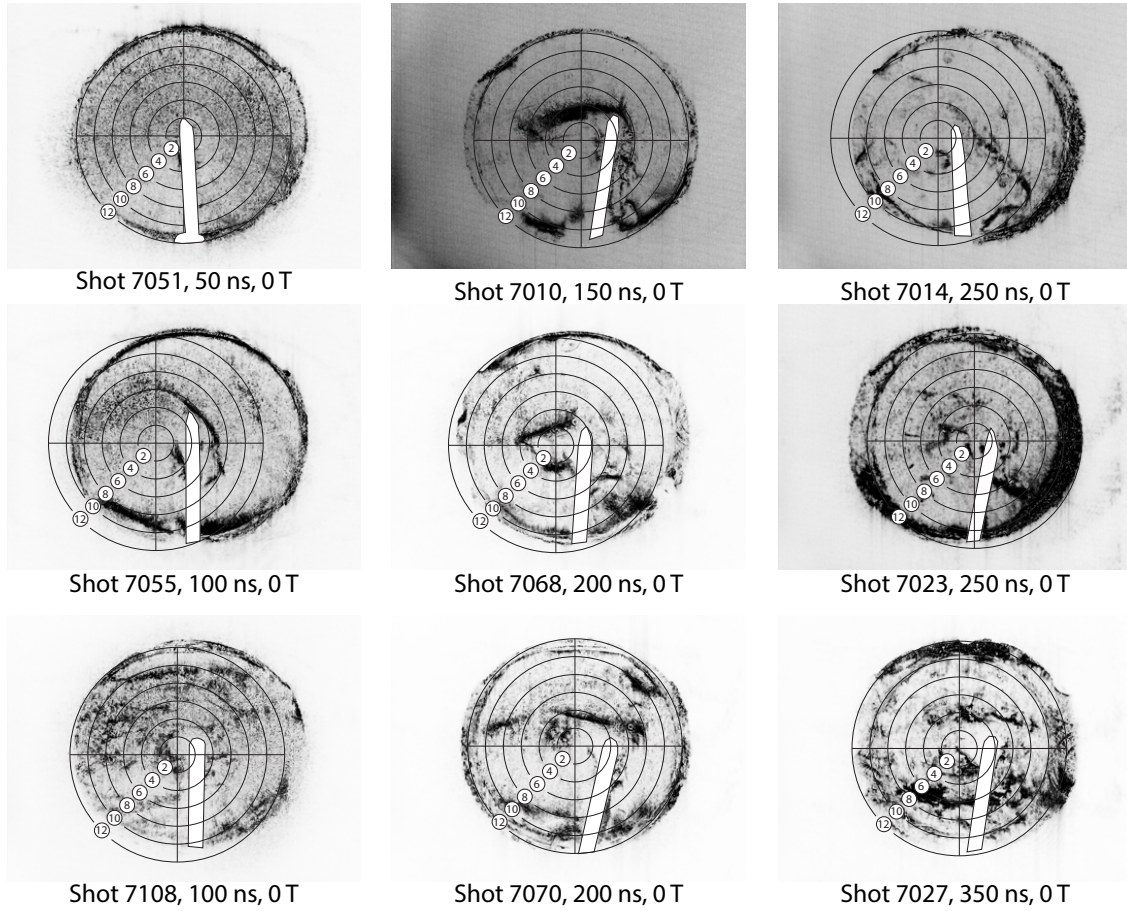


Figure 5.5: All no-field Schlieren images from MBW-1. Delay between laser irradiation and probe beam varied between 50 and 350 ns. Dark lines indicating a sharp density gradient appear in most images. Laser enters from the left; for scale, crosshair circles are labeled with their diameters in millimeters.

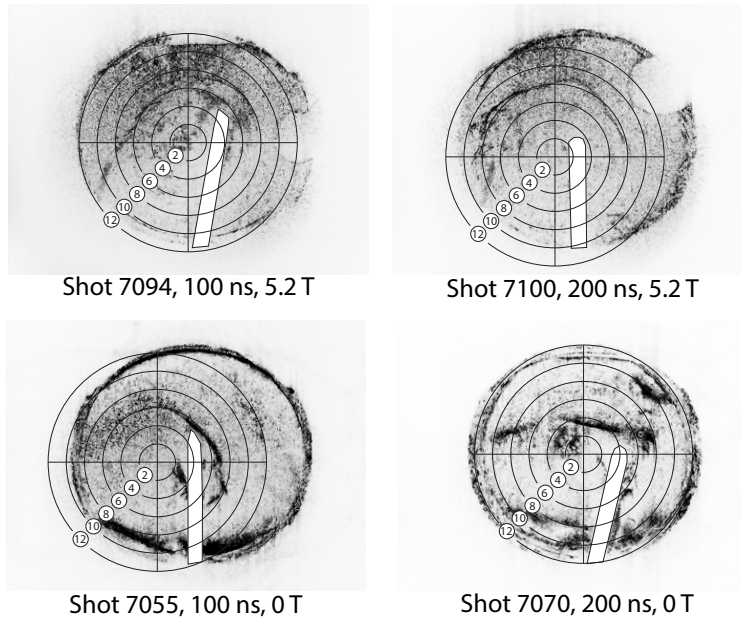


Figure 5.6: All low-field Schlieren images from MBW-1. Dark lines indicate a sharp density gradient. In both shots, these lines appear thinner than those in the no-field case. For comparison, the most similar no-field shots are show below their respective low-field shots. Laser enters from the left; for scale, crosshair circles are labeled with their diameters in millimeters.

a solid target. In the high-field shots, this will be confirmed, as the images show a strong response to the field.

Structure observed with high field (> 10 tesla)

Images of the target region for high-field shots showed a drastic change in structure. Whereas most no-field and low-field shots showed a spherical structure originating in front of the pin, the high-field shots show a cylindrical structure, or filament, nearly in line with the magnetic field axis. Figure 5.7 shows this filament clearly, except in Shot 7102, which may have the upstream portion of the filament blocked by the razor blade beam block. Exceptions to this are Shots 7110, 7112, 7115, and 7117, which are difficult to interpret given the images' ambiguity; Figure 5.8 shows these four images, which show unidentifiable or inexplicable features.

In addition to the filamentary structure along the horizontal direction, a bubble-like feature surrounds the pin, and accompanies the filament structure in the high-field shots pictured in Figure 5.7. A dark band surrounding the pin defines the border of this bubble, highlighted in Figure 5.10. Although such a bubble structure appears in no-field shots like Shots 7027 and 7068, it is not as consistent of an occurrence as in the high-field case, and this implies an enhancement of the bubble structure with high field.

Figure 5.9 illustrates features at key times in a high-field shot. The laser pulse initially generates a plasma in the $100\ \mu\text{m}$ focal region, and later expands. The expansion slows at later times; most expansion occurs in the first 100 ns. The field has the apparent effect of suppressing the spherical blast wave to a small volume around

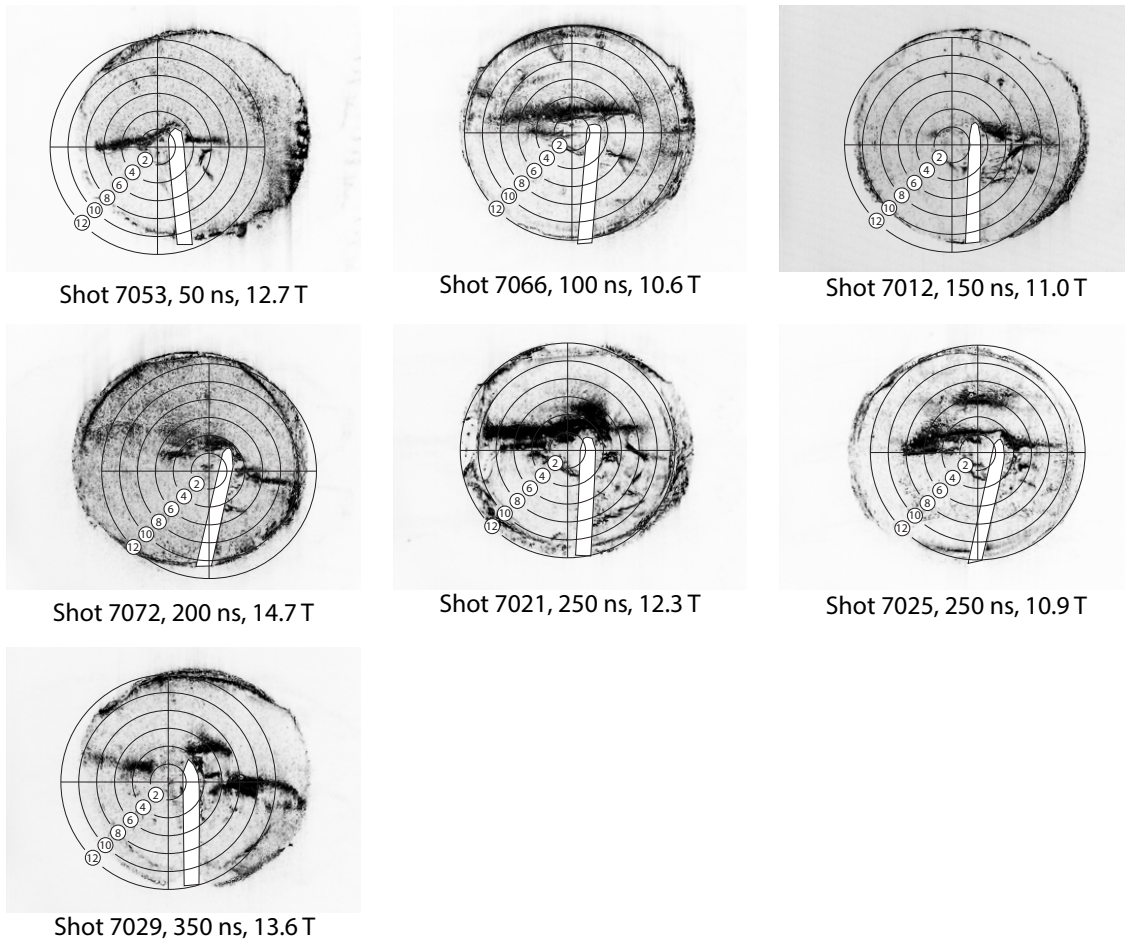


Figure 5.7: Selected high-field Schlieren images from MBW-1. Dark lines indicate a sharp density gradient. Filamentary structure is in stark contrast to quasi-spherical structure in no-field and low-field shots. Also note the bubble-like structure surrounding the pin. Laser enters from the left; for scale, crosshair circles are labeled with their diameters in millimeters.

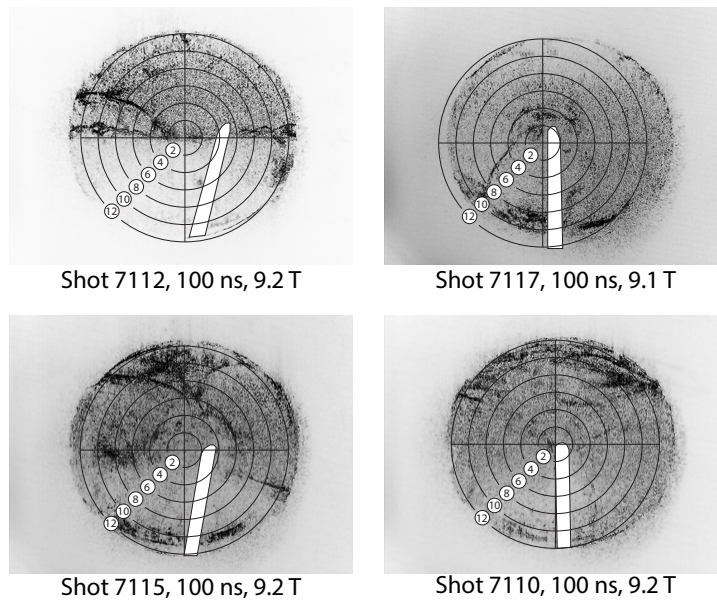


Figure 5.8: Selected high-field Schlieren images from MBW-1 with unidentifiable or inexplicable features are shown for completeness. Laser enters from the left; for scale, crosshair circles are labeled with their diameters in millimeters.

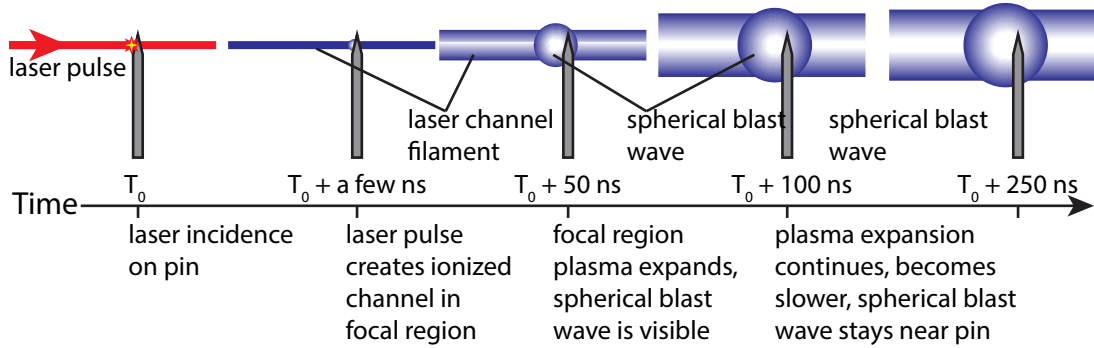


Figure 5.9: Time evolution of the laser filament seen in high-field shots. Initial plasma should only be in the focal region, but can expand at later times. The first two figures do not have comparable experimental images. Images from Shots 7053, 7066, and 7021 in Figure 5.7 are respectively comparable to the cartoon images for $T_0 + 50$ ns, 100 ns, and 250 ns.

the pin. There are no diagnostic images earlier than 50 ns after laser arrival, therefore this fast initial expansion cannot be confirmed experimentally, although it must occur while $t < (T_0 + 50$ ns) since the filament diameter in the image from Shot 7053 in Figure 5.7 is measurably larger than 100 μm .

5.3 Interpretation of plasma channel

Directing attention toward the high-field situation, in which this plasma filament appears across the laser axis, an argument can be made to explain the cause of this filament. Shot images clearly show that the high field ($B > 10$ T) is central to its appearance. This discussion will begin with a description of the likely mechanism of the initial formation of the plasma, which is quite straightforward. The more interesting point of this section is the question of why the filament only appears in the

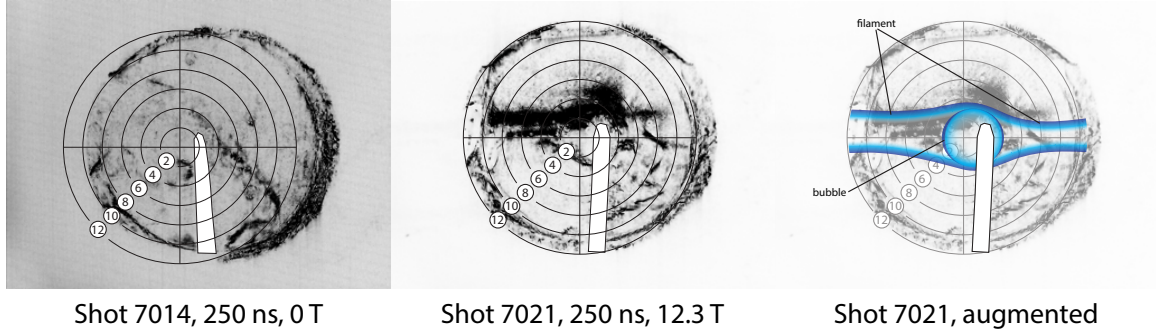


Figure 5.10: High-field shots yield new structures around the target pin. Left: Shot 7014 provides comparison with the no-field case at the same probe beam delay. Center: original image for Shot 7021, filament and bubble structures are clearly visible. Right: a cartoon superimposed on Shot 7021’s image highlights the two structures under discussion. Laser enters from the left; for scale, crosshair circles are labeled with their diameters in millimeters.

high-field shots. Furthermore, are there general descriptions of the plasma transport that can explain the observed behavior? This will be mostly a qualitative analysis; any numerical arguments should be tempered with the understanding that the data variance is large, and cannot lead to precise measurements. Even still, there are several observable features that reveal the general conditions of the plasma.

5.3.1 Plasma creation mechanism

Appearance of the filament in the high-field shots immediately suggest a plasma is present. This filament plasma is not visible in the no-field and low-field shots, but the presence of the blast wave may obscure it. Shots 7051 shows there is no filament plasma whatsoever in the no-field case, but Shot 7053 shows stark evidence of a filament plasma. Both shots used a $T_0 + 50$ ns diagnostic delay. In fact, Shot 7051

does not even show a blast wave from the pin yet, even though it was confirmed the pin was irradiated as designed. This disqualifies the blast wave from being a candidate for explaining the filament plasma generation.

Another possible formation mechanism is a magnetically collimated beam of hot electrons emanating from the irradiated pin. However, this explanation must include the chance for electron-neutral collisions to cause cross-field electron transport. A series of such collisions would decollimate the electron jet, resulting in a plasma with some angular divergence. While Shots 7029 and 7072 may show hints of such a divergence, this is an exception rather than a trend. Furthermore, if the electrons from the pin were released with high energy, which is not an unreasonable expectation from a laser-solid interaction, the electron collisional ionization cross section may be quite low; the cross-section for this process peaks around electron energies of 200 eV [49].

The most likely explanation for initial filament plasma formation is direct ionization by the electric field of the TPW laser pulse. Even with the long-pulse duration of 1.6 ns, the average energy of 160 J yields 1.3×10^{15} W/cm² on a focal diameter of 100 μ m. Such a high intensity places the ionization regime in the tunneling regime, as opposed to the multiphoton regime. This is known by obtaining the Keldysh parameter, which is a comparison of ionization potential I_p to the ponderomotive potential U_p :

$$U_p = \frac{e^2 E_0^2}{4m_e \omega_0^2}. \quad (5.2)$$

The dimensionless Keldysh parameter is

$$\gamma_K = \sqrt{\frac{I_p}{2U_p}}, \quad (5.3)$$

and $\gamma_K < 1$ marks the regime where tunneling ionization overtakes multiphoton ionization as the dominant ionization process [12].

It should be noted that the tunneling ionization regime is valid for high intensities, which are not present in the rising and falling edge of the laser pulse. As the intensity ramps up to its peak, the Keldysh parameter will be less than unity, signaling the multiphoton ionization regime. The author cautions that the following discussion, which only considers the tunnel ionization regime, is only correct under the simplifying assumption of a laser pulse with a square temporal profile. A more rigorous treatment must consider the initial multiphoton ionization phase, followed by a tunneling ionization phase. Since this discussion is only meant to provide a *qualitative* picture of the plasma formation, the following explanation will simplify the physical picture by assuming a square temporal profile; the laser will generate a plasma whether this approximation is considered or not.

Tunnel ionization

Tunnel ionization is an ionization process that is a partially classical and partially quantum mechanical process. The laser's electric field classically deforms the potential barrier that binds an electron to the atom; a sufficiently strong electric field deforms the potential barrier so drastically that the electron can escape the atom's potential barrier altogether by quantum mechanically tunneling out of the barrier, schematically depicted Figure 5.11 [12]. As the laser's electric $E(t)$ approaches the characteristic atomic field $E_a = 5.14 \times 10^9$ V/cm, this process becomes increasingly significant. The ionization rate for this process for a single hydrogen-like atom [33] is

given in

$$W_{H-like} = 4\omega_a \left(\frac{I_p}{I_H} \right)^{5/2} \frac{E_a}{E(t)} \exp \left[-\frac{2}{3} \left(\frac{I_p}{I_H} \right)^{3/2} \frac{E_a}{E(t)} \right]. \quad (5.4)$$

The constants $E_a = 5.14 \times 10^9$ V/cm and $\omega_a = 4.13 \times 10^{16}$ s⁻¹ are characteristic atomic values for electric field and frequency. The other constants are ionization energies, $I_H = 13.6$ eV is the ionization energy of hydrogen, and I_p is the ionization energy of the material being ionized. The laser's electric field is expressed as a simple sinusoidal oscillation at the laser frequency,

$$E(t) = E_0 \sin(2\pi ct/\lambda), \quad (5.5)$$

where the laser's electric field in terms of intensity is

$$E_0 = \sqrt{\frac{2I_0}{\epsilon_0 cn}}, \quad (5.6)$$

with I_0 and n representing the laser's peak intensity and the medium's refractive index, respectively.

This discussion would be incomplete without listing the ADK ionization rate, a more rigorous expression for the same rate. The ADK solution, shown in Equation (5.7), takes the electron quantum numbers into consideration, and treats the ionization process in a manner that results in a more realistic picture.

$$W_{ADK} = \omega_a C_{nl} f(l, m) \frac{3^{1/2}}{2\pi^{1/2}} \left(\frac{I_p}{I_H} \right)^{1/4} \left(\frac{E_0}{E_a} \right)^{1/2} \times \left[2 \frac{E_a}{E_0} \left(\frac{I_p}{I_H} \right)^{3/2} \right]^{2n-|m|-1} \exp \left[-\frac{2}{3} \left(\frac{I_p}{I_H} \right)^{3/2} \frac{E_a}{E_0} \right] \quad (5.7)$$

$$C_{nl} = (2 \exp(1) / n)^n (2\pi n)^{-1/2} \quad (5.8)$$

$$f(l, m) = \frac{(2l+1)(l+|m|)!}{2^{|m|}(|m|)!(l-|m|)!} \quad (5.9)$$

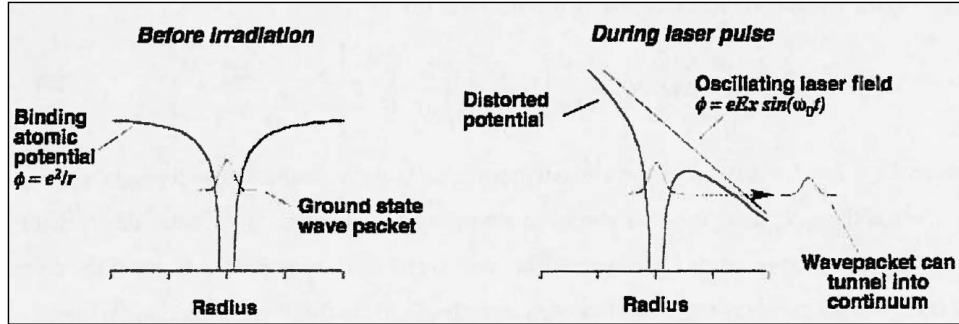


Figure 5.11: Ordinarily, an atom’s potential well contains its electrons. In the presence of strong electric field, this potential well is distorted, which creates an opportunity for the electron to escape by tunneling, a quantum mechanical effect [12].

ionization level	Xe ¹⁺	Xe ²⁺	Xe ³⁺	Xe ⁴⁺	Xe ⁵⁺
I_p (eV)	12.1	21.0	32.1	46	57
γ_K	0.21	0.28	0.34	0.41	0.46

Table 5.1: Keldysh parameter for the first five ionizations of xenon.

This rate is the ionization rate for an entire laser cycle, and does not need to be integrated as does the W_{H-like} expression. The additional coefficients l , m , and n are the quantum numbers of the ionized electron [2].

Ionization in plasma channel

Using the experimental values of $I_0 = 1.3 \times 10^{15}$ W/cm² and $\lambda = 1057$ nm, the ponderomotive energy is 136 eV. The Keldysh parameters for the first five ionization levels of xenon are listed in Figure 5.11, and all are below unity. By Equation (5.6), the laser’s electric field is 9.9×10^8 V/cm, which is the final unknown parameter of Equation (5.4) which enables a calculation of the ionization rate for xenon in the

laser's electric field. Figure 5.12 illustrates the ionization rates as a function of time across one laser cycle. It is significant that the ionization rate plots narrow with increasing ionization state; at higher ionization states, the electrons only tunnel when the laser field is close to its peak. This has an effect on the energy distribution of the freed electrons, in that the laser field gives an electron some energy which is a function of the phase at which the electron was freed. This energy is called the after threshold ionization (ATI) energy, and is given by

$$KE_{ATI} = 2U_p \sin^2 \Delta\phi_0, \quad (5.10)$$

where $\Delta\phi_0$ is the phase difference between the phase at which the electron is “born” and the phase of the peak electric field [12]. Combining this with Equation (5.4) yields a distribution function in terms of electron energy ϵ :

$$f(\epsilon) = \frac{a}{(1 - \epsilon/2U_p)(\epsilon/2U_p)^{1/2}} \exp \left[-\frac{2}{3} \left(\frac{I_p}{I_H} \right)^{3/2} \left(\frac{E_a}{E_0} \right) \left(1 - \frac{\epsilon}{2U_p} \right)^{-1/2} \right]. \quad (5.11)$$

A simple W_{H-like} model will be sufficient for the discussion here, since the nuances afforded by the superior ADK ionization rate will be lost in the approximations inherent to this discussion. Integrating the W_{H-like} ionization rates over one laser cycle shows the xenon atoms should be ionized to at least Xe^{5+} , creating a plasma along the laser focal region.

5.3.2 Plasma filament in no-field shots

A plasma filament comparable to that seen in the high field shots of Figure 5.7 is not visible in the no-field shots of Figure 5.5. In most cases, the blast wave is

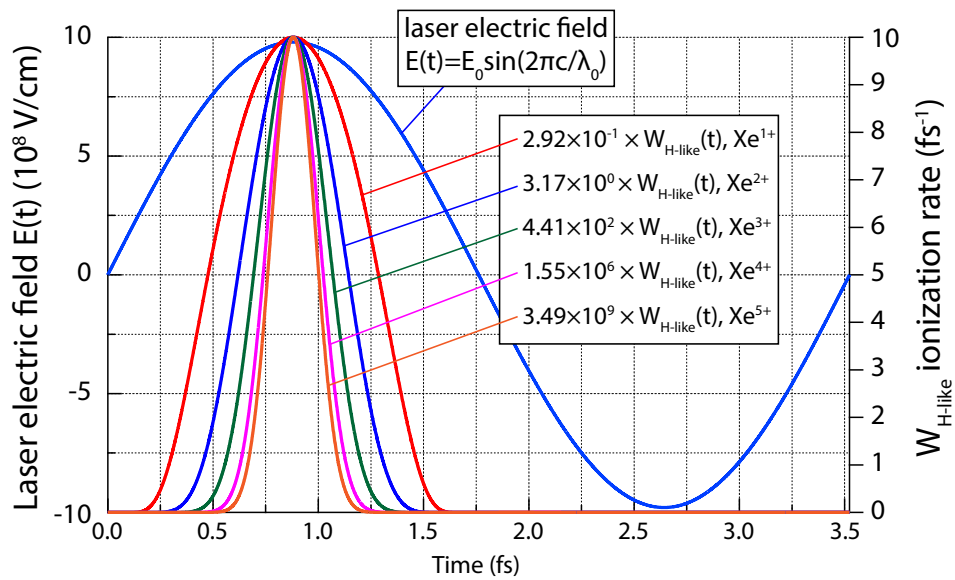


Figure 5.12: Ionization rates for xenon across one laser cycle using values from Figure 5.11 in Equation (5.4). Rates are normalized to 10^{16} s^{-1} , with their scale factors listed in the plot callouts.

the dominant feature in the no-field shots, and fills the region where the filament appears in the high-field shots. Any filament that would ordinarily be visible is thereby obscured. Shot 7051 is an exception, where the diagnostic probe has arrived too early for the blast wave to propagate into the background gas; no filament is visible in this case either.

This lends credence to the possibility that the filament has expanded rapidly enough to be beyond the boundary of the diagnostic window. This statement is equivalent to saying that any laser-generated filament produced expanded to $R \geq 5$ mm within 50 ns. An alternate explanation is that the Schlieren imaging diagnostic, which has a threshold density gradient below which nothing is detected, may not detect the density gradient of a filament produced in the no-field case. That is, although the Schlieren imaging is sensitive to sharp changes in refractive index (e.g. a plasma), there is a limit to the minimum detectable change. When the laser channel expands unrestricted in the no-field case, the change in the refractive index may not be sharp enough to scatter a measurable amount of probe light. With a more sensitive Schlieren diagnostic, these subtle features could become visible even in no-field shots.

Regardless of the explanation, it is clear that any laser-produced filament, which may or may not appear without field, cannot be seen in this configuration. The filament readily appears with high field, perhaps since the expansion of the spherical blast wave from the pin is suppressed by the field, uncovering the laser-produced filament. In addition, the field should suppress the growth of the laser filament, making it visible to the diagnostics by keeping it within the FOV.

5.3.3 Plasma filament in high-field shots

Let the discussion now shift to considering the high-field filament. The prime question asks why the high-field shots look so different compared to no-field ones. As alluded to in the previous section, the suppression of the spherical blast wave's growth may help reveal the filament, which can also be suppressed and thus more visible due to the larger density gradient.

Mechanism of filament appearance

Initially, when the laser creates a plasma in its focal region, the electrons attain some energy distribution, which may proceed to equilibrate on some time scale associated with the collision time of the filament plasma. Under a circumstance with no field, the only restriction to the filament's expansion would be that caused by the background gas. In the high-field case, the plasma is magnetized, and the electrons and ions have further restrictions on their movements.

Charged particles like these in magnetic fields orbit the field lines, and the radius of this orbit is the Larmor radius (also called the gyroradius), given by

$$\rho_L = \frac{\sqrt{mkT}}{qB} \quad (5.12)$$

for a particle with mass m , charge q , and energy kT in a magnetic field of flux density B . Without collisions, a particle orbiting a field line is unable to progress radially, although it is free to travel along the direction of the field line. For simplicity, this ignores the $\text{grad-}B$ drift, in which a particle executing a Larmor orbit is exposed to differing magnetic field strengths in different regions of its orbit, resulting in a drift

across field lines. The justification for ignoring grad- B is the fact that the Larmor radius in MBW-1 conditions is considerably smaller than the length scale of the gradient of the magnetic field, making grad- B drift relatively insignificant.

Considering the electrons in MBW-1, recall the statement in Section 5.3.1 that the greatest energy obtainable from tunnel ionization is $2U_p$, which will be 272 eV in this case. In a magnetic field of 10 tesla, this gives a maximum electron gyroradius of 3.9 μm . The field coil is several orders of magnitude larger than this, and in the localized region of a gyroradius, ∇B is small.

It can be concluded from this argument that the electrons are “stuck” to their field lines, and never propagate from their original radial positions in the case of high field. However, the experimental images do not support this assertion, since the plasma appears to be 1 mm in diameter in Shot 7053, and expands to greater radii in later shots, pictured in Figure 5.13. This raises a question as to the cause of this expansion, which is likely cross-field diffusion due to collisions.

Diffusion across field lines

Diffusion across field lines is a process by which charged particles are able to circumvent the Larmor orbit restriction on particle travel. From this point forward, we will be specifically discussing electron diffusion. The key to cross-field diffusion (denoted with a subscript \perp), is collisions—the collisions can “knock” the electrons from their original orbiting trajectory to different one. The rate of such collisions is dependent on the energy and number density of the electrons, specifically

$$\tau_e = \frac{3\sqrt{m_e} (kT_e)^{3/2}}{4\sqrt{2\pi} n \lambda e^4} = 3.44 \times 10^5 \frac{T_e^{3/2} [\text{eV}]}{n [\text{cm}^{-3}] \lambda} \text{sec}, \quad (5.13)$$

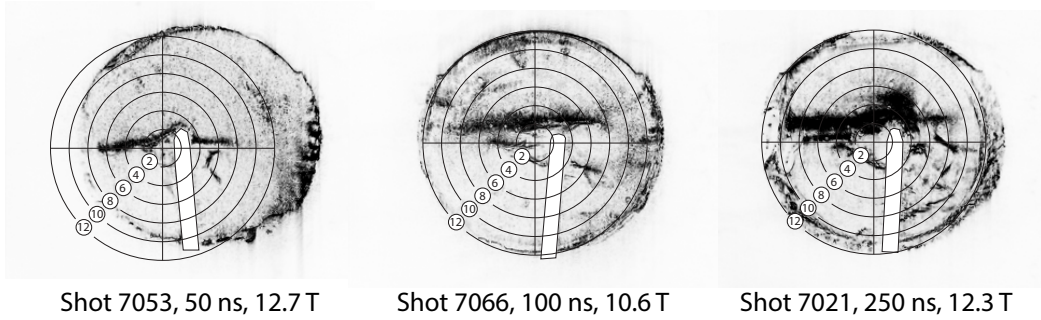


Figure 5.13: An expansion of the plasma filament is visible as probe delay increases. From left to right, plasma filament radius is approximately 1 mm, 1.3 mm, and 1.5 mm. Due to the Schlieren imaging apparatus using a half-beam block and illuminating only the top surface of the filament, symmetry about the horizontal axis is assumed for measurement purposes. This symmetry-breaking effect is discussed in Section 4.2.5.

with λ being the Coulomb logarithm, given by

$$\lambda_{ee} = 23.5 - \ln(n_e^{1/2} T_e^{-5/4}) - [10^{-5} + (\ln T_e - 2)^2 / 16]^{1/2} \quad (5.14)$$

for electron-electron collisions [31]. It should be noted that Equation (5.13) assumes a plasma charge state of unity, which is not accurate in this case. Despite this inaccuracy, this should still give an order-of-magnitude estimate for collision time. To accommodate charge states other than unity, we impose the condition that $n = n_e$.

Ignoring ion collisions, cross-field electron velocity in a magnetized plasma is

$$\mathbf{v}_\perp = \pm \mu_\perp \mathbf{E} - D_\perp \frac{\nabla n_e}{n_e} + \frac{\mathbf{v}_E + \mathbf{v}_D}{1 + (\nu_e^2 / \omega_{ce}^2)}, \quad (5.15)$$

where the electron gyrofrequency $\omega_{ce} = eB/m_e$, and ν_e is the electron-electron collision frequency, such that $\nu_e = \tau_e^{-1}$. The middle term represents cross-field diffusion, with a coefficient

$$D_\perp = \frac{kT_e / (m_e \nu_e)}{1 + \omega_{ce}^2 \tau^2} \quad (5.16)$$

in front of the density gradient $\nabla n_e/n_e$ [8]. The first term represents the particle mobility, with

$$\mu_{\perp} = \frac{q/(m\nu)}{1 + \omega_{ce}^2 \tau^2}, \quad (5.17)$$

which is essentially the particle's response to the electric field from the plasma, and the final term accounts for particle drifts.

The product $D_{\perp} \cdot (\nabla n_e/n_e)$ is of particular interest, since this is the term that can explain the high-field plasma filament's expansion due to cross-field diffusion. At first, when the laser ionizes the background gas, $\nabla n_e/n_e$ is very large at the plasma boundary. This drives a rapid initial expansion, which is governed by the coefficient D_{\perp} . As the initially sharp plasma boundary relaxes into a smoother profile, the gradient term becomes less influential, and its diffusive effect should fall rapidly.

Although it is not visible in the no-field shots, if a cylindrical blast wave launches from the laser focal region when this plasma is created, the ram pressure may expand the plasma initially. If the ram pressure $p_{ram} = \rho v^2$ exceeds the plasma pressure $p = nkT$, the ordinary concept of plasma β may not apply, and the blast wave could initially be unconfined. Unfortunately, there is insufficient experimental data to bring this hypothesis beyond the realm of conjecture.

5.3.4 Summary of plasma behavior

The arguments posed here concerning the filament's expansion behavior are order-of-magnitude explanations for the phenomena in play within the plasma volume during its recorded lifetime of a few hundred nanoseconds. These phenomena, such

as tunnel ionization and cross-field diffusion, are effects that can be expected in this regime of gas-density plasma irradiated by a high-intensity pulsed laser. Additional effects of the blast wave from the pin are not in discussion here; this is a separate portion of the experiment, and should be considered in a separate work.

It is not unreasonable to expect that additional phenomena are in play; in fact, it is likely that this is the case. Even still, the filamentary structure observed is undoubtedly brought about by the high field, and a Larmor radius restriction of the electrons' radial travel is a good qualitative explanation for the scaling seen. The field strength threshold at which the filament dominates the picture is not a well-posed question for the data set, but the low-field shots pictured in Figure 5.6 hint that this could be between 5 and 10 tesla.

Chapter 6

Conclusion

6.1 Summary

In response to the rapidly growing field of high energy density (HED) physics, Sandia National Laboratories and The University of Texas at Austin developed the MegaGauss 2 (MG2) pulse magnetic field driver to provide magnetization capability to HED plasma experiments. Magnetizing HED plasmas requires magnetic fields of the order of 100 T to reach the point where the magnetic field can strongly influence plasma behavior. The estimated peak discharge current of the MG2 system is 2.2 MA from a 100 kV charge voltage on the 160 kJ capacitor bank. During experiments at UT-Austin, we operated the system at 50 kV, which consistently yielded 1.0 MA, depending on circuit loading conditions. The load for most shots were single-turn coils. Faraday measurement of the field in the coil center indicated 63 T for a 1.0 MA peak current, which approximately agreed with simplified Biot-Savart estimates.

After the initial test-of-operation phase once the system arrived at UT-Austin from SNL, it became apparent that some modification to the original system would help prevent electrical breakdown during vacuum operation and increase reliability, which was crucial for future experiments. Reducing the size of the vacuum vessel was the primary modification; this modification allowed most of the high-voltage,

high-current conical transmission line to operate in atmosphere instead of vacuum. This effectively reduced the area of the high-voltage surfaces in vacuum, and increased the reliability of vacuum shots.

This modification secured the possibility of operating MG2 on the Texas Petawatt (TPW) Laser. In August 2013, the Magnetized Blast Waves experiment #1 (MBW-1) explored the effect of a strong magnetic field on a blast wave generated by irradiating a nylon pin immersed in low-pressure xenon. In addition to the spherical blast wave, a second, filamentary plasma appeared only during shots with 10 tesla or more.

It is discussed in Chapter 5 that this filament is generated by the laser's interaction with the background xenon gas. The appearance of the filament for the $B > 10$ T condition is the combined result of 1) the suppression of the spherical blast wave that obscured any filamentary structure in no-field or low-field shots, 2) the restricted expansion of the filamentary plasma due to the magnetic pressure, and possibly 3) the field's effective sharpening of the filamentary plasma's boundary which made the boundary more visible to the Schlieren imaging diagnostic, which is sensitive to sharp density perturbations.

The result of the MBW-1 experiment shows that the high (> 10 T) magnetic field had a drastic effect on plasma evolution versus the no-field and low-field (≈ 5 T) case. This confinement effect is relevant to expanding plasmas such as laser-heated gas targets in a background magnetic field. However, confining a laser-produced plasma, which can exhibit relatively large plasma pressures, demands a similarly large magnetic pressure. This is the function of the MG2 pulsed magnetic field driver.

To conclude, this experiment has demonstrated the capability of the MG2 system in a high-strength magnetic field experiment by producing up to 15 T field with ease in the MBW-1 experiment. Thoughtful selection and designing of targets should permit further use in other experiments requiring high magnetic fields, since Faraday rotation measurements have confirmed up to 63 T from this system when operated with 45% of the maximum designed current of 2.2 MA.

6.2 Future work

To push beyond the practical limitation of a 50 kV charge on the capacitor bank, improving the insulation scheme for the triplate transmission line may be in order. An attempt to fire the MG2 system with an 80 kV capacitor charge in the ten-capacitor mode resulted in catastrophic damage to the solid insulators which were installed after a series of modifications at UT-Austin. Due to the setback caused by this event, the operational limit of the capacitor bank charge voltage was set to to 50 kV when using all ten capacitors. An upgrade allowing higher charge would potentially double the maximum discharge current, and would have a similar multiplicative effect on the maximum attainable magnetic field.

Reconfiguring the load into a smaller coil would also strengthen the magnetic field, although the volume within the coil bore would diminish. In some cases, this could be an acceptable trade-off. Enlarging the coil is possible, although the coils in the gas cell targets of the MBW-1 experiment pushed the limit of best practices. Since the access ports on the MG2 vacuum chamber are meant to be concentric with

the coil, enlarging the coil beyond that of the coils in MBW-1 would push the coil boundary dangerously close to the top of the triplate transmission line. The best approach for larger coils is to modify the vacuum chamber to raise the access ports. Other loads such as wire arrays, cylindrical liners, gas puffs, or other such devices could be possible, although such purposes are beyond the scope of this work.

At the time of publication of this work, the MG2 system will be at SNL for implementation in additional blast wave experiments exploring effects identical or comparable to those observed during MBW-1. Due to the very different beam line configuration of the Z Beamlet laser, where MG2 will be deployed, the triplate transmission line will have to be replaced with a coaxial stalk feed, similar to the MIFEDS apparatus of [24]. The mobility and modularity of the MG2 components are key in enabling this endeavor.

List of Acronyms

2-D two-dimensional.

A-K anode-cathode.

AR anti-reflective.

ATI after threshold ionization.

CAD computer-aided design.

CPA chirped pulse amplification.

CW continuous wave.

DC direct current.

FOV field of view.

FWHM full width half maximum.

GHOST Glass Hybrid OPCPA Scale Test.

HED high energy density.

ICF inertial confinement fusion.

ID inner diameter.

LANL Los Alamos National Laboratory.

LLE Laboratory for Laser Energetics.

MagLIF magnetized liner inertial fusion.

MBW-1 Magnetized Blast Waves experiment #1.

MG1 MegaGauss.

MG2 MegaGauss 2.

MHD magnetohydrodynamic.

MIFEDS Magneto-Inertial Fusion Electrical Discharge System.

NHMFL National High Magnetic Field Laboratory.

NRL Naval Research Laboratory.

OD outer diameter.

RF radio frequency.

SNL Sandia National Laboratories.

TA-1 Target Area 1.

TA-2 Target Area 2.

TGG terbium gallium garnet.

TPW Texas Petawatt.

UT-Austin The University of Texas at Austin.

UV ultraviolet.

Bibliography

- [1] Texas petawatt laser. <http://texaspetawatt.ph.utexas.edu/>. Accessed: 2014-01-22.
- [2] Maxim V Ammosov, Nikolai B Delone, and Vladimir P Krainov. Tunnel ionization of complex atoms and atomic ions in electromagnetic field. In *1986 Quebec Symposium*, pages 138–141. International Society for Optics and Photonics, 1986.
- [3] W. Bang, G. Dyer, H. J. Quevedo, A. C. Bernstein, E. Gaul, M. Donovan, and T. Ditmire. Optimization of the neutron yield in fusion plasmas produced by coulomb explosions of deuterium clusters irradiated by a petawatt laser. *Phys. Rev. E*, 87:023106, Feb 2013.
- [4] Hansjoachim Bluhm. *Pulsed power systems principles and applications*. Springer, Berlin, 2006.
- [5] B.N. Breizman and A.V. Arefiev. Electron response in laser-irradiated microclusters. *Plasma Physics Reports*, 29(7):593–597, 2003.
- [6] Boris N. Breizman and Alexey V. Arefiev. Ion acceleration by hot electrons in microclusters. *Physics of Plasmas (1994-present)*, 14(7):–, 2007.

- [7] Harold L. Brode. Numerical solutions of spherical blast waves. *Journal of Applied Physics*, 26(6), 1955.
- [8] Francis Chen. *Introduction to plasma physics and controlled fusion*. Plenum Press, New York, 1984.
- [9] National Research Council Committee on High Energy Density Plasma Physics, Plasma Science Committee. *Frontiers in High Energy Density Physics: The X-Games of Contemporary Science*. The National Academies Press, 2003.
- [10] Wikimedia Commons. File:paschen curves.png, July 2009.
- [11] M.E. Cuneo, M. C. Herrmann, D. B. Sinars, S. A. Slutz, W. A. Stygar, R. A. Vesey, A. B. Sefkow, G. A. Rochau, G. A. Chandler, J. E. Bailey, J. L. Porter, R. D. McBride, D. C. Rovang, M. G. Mazarakis, E. P. Yu, D. C. Lamppa, K. J. Peterson, C. Nakhleh, S. B. Hansen, A. J. Lopez, M. E. Savage, C. A. Jennings, M. R. Martin, R. W. Lemke, B. W. Atherton, I. C. Smith, P. K. Rambo, M. Jones, M. R. Lopez, P. J. Christenson, M. A. Sweeney, B. Jones, L. A. McPherson, E. Harding, M. R. Gomez, P. F. Knapp, T. J. Awe, R. J. Leeper, C. L. Ruiz, G. W. Cooper, K. D. Hahn, J. McKenney, A. C. Owen, G. R. McKee, G. T. Leifeste, D. J. Ampleford, E. M. Waisman, A. Harvey-Thompson, R. J. Kaye, M. H. Hess, S. E. Rosenthal, and M. K. Matzen. Magnetically driven implosions for inertial confinement fusion at sandia national laboratories. *Plasma Science, IEEE Transactions on*, 40(12):3222–3245, 2012.
- [12] T. Ditmire and M. Bass. *Handbook of optics*, volume 4. McGraw-Hill, New York, 2010.

- [13] T. Ditmire, J.W.G. Tisch, E. Springate, M.B. Mason, N. Hay, J.P. Marangos, and M.H.R. Hutchinson. Explosion of atomic clusters heated by high intensity, femtosecond laser pulses. In Louis DiMauro, Margaret Murnane, and Anne LHuillier, editors, *Applications of High-Field and Short Wavelength Sources*, pages 123–130. Springer US, 1998.
- [14] T. Ditmire, J. Zweiback, V. P. Yanovsky, T. E. Cowan, G. Hays, and K. B. Wharton. Nuclear fusion from explosions of femtosecond laser-heated deuterium clusters. *Nature*, 398:489–492, April 1999.
- [15] A. D. Edens. Experimental study of the hydrodynamics of high mach number blast waves. Technical report, The University of Texas at Austin.
- [16] M Erba. New parametrizations of dd fusion cross sections. *Journal of Physics D: Applied Physics*, 27(9):1874, 1994.
- [17] R. E. Falcon, G. A. Rochau, J. E. Bailey, J. L. Ellis, A. L. Carlson, T. A. Gomez, M. H. Montgomery, D. E. Winget, E. Y. Chen, M. R. Gomez, T. J. Nash, and T. M. Pille. Creating White Dwarf Photospheres in the Laboratory: Strategy for Astrophysics Applications. In Krzesiń, J. ski, G. Stachowski, P. Moskalik, and K. Bajan, editors, *18th European White Dwarf Workshop.*, volume 469 of *Astronomical Society of the Pacific Conference Series*, page 405, January 2013.
- [18] Ross E. Falcon, G.A. Rochau, J.E. Bailey, J.L. Ellis, A.L. Carlson, T.A. Gomez, M.H. Montgomery, D.E. Winget, E.Y. Chen, M.R. Gomez, and T.J. Nash. An experimental platform for creating white dwarf photospheres in the laboratory. *High Energy Density Physics*, 9(1):82 – 90, 2013.

- [19] S. H. Feldman, G. Hays, A. Belolipetski, D. Herrmann, J. Schmidt, H. J. Quevedo, A.C. Bernstein, and T. Ditmire. Glass hybrid opcpa scale test bed laser. In *Lasers and Electro-Optics, 2009 and 2009 Conference on Quantum electronics and Laser Science Conference. CLEO/QELS 2009. Conference on*, pages 1–2, 2009.
- [20] M. E. Foord, Y. Maron, G. Davara, L. Gregorian, and A. Fisher. Particle velocity distributions and ionization processes in a gas-puff z pinch. *Phys. Rev. Lett.*, 72:3827–3830, Jun 1994.
- [21] Erhard W. Gaul, Mikael Martinez, Joel Blakeney, Axel Jochmann, Martin Ringuette, Doug Hammond, Ted Borger, Ramiro Escamilla, Skylar Douglas, Watson Henderson, Gilliss Dyer, Alvin Erlandson, Rick Cross, John Caird, Christopher Ebbbers, and Todd Ditmire. Demonstration of a 1.1 petawatt laser based on a hybrid optical parametric chirped pulse amplification/mixed nd:glass amplifier. *Appl. Opt.*, 49(9):1676–1681, Mar 2010.
- [22] P Gibbon and E Frster. Short-pulse laser - plasma interactions. *Plasma Physics and Controlled Fusion*, 38(6):769, 1996.
- [23] Steven Glidden and Howard Sanders. Cobra high current generator baseline design. Technical report, Applied Pulsed Power, Inc., prepared for Cornell University.
- [24] O. V. Gotchev, J. P. Knauer, P. Y. Chang, N. W. Jang, M. J. Shoup, D. D. Meyerhofer, and R. Betti. Seeding magnetic fields for laser-driven flux compression in high-energy-density plasmas. *Review of Scientific Instruments*, 80(4):–, 2009.

- [25] O. F. Hagena and W. Obert. Cluster formation in expanding supersonic jets: Effect of pressure, temperature, nozzle size, and test gas. *The Journal of Chemical Physics*, 56(5), 1972.
- [26] O.F. Hagena. Condensation in free jets: Comparison of rare gases and metals. *Zeitschrift fr Physik D Atoms, Molecules and Clusters*, 4(3):291–299, 1987.
- [27] P Hariharan. *Basics of interferometry*. Elsevier Academic Press, Amsterdam Boston, 2007.
- [28] William Haynes. *CRC handbook of chemistry and physics : a ready-reference book of chemical and physical data*. CRC Press, Boca Raton, Florida, 2013. Online version.
- [29] D. D. Hinshelwood. BERTHA: A versatile transmission line and circuit code. *NASA STI/Recon Technical Report N*, 84:16474, November 1983.
- [30] M. Hohenberger, P.-Y. Chang, G. Fiksel, J. P. Knauer, R. Betti, F. J. Marshall, D. D. Meyerhofer, F. H. Sguin, and R. D. Petrasso. Inertial confinement fusion implosions with imposed magnetic field compression using the omega laser). *Physics of Plasmas (1994-present)*, 19(5):–, 2012.
- [31] J.D Huba. *NRL Plasma Formulary*. Naval Research Laboratory, Washington, DC 20375, 2007.
- [32] K.Y. Kim, V. Kumarappan, and H.M. Milchberg. Measurement of the average size and density of clusters in a gas jet. *Applied Physics Letters*, 83(15):3210–3212, 2003.

- [33] L. D. Landau and L. M. Lifshitz. *Quantum mechanics : non-relativistic theory*, volume 3. Pergamon Press, Oxford New York, third edition, 1977. §77.
- [34] Texas Petawatt Laser. Texas petawatt laser user standard operating procedures (sop). available online: http://texaspetawatt.ph.utexas.edu/doc/TPW_User_-SOP.pdf, July 2011.
- [35] M. A. Lieberman. *Principles of plasma discharges and materials processing*. Wiley-Interscience, Hoboken, N.J, 2005.
- [36] V. Malka, C. Coulaud, J-P Geindre, V. Lopez, Z. Najmudin, D. Neely, and F. Amiranoff. Characterization of neutral density profile in a wide range of pressure of cylindrical pulsed gas jets. *Review of Scientific Instruments*, 71(6):2329–2333, 2000.
- [37] J. C. Martin. Fast pulse vacuum flashover, March 1971. SSWA/JCM/713/157 and AFWL High Voltage Notes, Note 2, 16.
- [38] M. McCormick. PhD thesis, The University of Texas at Austin, 2013.
- [39] K. J. Mendham, N. Hay, M. B. Mason, J. W. G. Tisch, and J. P. Marangos. Cluster-size distribution effects in laser-cluster interaction experiments. *Phys. Rev. A*, 64:055201, Oct 2001.
- [40] C.H. Mielke and B.M. Novac. Experimental and numerical studies of megagauss magnetic-field generation at lanl-nhmfl. *Plasma Science, IEEE Transactions on*, 38(8):1739–1749, 2010.

- [41] I. H. Mitchell, J. M. Bayley, J. P. Chittenden, J. F. Worley, A. E. Dangor, M. G. Haines, and P. Choi. A high impedance mega-ampere generator for fiber z-pinch experiments. *Review of Scientific Instruments*, 67(4), 1996.
- [42] Noboru Miura and Koichi Nakao. Computer analysis of megagauss field generation by condenser bank discharge. *Japanese Journal of Applied Physics*, 29(Part 1, No. 8):1580–1599, 1990.
- [43] N. K. Moncur, R. P. Johnson, R. G. Watt, and R. B. Gibson. Trident: a versatile high-power nd:glass laser facility for inertial confinement fusion experiments. *Appl. Opt.*, 34(21):4274–4283, Jul 1995.
- [44] E I Moses. The National Ignition Facility: Status and Plans for Laser Fusion and High-Energy-Density Experimental Studies. (physics/0111063. UCRL-JC-142223), Nov 2001.
- [45] B. M. Novac. Filamentary modeling of pulsed high-current systems. unpublished report.
- [46] B. M. Novac and I. R. Smith. Advances in the filamentary modelling of electromagnetic flux compression. *Japanese Journal of Applied Physics*, 45(4A):2807–2811, 2006.
- [47] B.M. Novac, I.R. Smith, and M. Hubbard. 2-d modeling of electromagnetic flux-compression in θ -pinch geometry. *Plasma Science, IEEE Transactions on*, 32(5):1896–1901, 2004.

- [48] O Portugall, N Puhlmann, H U Mller, M Barczewski, I Stolpe, and M von Ortenberg. Megagauss magnetic field generation in single-turn coils: new frontiers for scientific experiments. *Journal of Physics D: Applied Physics*, 32(18):2354, 1999.
- [49] Donald Rapp and Paula EnglanderGolden. Total cross sections for ionization and attachment in gases by electron impact. i. positive ionization. *The Journal of Chemical Physics*, 43(5), 1965.
- [50] N. Riley, March 2014. Personal communication.
- [51] J. Singleton, C.H. Mielke, A. Migliori, G.S. Boebinger, and A.H. Lacerda. The national high magnetic field laboratory pulsed-field facility at los alamos national laboratory. *Physica B: Condensed Matter*, 346347(0):614 – 617, 2004. Proceedings of the 7th International Symposium on Research in High Magnetic Fields.
- [52] S. A. Slutz, M. C. Herrmann, R. A. Vesey, A. B. Sefkow, D. B. Sinars, D. C. Rovang, K. J. Peterson, and M. E. Cuneo. Pulsed-power-driven cylindrical liner implosions of laser preheated fuel magnetized with an axial fielda). *Physics of Plasmas (1994-present)*, 17(5):–, 2010.
- [53] Stephen A. Slutz and Roger A. Vesey. High-gain magnetized inertial fusion. *Phys. Rev. Lett.*, 108:025003, Jan 2012.
- [54] R. B. Spielman, F. Long, T.H. Martin, J.W. Poukey, D. B. Seidel, W. Shoup, W.A. Stygar, D. H. McDaniel, M. A. Mostrom, K.W. Struve, P. Corcoran, I. Smith,

and P. Spence. PbfA ii-z: A 20-mA driver for z-pinch experiments. In *Pulsed Power Conference, 1995. Digest of Technical Papers., Tenth IEEE International*, volume 1, pages 396–404 vol.1, July 1995.

- [55] K. Struve. Inductance of a conical transmission line. Personal communication.
- [56] K. Struve, February 2014. Personal communication.
- [57] K. W. Struve, J. L. Porter, and D. C. Rovang. Megagauss field generation for high-energy-density plasma science experiments. Technical report, Sandia National Laboratories.
- [58] K.W. Struve, M.E. Cuneo, J.-P. Davis, S.F. Glover, K.R. LeChien, J.J. Leckbee, M.G. Mazarakis, G.R. McKee, J.L. Porter, M.E. Savage, B.S. Stoltzfus, W.A. Stygar, and J.R. Woodworth. Recent pulsed-power technology advances in the pulsed power sciences center at sandia national laboratories. In *Pulsed Power Conference, 2009 IET European*, pages 1–4, Sept 2009.
- [59] W. A. Stygar, H. C. Ives, T. C. Wagoner, J. A. Lott, V. Anaya, H. C. Harjes, J. P. Corley, R. W. Shoup, D. L. Fehl, G. R. Mowrer, Z. R. Wallace, R. A. Anderson, J. D. Boyes, J. W. Douglas, M. L. Horry, T. F. Jaramillo, D. L. Johnson, F. W. Long, T. H. Martin, D. H. McDaniel, O. Milton, M. A. Mostrom, D. A. Muirhead, T. D. Mulville, J. J. Ramirez, L. E. Ramirez, T. M. Romero, J. F. Seamen, J. W. Smith, C. S. Speas, R. B. Spielman, K. W. Struve, G. E. Vogtlin, D. E. Walsh, E. D. Walsh, M. D. Walsh, and O. Yamamoto. Flashover of a vacuum-insulator interface: A statistical model. *Phys. Rev. ST Accel. Beams*, 7:070401, Jul 2004.

- [60] J. W. G. Tisch, N. Hay, K. J. Mendham, E. Springate, D. R. Symes, A. J. Comley, M. B. Mason, E. T. Gumbrell, T. Ditmire, R. A. Smith, J. P. Marangos, and M. H. R. Hutchinson. Interaction of intense laser pulses with atomic clusters: Measurements of ion emission, simulations and applications. *Nuclear Instruments and Methods in Physics Research B*, 205:310–323, May 2003.
- [61] E. T. Vishniac. The dynamic and gravitational instabilities of spherical shocks. *Astrophysical Journal*, 274:152–167, November 1983.
- [62] E. T. Vishniac. Nonlinear instabilities in shock-bounded slabs. *Astrophysical Journal*, 428:186–208, June 1994.
- [63] L.J. Waxer, T.J. Kessler D.N. Maywar, J.H. Kelly, R.L. McCrory B.E. Kruschwitz, S.J. Loucks, C. Stoeckl D.D. Meyerhofer, S.F.B. Morse, and J.D. Zuegel. High-energy petawatt capability for the omega laser. *Opt. Photon. News*, 16(7):30–36, Jul 2005.
- [64] Y. B. Zeldovich and Y. P. Raizer. *Physics of shock waves and high-temperature hydrodynamic phenomena*. Dover Publications, Mineola, N.Y, 2002.
- [65] J. Zweiback, R. A. Smith, T. E. Cowan, G. Hays, K. B. Wharton, V. P. Yanovsky, and T. Ditmire. Nuclear fusion driven by coulomb explosions of large deuterium clusters. *Phys. Rev. Lett.*, 84:2634–2637, Mar 2000.

Vita

Matthew Wisher graduated from LeTourneau University in Longview, Texas, with the Bachelor of Science degree in Engineering, Electrical Concentration in May 2007. He began graduate studies at The University of Texas at Austin in 2008, where he acquired the Master of Science in Engineering in the summer of 2011.

Permanent address: 13104 Bennington Lane
Austin, Texas 78753

This dissertation was typeset with L^AT_EX[†] by the author.

[†]L^AT_EX is a document preparation system developed by Leslie Lamport as a special version of Donald Knuth's T_EX Program.